LINEAR AND NONLINEAR OPTICAL PROPERTIES OF LOW-DIMENSIONAL STRUCTURES ON VICINAL SILICON (111) SURFACES

A thesis submitted to
THE UNIVERSITY OF DUBLIN
for the degree of
Doctor in Philosophy

JULIE JACOB

School of Physics
University of Dublin
Trinity College
Dublin 2
Ireland

October 2007

DECLARATION

This thesis has been submitted to the University of Dublin for examination for the degree of Doctor in Philosophy by the undersigned.

This thesis has not been submitted as an exercise for a degree to any other university.

With the exception of the assistance noted in the acknowledgements, this thesis is entirely my own work.

I agree that the Library of the University of Dublin may lend or copy this thesis upon request.

Julie Jacob October 2007

School of Physics,
University of Dublin,
Trinity College,
Dublin

Abstract

Reflectance anisotropy spectroscopy (RAS) and second harmonic generation (SHG) have been used to probe various low-dimensional (LD) structures grown on vicinal Si(111) surfaces under ultra-high vacuum (UHV) conditions. Reflectance anisotropy spectroscopy (RAS) spectra of single domain Si(111)-5×2-Au, Si(557)-5×1-Au, Si(111)-4×1-In and Si(111)-3×1-Ag structures showed a large minima in the region below 3 eV, which show a systematically higher polarizability perpendicular to the adsorbate chains, for all the structures. The detail, however, varies with the adsorbate, the reconstruction and the offcut. The RAS spectra of Si(111)-5×2-Au showed changes with offcut angle in the 1 to 3 eV region, where Au-induced structures appear. The variation was found consistent with different populations of single- and double-chain gold structures formed in the region of the steps.

One-dimensional (1D) arrays of nanodots were grown on a single domain (3×1)-Ag surface by depositing 0.5 monolayer (ML) of Ag on the Si(111)-3×1-Ag surface. Reflectance anisotropy spectroscopy (RAS) was used, together with scanning tunneling spectroscopy (STS), to investigate the optical and electronic properties of the nanodots. Scanning tunneling spectroscopy (STS) of the Ag nanodots revealed a bandgap of ~0.6 eV, which is attributed to the opening of a Kubo gap due to confinement of the electron wavefunction. The nanodots showed a very small optical response in the infrared (IR) region which is consistent with their non-metallic character. Larger, anisotropic 3D Ag islands were formed by further deposition of Ag. Scanning tunneling spectroscopy (STS) showed a well-developed metallic character, in agreement with their larger size. Reflectance anisotropy spectroscopy (RAS) measurements extended into the IR region, showed a large positive anisotropy consistent with the electronic properties of the nanostructures measured by STS. The large positive IR anisotropy for the 3D Ag islands is in the region where anisotropic Drude-like intraband transitions begin to become significant, the larger polarizability being aligned along the length of the islands, where the inelastic scattering electron mean free path is expected to be longer. The anisotropy was also found to be influenced by the offcut angle of the substrate, and hence the terrace width. The agreement between the electronic properties, as measured by STS and the IR measurements indicates that infrared RAS should be a useful technique for the non-contact probing of the metallicity of aligned anisotropic nanostructures.

The Ag nanostructures were then capped with amorphous Si to form a near-IR transparent protecting layer. The samples were stable to exposure to ambient conditions for significant periods. The RAS spectra were compared to model calculations, which support the conclusion that the metallic nanostructures survived the capping, while the (3×1)-Ag areas not covered by the nanostructures are modified by the deposition of Si. In contrast, the quasi-1D structure of Si(111)-4×1-In did not survive the capping by amorphous Si as the optical signature of the (4×1)-In structure was quenched on capping.

Optical second harmonic generation (SHG) was used to study the structural symmetry of 3×1-Ag, $\sqrt{3}\times\sqrt{3}$-Ag, Ag nanodots and Ag islands grown on vicinal Si(111). For the Si(111)-3×1-Ag structure, using *s*-output measurements, it was found that there are tensor components making significant contributions to the SH intensity that are identically zero in the presence of a mirror plane. This is a conclusive proof that the (3×1)-Ag structure does not possess a mirror plane in the $[\bar{1}\bar{1}2]$ direction, in agreement with a previous SHG study of this structure grown on a singular surface. These results were contrasted with those from Si(111)-$\sqrt{3}\times\sqrt{3}$-Ag, where the response is consistent with the presence of a mirror plane. Analysis of SHG studies of Ag nanodots and Ag islands revealed deviation from 3m symmetry, implying interaction of the Ag nanostructures with the underlying (3×1)-Ag chain.

Acknowledgements

I would like to express my sincere gratitude to my supervisor, Prof. John McGilp, for providing me with an opportunity to work in the Surface and Interface Physics Lab. He followed my entire thesis work very closely and always provided solutions to many difficult problems. This work would not have been possible without his guidance and encouragement.

My sincere thanks to Prof.(Mrs.) R.C Aiyer for her guidance and encouragement she rendered during my research career as an M.Phil. student.

Many thanks to Dr. Lee Carroll for introducing me to everything about UHV and other experimental equipments required for this thesis work. I am grateful to Dr. Sandhya Chandola for her suggestions with the sample preparation and for the STM work. Many thanks to Dr. Karsten Fleischer for the experimental help and suggestions during critical situations.

Many thanks to Chris Smith for the ellipsometry measurements and for lending me a computer for my thesis write up. I wish to thank Nial McAlinden for the RAS work on Si(557)-Au. Thanks to John Cunniffe for his help while assembling the UHV components.

Many thanks to Nikos, who was always willing to lend a hand during difficult experimental times in the lab.

I wish to thank John Kelly for allowing me to sit in the post-doc office during my write up and for all the administrative help. Many thanks Joe, Mick, Dave, Patrick, Nigel and Ken for their technical help.

Many thanks to those who happened to be my way, for their help in removing/assembling the bake out panel or the sample manipulator!

My thanks to Chris, Lee, Karsten, Nikos, Sandhya, John, Nial and Leena for taking me to lunch and the nice evening times at O’Neill’s and café en Seine.

My sincere thanks to Sumesh all his help, support, suggestions and encouragement during the difficult times. I wish to thank all my friends Sumesh & Parvathy, Sibu & Reena, Vamsi & Swarna, Venky & Lakshmi, Satheesh & Bhavna, Uttam & Mahua, Manjula, Rajat, Pratheep, Vinod for the nice party time in Dublin.

Many thanks to Georgeachen, Cicychechi and Appu for inviting me to their house and for the nice food I had during my stay in Dublin. I wish to thank my parents, my sisters and brothers-in-law for all their support and encouragement.

Publications

Optical response of Ag-induced reconstructions on vicinal Si(111)
S. Chandola, **J. Jacob**, K. Fleischer, P. Vogt, W. Richter, J. F. McGilp
Physica Status Solidi B 2005, 242:3017-3021

Optical and electronic properties of Ag nanodots on Si(111)
S. Chandola, **J. Jacob**, K. Fleischer, P. Vogt, W. Richter, J. F. McGilp
Journal of Physics: Condensed Matter 2006, 18:6979-6986

Reflectance anisotropy studies of the formation of 5×2-Au structures on Si(111) surfaces with different step formations
J. Jacob, N. McAlinden, K. Fleischer, J. F. McGilp
Physica Status Solidi B 2007 (Communicated)

Optical second-harmonic generation studies of Si(111)-$\sqrt{3}\times\sqrt{3}$-Ag and Si(111)-3×1-Ag grown on vicinal Si(111)
J. Jacob, A. Gomes Silva, K. Fleischer, J. F. McGilp
Physica Status Solidi B 2007 (Communicated)

Using reflectance anisotropy spectroscopy to characterize capped metal nanostructures on silicon,
K. Fleischer, **J. Jacob**, S. Chandola, N. Esser, J. F. McGilp
Physica Status Solidi B 2007 (Communicated)

Table of Acronyms

1D	One-dimensional
UHV	Ultra-high vacuum
LD	Low-dimensional
RAS	Reflectance anisotropy spectroscopy
SHG	Second-harmonic generation
RA	Reflectance anisotropy
IR	Infra-red
SH	Second-harmonic
EM	Electromagnetic
ML	Monolayer
EUV	Extreme ultra violet
SK	Stranski-Krastanov
VW	Volmer-Weber
CDW	Charge density wave
SDW	Spin density wave
DAS	Dimer-adatom-stacking fault
THEED	Transmission high energy electron diffraction
STM	Scanning tunneling microscopy
STS	Scanning tunneling spectroscopy
JDOS	Joint density of states
SDA	Surface dielectric anisotropy
LEED	Low energy electron diffraction
RHEED	Reflection high energy electron diffraction
AES	Auger electron spectroscopy
HTEZ	High temperature effusion cell
SUSI	Silicon sublimation source
FSW	Fused silica window
PMT	Photomultiplier tube
ARUPS	Angle resolved ultra-violet photoelectron spectroscopy
EELS	Electron energy loss spectroscopy
ARPES	Angle resolved photoemission spectroscopy
QCO	Quartz crystal oscillator
HCC	Honeycomb chain-channel

DB	Dangling bond
LEEM	Low energy electron microscopy
PEEM	Photoemission electron microscopy
IPES	Inverse photoemission spectroscopy
QSE	Quantum size effects
HCT	Honeycomb-chained triangle
IET	Inequivalent triangle

Table of contents

1. Introduction

2. Low-dimensional structures and their optical response

3. Phenomenology of RAS and SHG

4. Experimental details

5. RAS of anisotropic structures grown on vicinal Si(111)

6. RAS of uncapped and capped metal structures

7. SHG of Ag induced reconstructions and nanostructures

8. Conclusions and outlook

Appendix

1

Introduction

1.1 Overview

One-dimensional (1D) electron systems are revealing new and interesting phenomena, such as spin-charge separation in a Lutttinger liquid, charge density waves, the Peierls gap, mixed dimensionality and 1D quantum well states, but much of the physics of these systems remains to be explored and understood [1]. The development of this field has been limited, until recently, by the bulk sample preparation techniques used, which involved the growth of three-dimensional crystals consisting of weakly coupled linear chains, e.g. rows of transition metal ions kept apart by a rigid lattice of counterions. This approach produced a large measurement volume for bulk sensitive experiments, such as neutron scattering, but the residual coupling between the chains depended on the crystalline structures formed. Polymers, however, are more flexible with respect to tailoring the chain spacing by the addition of branches, but they do not order very well. More recently, the synthesis of highly perfect nanowires, such as carbon nanotubes, has stimulated the investigation of individual objects with 1D character. Probing the electronic structure of an individual nanowire is still at a rudimentary stage, however. It is very difficult to attach leads to a single nanowire that connect it to the macroscopic world. Fabricating contacts by conventional lithography introduces surface contamination that influences the electronic structure of the nanowire.

1D electron systems can be synthesized at stepped surfaces by self-assembly of atomic and molecular chains. Surface science techniques have been used recently to produce clean and well-ordered arrays of chains at planar surfaces [1-3]. Locking the chains to a crystalline substrate as a superlattice makes it possible to control their spacing with atomic precision. A wide variety of adsorbate and substrate combinations provides opportunities for systematically tailoring electronic properties, such as the intra-chain and inter-chain coupling, the electron count and the Coulomb interaction.

Regular arrays of monatomic steps can be produced on planar Si(111) single crystal surfaces, with periodicities ranging from 2 to 80 nm, and with very low kink densities, due to the highly directional nature of the Si bonding [1]. Tailored arrays of chains can be produced by self-assembly at such surfaces, where nucleation and growth typically initiates at the step edges. Conventional surface science techniques have been used to show that structures such as Si(111)-5×2-Au, Si(111)-3×1-Ag and Si(111)-4×1-In have 1D chain structures of typical width ~1 nm for the individual chains, where the formation of 1D electronic states are expected [1]. These nanostructures are grown by self-assembly and also characterized under ultra-high vacuum (UHV) conditions. The potential of this approach to growing 1D systems is exemplified by the Si(111)-4×1-In system, where recent high brightness synchrotron angle-resolved photoemission studies, in the region 0 to 5 eV below the Fermi level, have provided the first fascinating evidence that the In chains are 1D conducting wires, with a Peierls gap opening at low temperature on formation of a charge density wave, although the latter point remains controversial [4-9]. Further, these surfaces can be used as a template to obtain arrays of quantum dots or anisotropic metal islands [10-13]. The nanodots arrange regularly in a self assembling manner and hence its size and position are highly controllable.

These model systems have excellent potential for exploring low-dimensional (LD) phenomena and, being based on planar Si substrates with growth techniques compatible with current semiconductor processing technology, the systems are also very promising, in the longer term, for nanoscale device fabrication. The main goal of this work is to explore the characteristics of such nanostructures, *in situ* and non-destructively by linear and nonlinear optical techniques. Secondly, capping layers are needed on LD structures to protect them from ambient conditions during study or use outside the growth chamber. The presence of a capping layer poses significant problems for surface scientists who wish to examine these interfaces directly at an atomic level. Electron-based techniques, including scanning probe techniques do not penetrate the capping layers. Photon-based techniques are often still applicable, because capping layers at typically ~1 nm -10 nm thick, is less than the absorption depth for optical radiation. A problem to be overcome is that the interfacial spectroscopic signal is often mixed in with very similar bulk-phase signals that can be several orders of magnitude larger. This may make it impossible to extract the desired interfacial spectroscopic information. The key attribute of linear and nonlinear optical techniques used here is the ability to probe both electronic and crystallographic structure at interfaces, while avoiding interference from bulk phases.

1.2 Optical characterisation techniques and previous work

The optical characterisation techniques used in this work are reflectance anisotropy spectroscopy (RAS) and second harmonic generation (SHG). These state-of-the art epioptic [14] techniques exploit the difference in symmetry between the surface or interface and the centrosymmetric structure of substrates such as silicon (and also capping layers) in order to eliminate the normally dominant bulk response [15]. Optical techniques are particularly sensitive to stepped surfaces and interfaces because the symmetry is further reduced [16]. However, anisotropic reconstructions of isotropic bulk exposed planes complicate symmetry considerations. Under these circumstances, the symmetry of the substrate often dictates that a number of symmetry-related domains are formed. For example, singular Si(111) substrates allow three equivalent one-dimensional structures (chain direction $[1\bar{1}0]$, $[01\bar{1}]$ and $[\bar{1}01]$). Stepped silicon surfaces break the three fold symmetry of the substrate and lead to a single domain if the step edge runs along one of the three equivalent chain directions. Hence, the use of stepped surfaces promotes a dominant domain on the surface that will give rise to a RAS signal, whereas equal domain populations ensure the absence of optical anisotropy, even though each domain is itself anisotropic.

The potential for monitoring “self-assembly” of adsorbates on vicinal surfaces in real time is an important attribute of RAS. For example, the development of Si(111)-5×2-Au has been studied by RAS [17]. Initially the vicinal Si(111)-7×7 shows no significant macroscopic anisotropy. As Au is deposited, the single domain (5×2) structure grows, creating a macroscopically anisotropic surface which can be monitored by RAS and which grows in intensity while preserving its spectral shape until the restructuring of the surface is complete. Once the maximum RA signal has been observed and the restructuring of the surface is complete, further deposition of Au gives rise to the growth of the ($\sqrt{3}\times\sqrt{3}$) structure, which is optically isotropic. The RA spectrum decays steadily and eventually reduces to zero when the ($\sqrt{3}\times\sqrt{3}$) structure is complete. RAS studies of both Si(111)-5×2-Au and Si(111)-4×1-In show a dominant linear polarizability perpendicular to the chain and step edges, between 1.5 and 3 eV [18-21]. This is interpreted in terms of electron confinement perpendicular to step edges. These RAS studies did not provide any evidence of quasi-1D metallicity along the chains, as any optical response associated with metallicity was assumed to be in the lower energy. RAS studies of Si(111)-4×1-In extended to lower energy provided evidence for this [19]. RAS shows an emergence of a positive structure below ~1.4 eV consistent with a dominant in-plane linear polarizability along the chains. By extending the spectral range into the infrared (IR), RAS has been utilised successfully to study anisotropic metal islands and isolated wires with direct observation of conductance anisotropy [22-24]. The observed large optical anisotropy directly reflects the morphological anisotropy, which arises from the presence of perfectly aligned self-assembled nanowires. Metallic conductors have Drude-like intraband contribution to the IR spectral region [25]. The observed large positive IR response with dominant polarizability along the long axes of the islands is in the spectral region where anisotropic Drude-like intraband transitions are expected to make significant contribution to the optical spectrum. The response can be modelled by an anisotropic Drude-type dielectric function with two independent tensor components, ε_x and ε_y, contributing to the RAS signal. This simple model appears promising in relating the measured spectra of metallic nanowires and islands to the conductance anisotropy, thus facilitating contactless measurement of this quantity.

The second optical technique used is SHG. Silicon is a material with bulk inversion symmetry and, within the dipole approximation, SHG from the bulk is parity forbidden. At the surface the inversion symmetry is broken and surface dipole exists, allowing the production of a dipolar SHG signal. Care is required however, as higher order bulk quadrupolar and magnetic dipolar contributions are allowed, and these may be comparable in size to the dipolar surface and interface signal. As the fundamental energy is scanned, resonances appear at direct optical transitions involving electronic states of specific symmetries, at either the fundamental or the SH energy. SHG has provided important information on the electronic structure at surface steps [26]. These electronic states have the reduced symmetry of the surface or interface and, in addition, selection of the fundamental and SH electromagnetic field vectors (polarisation vectors) allows different electronic resonances to be accessed, this additional information coming from exciting the various independent nonlinear susceptibility tensor components [27].

SHG studies of Si(111)-4×1-In show that the SH intensity is a factor of six greater when the electric field vectors are aligned along the In chains, compared with alignment orthogonal to the chains [28].This appears to be the 1D equivalent of the general observation that the nonlinear susceptibility of metals is larger than that of semiconductors or insulators, due to the increased polarizability, in the optical region of the spectrum, of electrons in metallic systems. There have been a number of SHG studies of Ag structures on Si(111), mostly concerned with investigating the origin of oscillations of the SH intensity with film thickness above 1 ML coverage [29-34]. In addition, the sensitivity of SHG to surface symmetry has been used to probe the symmetry of the 3×1 and $\sqrt{3} \times \sqrt{3}$ reconstructions on singular Si(111) [35-37].

Self-organised nanostructure arrays are also ideal test structures to investigate changes in metallic properties upon capping. Optical techniques like RAS and SHG are very well suited to probe the properties of buried nanostructures, as their penetration depth is much larger than that of conventional surface probes, and the lower symmetry of aligned nanostructures helps to discriminate the nanostructure response from the residual interface, bulk and capping layer response [16].

1.3 Thesis outline

The main aim of this work is to use the epioptic [14] techniques like RAS and SHG to identify the optical signatures associated with the various low dimensional structures.
The outline of thesis chapters is as follows:

Chapter 2 gives a brief review on the properties of low-dimensional structures and their optical response. Chapter 3 describes the phenomenological theory behind RAS and SHG. Chapter 4 describes the experimental set-up used for RAS and SHG and also sample cleaning procedures. Chapter 5 focuses on the preparation of Si(111)-4×1-In, Si(111)-5×2-Au and Si(111)-3×1-Ag surfaces. Characterization of these surfaces by RAS is then discussed. Chapter 6 presents and discusses the RAS of island structures formed on anisotropic surface reconstructions on offcut Si(111) surfaces and the RAS of In and Ag nanostructures capped using silicon. Chapter 7 presents SHG measurements of Si(111)-$\sqrt{3}\times\sqrt{3}$-Ag, Si(111)-3×1-Ag, silver nanodots and silver islands. Chapter 8 gives the summary and outlook for future work.

References

1. Himpsel FJ, Altmann KN, Bennewitz R, Crain JN, Kirakosian A, Lin JL, McChesney JL: **One-dimensional electronic states at surfaces.** *Journal of Physics-Condensed Matter* 2001, **13:**11097-11113.
2. Himpsel FJ, Jung T, Kirakosian A, Lin JL, Petrovykh DY, Rauscher H, Viernow J: **Nanowires by step decoration.** *MRS Bulletin* 1999, **24:**20-24.
3. Himpsel FJ, Jung T, Ortega JE: **Nanowires on stepped metal surfaces.** *Surface Review & Letters* 1997, **4:**371-380.
4. Kumpf C, Bunk O, Zeysing JH, Su Y, Nielsen M, Johnson RL, Feidenhans'l R, Bechgaard K: **Low-temperature structure of indium quantum chains on silicon.** *Physical Review Letters* 2000, **85:**4916-4919.
5. Yeom HW, Takeda S, Rotenberg E, Matsuda I, Horikoshi K, Schaefer J, Lee CM, Kevan SD, Ohta T, Nagao T, Hasegawa S: **Instability and charge density wave of metallic quantum chains on a silicon surface.** *Physical Review Letters* 1999, **82:**4898-4901.
6. Sakamoto K, Ashima H, Han Woong Y, Uchida W: **Angle-resolved high-resolution electron-energy-loss study of In-adsorbed Si(111)-(4*1) and -(8*2) surfaces.** *Physical Review B-Condensed Matter* 2000, **62:**9923-9926.
7. Yeom HW, Horikoshi K, Zhang HM, Ono K, Uhrberg RIG: **Nature of the broken-symmetry phase of the one-dimensional metallic In/Si(111) surface.** *Physical Review B (Condensed Matter and Materials Physics)* 2002, **65:**241307-241301.
8. Tsay SF: **Atomic and electronic structure of the (4*1) and (8*2) In/Si(111) surfaces.** *Physical Review B (Condensed Matter and Materials Physics)* 2005, **71:**35207-35201.
9. Gonzalez C, Ortega J, Flores F: **Metal-insulator transition in one-dimensional in-chains on Si(111): combination of a soft shear distortion and a double-band Peierls instability.** *New Journal of Physics* 2005, **7**.
10. Kuntze J, Mugarza A, Ortega JE: **Ag-induced zero- and one-dimensional nanostructures on vicinal Si(111).** *Applied Physics Letters* 2002, **81:**2463-2465.
11. Owen JHG, Miki K: **Growth of Ag nanoclusters on a 1D template.** *Surface Science* 2006, **600:**2943-2953.
12. Zhachuk RA, Teys SA, Dolbak AE, Olshanetsky BZ: **Formation of ordered arrays of Ag nanowires and nanodots on Si(557) surface.** *Surface Science* 2004, **565:**37-44.
13. Hirayama H, Horie R, Takayanagi K: **Nucleation of Ag nanodots at the Si(111)3*1-Ag surfaces.** *Surface Science* 2001, **482-485:**1277-1282.
14. McGilp JF: **Optical second-harmonic generation for studying surfaces and interfaces.** *Journal of Physics Condensed Matter* 1989, **1:**85-92.
15. McGilp JF: **Optical Characterization of Semiconductor Surfaces and Interfaces.** *Progress in Surface Science* 1995, **49:**1-106.
16. McGilp JF: **Optical response of low-dimensional In nanostructures grown by self-assembly on Si surfaces.** *Physica Status Solidi a-Applied Research* 2001, **188:**1361-1369.

17. Power JR, Weightman P, O'Mahony JD: **Strong optical anisotropy of the single-domain 5*2-Au reconstruction on vicinal Si(111).** *Physical Review B-Condensed Matter* 1997, **56:**3587-3590.
18. Pedreschi F, Omahony JD, Weightman P, Power JR: **Evidence of electron confinement in the single-domain (4*1)-In superstructure on vicinal Si(111).** *Applied Physics Letters* 1998, **73:**2152-2154.
19. Fleischer K, Chandola S, Esser N, Richter W, McGilp JF: **Reflectance anisotropy spectroscopy of Si(111)-(4*1)-In.** *physica status solidi (a)* 2001, **188:**1411-1416.
20. Fleischer K, Chandola S, Esser N, Richter W, McGilp JF: **Phonon and polarized reflectance spectra from Si(111)-(4*1)In: evidence for a charge-density-wave driven phase transition.** *Physical Review B (Condensed Matter and Materials Physics)* 2003, **67:**235318-235311.
21. Fleischer K, Chandola S, Esser N, Richter W, McGilp JF, Schmidt WG, Wang S, Lu W, Bernholc J: **Atomic indium nanowires on Si(111): the (4*1)-(8*2) phase transition studied with reflectance anisotropy spectroscopy.** *Applied Surface Science* 2004, **234:**302-306.
22. Jalochowski M, Strozak M, Zdyb R: **Reflectance anisotropy during growth of Pb nanowires on well ordered Si(3 3 5) surface.** *Applied Surface Science* 2003, **211:**209-215.
23. Strozak M, Hnatyuk V, Jalochowski M: **Optical properties of Pb nanowires on Si(3 3 5).** *Vacuum* 2004, **74:**241-245.
24. Fleischer K, Chandola S, Herrmann T, Esser N, Richter W, McGilp JF: **Free-electron response in reflectance anisotropy spectra.** *Physical Review B (Condensed Matter and Materials Physics)* 2006, **74:**195432-195410.
25. Johnson PB, Christy RW: **Optical constants of the noble metals.** *Physical Review B (Solid State)* 1972, **6:**4370-4379.
26. Power JR, O'Mahony JD, Chandola S, McGilp JF: **Resonant Optical 2nd-Harmonic Generation at the Steps of Vicinal Si(001).** *Physical Review Letters* 1995, **75:**1138-1141.
27. McGilp JF: **Second-harmonic generation at semiconductor and metal surfaces.** *Surface Review and Letters* 1999, **6:**529-558.
28. Chandola S, McGilp JF: **Optical second harmonic generation at Si(111)-In interfaces: Evidence of quasi-one-dimensional metallicity.** *physica status solidi (a)* 2001, **184:**111-116.
29. Pedersen TG, Pedersen K, Kristensen TB: **Optical second-harmonic generation from Ag quantum wells on Si(111)7*7: Experiment and theory.** *Physical Review B-Condensed Matter* 1999, **60:**R13997-14000.
30. Pedersen K, Kristensen TB, Pedersen TG, Morgen P, Li Z, Hoffmann SV: **Optical second-harmonic generation and photoemission from quantum well states in thin Ag films on Si(1 1 1).** *Surface Science* 2001, **482-485:**735-739.
31. Hirayama H, Kawata T, Takayanagi K: **Oscillation of the optical second-harmonic generation intensity during Ag thin film growth on a Si(111)7*7 surface.** *Physical Review B-Condensed Matter* 2001, **64:**195411-195415.
32. Hirayama H, Komizo T, Kawata T, Takayanagi K: **Changes of phase and intensity of optical SHG with Ag deposition on Si(111)-7*7 surfaces.** *Applied Surface Science* 2002, **190:**108-112.
33. Hirayama H, Yamasaki A, Kawata T: **Change of optical second harmonic generation intensity during Ag deposition on Si(111)7*7 and Si(111)sqrt[3]*sqrt[3]-Ag surfaces.** *Surface Science* 2003, **532-535:**922-927.
34. Hirayama H, Watai M: **Two-photon resonance in optical second harmonic generation from quantum well states in ultra-thin Ag films grown on Si(1 1 1) surfaces.** *Surface Science* 2006, **600:**3825-3829.

35. Dongmei D, Suzuki T: **Nucleation and growth of Si(111)-sqrt[3]*sqrt[3]-Ag investigated in situ using second-harmonic generation.** *Physical Review B (Condensed Matter and Materials Physics)* 2005, **72:**85308-85301.
36. Deng D, Suzuki T: **Si(111)-3*1-Ag reconstruction studied in situ at elevated temperatures by second-harmonic generation.** *Japanese Journal of Applied Physics, Part 2 (Letters)* 2004, **43:**510-512.
37. Venkataraghavan R, Aono M, Suzuki T: **Studies on the nucleation, dynamics and structure of the Si(111)-sqrt[3]*sqrt[3]-Ag surface using surface second-harmonic generation.** *Surface Science* 2002, **517:**65-74.

2

Low-dimensional structures and their optical response

2.1 Overview

The first section of this chapter introduces the singular Si(111) surface, and the dimer adatom stacking-fault model for its 7×7 reconstruction. A brief outline of vicinal Si(111) surfaces is also given. Low-dimensional nanostructures grown by self-assembly and their electronic and optical properties are reviewed in the following sections.

2.2 The Si(111) substrate

2.2.1 The Si(111)-7×7-surface

A silicon crystal has a diamond lattice, in which each Si atom has four electrons with which to make covalent bonds with four neighbours in a tetrahedral arrangement [1]. When the valence electrons $(3s)^2(3p)^2$ of a Si atom form hybrid orbitals sp^3 to make bonds with neighbouring atoms, their energy levels split into bonding and anti-bonding states. The valence electrons are accommodated in the bonding state, so the anti-bonding state is empty. Since in a crystal many atoms make bonds with each other to arrange themselves periodically, these energy levels are broadened to make bands: the valence band and the conduction band, respectively. But on the ideal bulk terminated surface there exist dangling bonds (unpaired hybrid orbitals) which are similar to the hybrid orbitals of isolated atoms, whose energy levels will be located between the bonding and anti-bonding states, or within an energy gap. In fact, the dangling-bond state on a clean Si(111) surface is known to lie around the middle of the band gap . But when foreign atoms come to make bonds with the topmost Si atoms, the dangling-bond state will again split into bonding and anti-bonding states. When, furthermore, the adsorbates induce a surface superstructure to form some orbital overlap between neighbouring sites, the bonding and anti-bonding states will again be broadened and become bands. These are surface-state bands, inherent in the surface superstructure. The bands have their own characters, distinct of the bulk electronic states. Figure 2.1 sets out schematically, the formation of surface state bands [1].

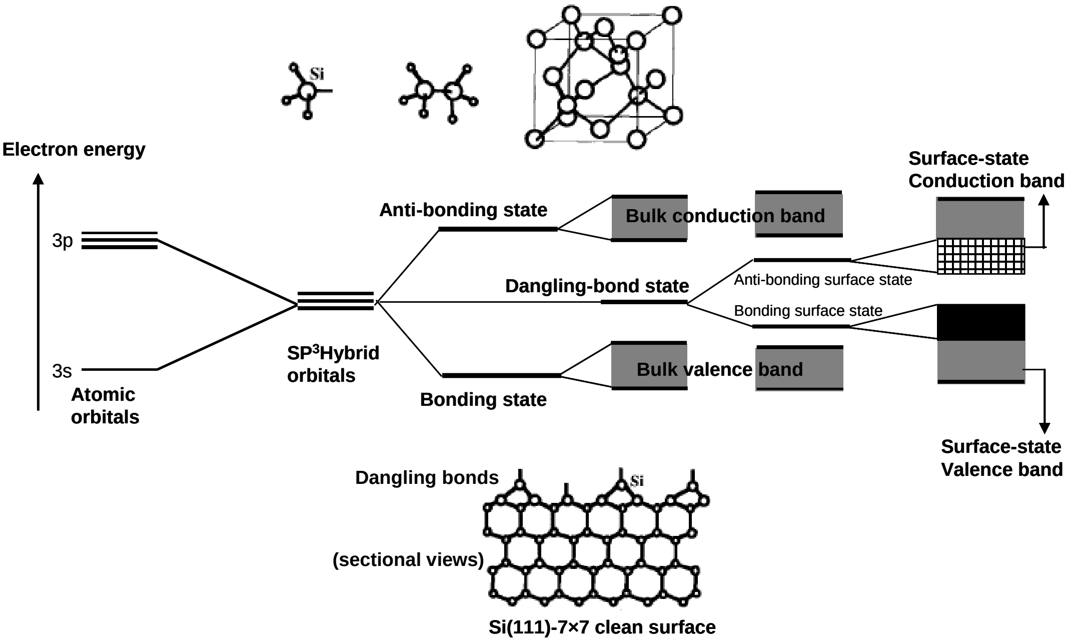

Figure 2.1 A schematic diagram for atoms and molecules, and also the bulk and the surface of a silicon crystal

The generally accepted structure for the Si(111)-7×7 reconstructed surface is the dimer-adatom-stacking-fault (DAS) model proposed by Takayanagi [2] after scanning tunnelling microscopy (STM) and transmission high-energy-electron diffraction (THEED) studies of the surface. This structure is shown in figure 2.2 [3]. The lozenge of the 7×7-unit cell has corner holes, which are connected to each other by chains of *dimers*. This unit cell is regarded as containing two triangles separated by the dimer chains. Each triangle has six *adatoms* (large pink balls) and three rest atoms, arranged locally in a 2×2 periodicity. The

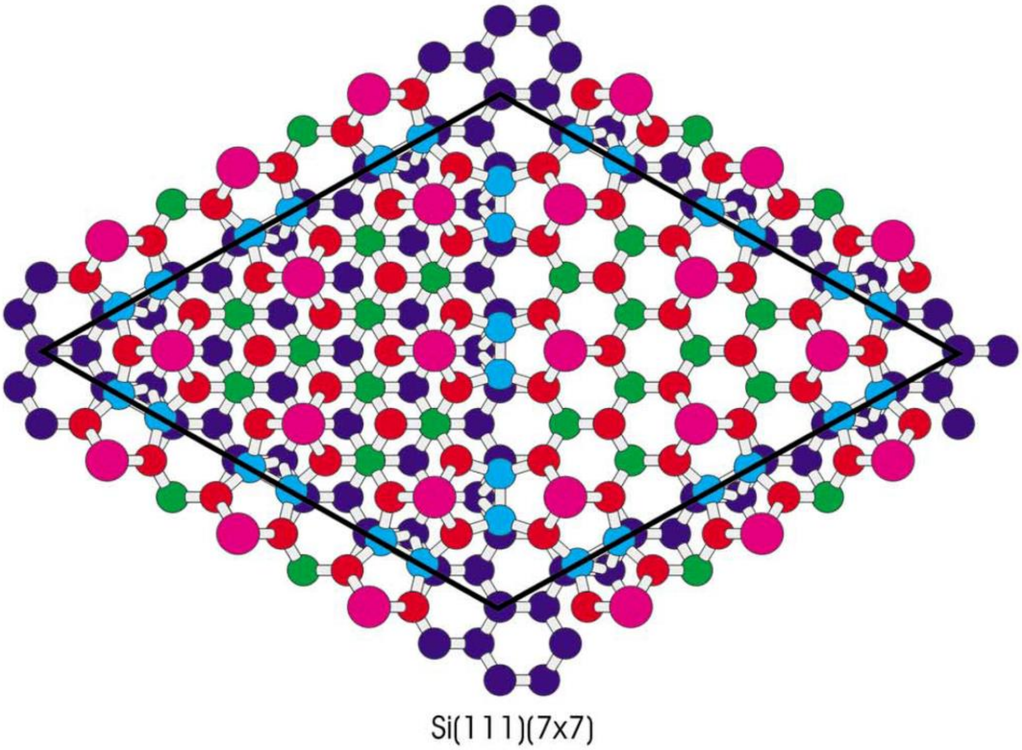

Figure 2.2 Schematic diagram, in plan view, of the DAS model of of Si(111)-7×7 surface; the bold lines again show the surface unit mesh. In this diagram the adatoms are shown as large pink spheres, while the dimerised Si atoms are shown as pale blue. The red spheres show un-dimerised Si atoms in this same layer. The Si atoms in the layer below are shown green, while those in deeper layers are dark blue [3].

left and right triangles have opposite stacking sequences; the left hand side has a stacking fault (*faulted half*), while the right does not (*unfaulted half*). The structure has 19 dangling bonds per 7×7 unit cell, which is a significant reduction in the number of unpaired electrons from 49 at an ideal unreconstructed (111) surface. This leads to a decrease of the total energy, which is, however balanced against an energy increase caused by large angular strains of unusual bondings, such as dimers and adatoms. A review of the models proposed previous to the DAS reconstruction, together with the DAS structure is given by Haneman [4]. Prior to the advent of STM, the 7×7 reconstruction, indicated by electron diffraction techniques, could not be observed on the atomic scale. The first STM topographs obtained by Binning *et al.* [5] imaged spots within the 7×7 unit cell, at both positive and negative biases, which were thought to be adatoms on an otherwise bulk-terminated substrate. Such a model was shown to lead to high strain, and in any case there was no guarantee that these STM peaks were in fact localized on single atoms. Ion scattering measurements [6-8] could not be explained without the incorporation of a stacking fault into a model for the surface. The lateral sensitivity of THEED work by Takayanagi *et al.* [2], with calculations of projected atom positions, led to the final structure shown in the figure [3]. This has become the widely accepted model of the Si(111)-7×7 surface.

Data analysis confirmed that the images seen by STM were indeed adatoms and that a fifth layer stacking fault existed in one half of the 7×7 unit cell. STM topographs at different sample biases were made by Tromp *et al.* [9] and showed a clear asymmetry between opposite halves of the 7×7 unit cell, resulting from the small difference in energy of the dangling bond surface states in the different halves. It has been found by Chou *et al.* [10] that the stacking fault introduces a surface sate at 0.1 eV above the valence band, dispersing into the valence band. Evidence for the stacking fault and adatoms has also been found in XRD measurements by Robinson *et al*. [11]. The other major feature of the model is the existence of dimers which delineate the sides of each half of the unit cell.

The effect of the DAS 7×7 reconstruction is to reduce the number of dangling bonds per unit cell. However, the surface is still reactive and possible adsorption sites include direct adsorption onto the dangling bonds, substitution for the adatoms, and adsorption in the corner hole, or breaking of the dimer bonds. All these adsorption sites affect the dangling bonds and any surface states associated with them.

2.2.2 Vicinal Si(111) surfaces

A vicinal surface of a single-crystal is a free surface whose orientation is close to that of a low Miller index surface. Vicinal surfaces are typically obtained by cutting a single crystal slightly off a low-Miller index direction, by an angle called the miscut angle. When suitably prepared, at the atomic scale a vicinal surface consists either of a regular array of parallel atomic steps separating atomically flat atomic terraces, or an array of an accumulations of atomic steps separated by flat terraces, a phenomenon called step bunching [12, 13]. Step bunching can be viewed as a periodic micro-faceting of a surface. Preparation usually consists of a series of cleaning/annealing cycles or homoepitaxial overgrowth, or a combination of several such procedures. Vicinal surfaces can act as templates for further deposition, where growth occurs preferentially at the steps (step decoration). For vicinal surfaces this has been demonstrated on variety of adsorbate/substrate combinations such as Ag/Pt(997) [14], Co/Pt(997) [15] , Ga/Si(112)

[16], Gd/Si(111) [17] , Au on Si(337), Si(557), Si(5 5 12) [18, 19] or Ag/Si(5 5 12) surfaces.

The Si(111)-7×7 surface has a particularly stable step geometry. The top edge of an equilibrated step consists of a string of corner holes of the 7×7 unit cell, running along the $[\bar{1}10]$ direction [20-22]. Thereby, the 7×7 reconstruction helps ordering the step arrays by quantizing the terrace width in units of half the 7×7 unit cell [23]. This still leaves two possible orientations of the step edge, where the surface normal is tilted from (111) towards opposite directions, i.e., $[11\bar{2}]$ and $[\bar{1}\bar{1}2]$. Due to the symmetry of bulk Si crystal structure, the surfaces misoriented towards these directions have inherently different structures from each other. Figure 2.3 shows the ideally truncated surfaces of misoriented Si(111) crystal toward $[11\bar{2}]$ (left) and $[\bar{1}\bar{1}2]$ (right) directions, respectively. These two surfaces have different chemical bond configurations at step edges; only one dangling bond (DB) at a step-edge Si atom for the $[11\bar{2}]$-directed miscut, while two DBs for the $[\bar{1}\bar{1}2]$ case [24]. The steps with the $[\bar{1}\bar{1}2]$ tilt are taken as the most stable configuration since they are found to occur during Si-on-Si(111) epitaxy [25]. Arrays of single steps can be obtained from samples cut 1.1° towards $[\bar{1}\bar{1}2]$ using a multi-stage annealing sequence [26]. The most critical part is a quench to 850°C within 3 s for avoiding step tripling. Rapid quenching through step bunching regions allows preserving the single-height steps that are stable at high temperature. Thermal disorder from the quench can be removed in a post anneal at lower temperatures, where the mobility is too low for step bunching. However, if

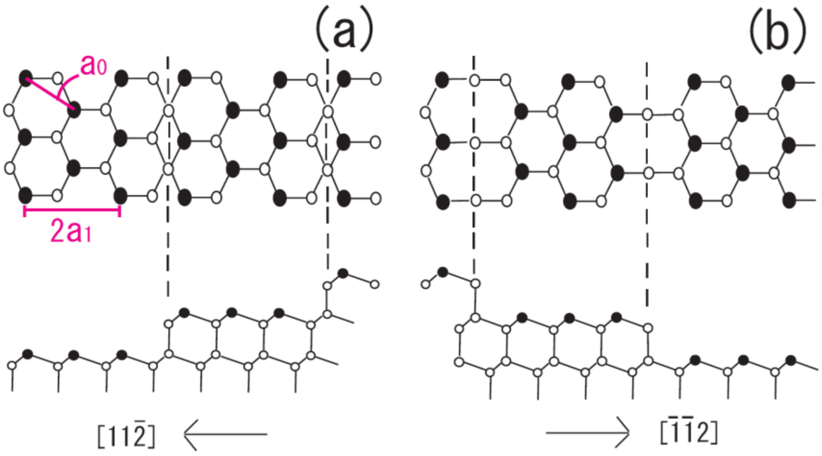

Figure 2.3 Atomic structure models of ideally truncated surfaces of vicinal Si(111) misoriented toward (a) $[11\bar{2}]$ and (b) $[\bar{1}\bar{1}2]$ directions, respectively. The upper panels are top views, and the lower are side views [24].

this temperature is too high, i.e., too close to the 7×7-to1×1 phase transition at ~870^{o}C, some of the single steps convert to triple steps. Arrays of bunched steps occur for miscut towards $[11\bar{2}]$ direction, with adjustable height (1-5 nm) and a spacing of 70 nm. By taking into account several parameters such as miscut angle, annealing sequence, current direction, external stress; straight edges and regular spacing can be obtained [12, 26].

2.3 Low-dimensional structures

The most commonly used techniques for the preparation of LD nanostructures are lithography, electrochemical deposition and self-organised growth on structured or stepped surfaces. The conventional lithographic methods use UV light from excimer lasers. The structure size is limited by the wavelength of the laser light (currently λ = 193 nm or 157 nm). The node size in commercially available CMOS devices is 45 nm - already below the diffraction limit of $\lambda/2$. This can only be achieved by an enormous precision in the manufacturing steps and huge effort in mask design. Other lithographic methods such as electron beam lithography, or the direct scratching of the photoresist using an atomic force or scanning tunnelling microscope can produce much smaller structures, but not in large quantities or on large areas as required for device production. A promising approach to reduce the structure size with conventional lithographic techniques is EUV-lithography (extreme ultraviolet, 13 nm), [27, 28].

Other methods of growing nanostructures have been discussed recently [29, 30]. Metallic nanowires can be grown by electrochemical deposition of metals in structured membranes which are then dissolved in later production steps [29, 31, 32]. The width of wires produced in such a way is determined by the membrane pore size and the length by its thickness. Currently, the only way to produce large areas of organised nanostructures of minimum dimension <5 nm is by self-assembly on structures substrates, particularly stepped surfaces.

2.3.1 Self-organised epitaxial growth

Self-organised epitaxial growth or epitaxial self-assembly may occur on crystalline substrates under favourable conditions. The driving force for the self-organization process during heteroepitaxial growth of films of more than a few monolayers (ML) thickness is the misfit between the crystal lattice of the growing layer and that of the substrate, which creates strain in the growing layer. In the initial stage of growth, a pseudomorphic thin layer is created, which is elastically distorted. During growth the elastic energy stored in this layer increases. In general, either plastic or elastic relaxation of this internal elastic energy is possible. During plastic relaxation, the elastic energy is reduced by misfit dislocations at the substrate/layer interface; this process competes with elastic relaxation leading to self-organized nanostructures. Elastic energy relief is important for the formation of self-assembled nanostructures, and this in turn depends substantially on layer thickness. For layer thicknesses of only a few MLs, the elastic energy may be reduced by surface reconstruction. The clean surface of a crystalline substrate is often reconstructed in relation to a bulk exposed plane. Heterogeneous adsorption then leads to further reconstruction, producing an adsorbate induced surface superstructure.

2.3.2 Metal-induced reconstructions as templates for LD growth

Surface superstructures induced by metal adsorption on semiconductor surfaces have now become important platforms for exploring LD physics as well as applications to nanotechnology. With various combinations of metal adsorbates and semiconductor substrates an abundance of ordered surface phases has been reported, some of which exhibit intriguing physical properties. Different adsorbates and atomic arrangements form different surface electronic states. Since the surface superstructures generally involve one or two surface atomic layers, their surface state bands are inherently two dimensional. One-dimensional electronic bands may be created due to strongly anisotropic atomic arrangements in surface superstructures. For nano-structural fabrication, usually a thin epilayer is grown on a substrate. This two-dimensional (2D) layer may be used to fabricate lower dimensional structures like wires (1D) or dots (0D) by lithographic techniques. However, structures smaller than the limits of lithographic techniques can only be obtained by assembled growth utilizing the principles of Stranski-Krastanov (SK) or Volmer Weber (VW) growth. Small islands can exhibit unusual quantum confinement effects, which make them useful in electrical devices as single electron transistors and optical devices.

The use of more complex crystalline templates opens up more possibilities of LD epitaxial growth of metallic and semiconducting structures. This is demonstrated on Si(111)-3×1-Ag [33, 34], where the Si(111)-3×1-Ag surface is used as a template for growing 1nm sized Ag quantum dots, with a preferential spacing of 1.5 nm along the rows. Other structures include Er silicode wires on Si(001) as templates for deposition of platinum [35], 1D In islands on Bi/Si(001) system [36]. Adsorption of a larger quantity of metal atoms on surfaces can lead to the formation of islands. The shape of the islands formed may depend not only on the adsorbate and substrate material, but also on the surface orientation and reconstruction before adsorption. In some cases it is possible to grow larger anisotropic islands. Examples are the formation of Sn islands on InAs(110) [37] or Pb islands on Si(335) [38], Ag islands on Si(111)-3×1-Ag [33], InGaAs islands on GaAs [39]. In these systems the island size and also shape is determined by the amount of metal deposited. The width, height and length of the island change when more material is deposited. With appropriate growth conditions, self-assembled epitaxial islands can be grown in reasonably well-controlled sizes. A narrow size distribution is essential for most optoelectronic applications. The ability to grow such size-controlled islands is an attractive feature of self-assembly, although the positions of individual islands cannot be determined precisely. Since precise placement of islands is not required for many devices, self-assembly is an attractive route for the fabrication of devices based on nanostructures.

2.3.3 Nucleation of islands on silicon surfaces

Growth of surface structures as described above involves deposition of atoms onto a surface, subsequent diffusion of those adatoms on the surface, and eventually nucleation of adatom clusters, commonly called islands. As atoms are deposited onto a surface they are adsorbed and begin to migrate at non-zero temperatures. Nucleation proceeds as long as adatoms form new islands instead of attracting to the existing ones. A stationary state is reached when the number of islands N remains constant and only island size changes. N scales as a power-law with respect to the surface diffusion coefficient D and the incoming flux F [40, 41] . This implies that the surface diffusion coefficient D can be found by measuring the number of islands on a surface. The scaling relation is given by [40]

$$N \sim \frac{D}{F}^{-x} \tag{2.1}$$

where x is the scaling exponent which depends on the spatial dimension d, various microscopic surface processes and the critical island size. For islands on a singular surface, the relevant length scale is determined by the typical distance between islands l_n, which is set during submonolayer deposition. Incoming adatoms nucleate new islands, since in this initial stage of growth there are no steps or islands present where newly landed adatoms could attach. Nucleation terminates when a saturation regime is reached, and all incoming adatoms attach to already existing islands. Consequently, the total number of islands remains constant.

If one assumes stable and immobile dimers, the nucleation length on a singular surface is given by [42]

$$l_n \sim \left(\frac{D}{F}\right)^{1/6} \tag{2.2}$$

where D is the adatom diffusion coefficient and F is the flux. When island growth occurs on terraces of a vicinal surface, the terrace width L appears also as a length scale. On a terrace with smaller L most adatoms attach to the step edge and only a few islands appear [43]. On a vicinal surface in the limit of large terraces, $L>>l_n$, in the submonolayer regime, the island density N (number of islands per unit area) will scale as on a singular surface,

$$N = \frac{1}{l_n^2} \sim \left(\frac{F}{D}\right)^{1/3} \tag{2.3}$$

As the terrace width decreases, adatoms attach preferentially to steps instead of nucleating new islands. If L is small enough (step-dominated nucleation), only one island fits between the edges of neighbouring steps. The nucleation length of the islands on a small terrace is given by [44]

$$\tilde{l}_n \sim \left(\frac{D}{F}\right) L^{-5} \tag{2.4}$$

and consequently the island density in this regime is given by

$$\tilde{N} = \frac{1}{\tilde{l}_n L} \sim \frac{FL^4}{D} \tag{2.5}$$

Setting the expressions for the island densities equal, $N = \tilde{N}$, results for a cross-over value of the flux $F_c = D/L^6$, or the terrace width $L_c = (D/F)^{1/6}$. During the nucleation period the distance between the islands decreases until the saturation density is reached.

2.3.4 Electronic properties of LD structures

In LD systems, confinement of the electrons in at least one dimension strongly modifies the properties of the system. Low dimensions amplify the role of quantum fluctuations and enhance correlations. Both the ground state and the excitations exhibit strong correlation effects and possess a number of exotic properties, such as charge density waves (CDWs), Peierls instabilities, or the formation of non-Fermi-liquid-like ground states [45-48].

The Fermi liquid picture can describe the properties of bulk metals very well. The key observation is that, at normal temperatures, the macroscopic properties involve only excitations of the system on an energy scale small compared to the Fermi energy. The state of the system can be specified in terms of its ground state, i.e. the Fermi surface, and lowlying elementary excitations-a rarefied gas of ‘quasi-particles’. These quasi-particles evolve continuously out of the states of a free Fermi gas when interactions are switched on adiabatically, and are in one-to-one correspondence with the bare particles (adiabatic continuity). They possess the same quantum numbers as the original particles, but their dynamical properties are modified by the interactions. This scenario emerges because the phase space for scattering of particles is severely restricted by Fermi statistics: at low temperatures ($T/E_F << 1$) most particles are frozen inside the Fermi sea, and only a fraction participate in the scattering processes. The restriction to lowlying excitations, implying low densities of excitations, and Fermi statistics are enough to ensure Fermi Liquid properties. In an ideal 1D system, the only possible scattering requires full momentum transfer. Hence interactions between single electrons will be much larger than in the 2D and 3D case. On the microscopic level, the central problem in the theory of interacting electrons is the Peierls instability. For a strictly 1D metal, a model of the band structure and the Fermi surface is shown in figure 2.4 (left). Assuming the band is crossing the Fermi level at half the Brillouin zone, it can be seen that any periodic distortion with a periodicity of 2 real space unit cells will lead to a backfolding of the band at the new zone boundary. This is always accompanied with an energy gain of electrons at the Fermi surface of ΔE_P due to the opening of a gap as depicted in figure 2.4 (right). The argument can be similarly formulated for any k_F, though the distortion then involves more than two unit cells. Peierls and Frohlich discussed these phenomena in terms of the electron-phonon interaction. The periodic lattice distortion of $2k_F$ leads to the energy gain and a periodic modulation of the charge called a charge density wave (CDW) [49]. This instability of 1D metallic structures against CDWs accompanied with periodic lattice distortions (or vice versa) is now known as Peierls instability. For electrons in 1D, any many-body interaction that causes a $2k_F$ distortion would lead to a more stable configuration than the metallic band. Repulsive electron-electron interaction would lead to similar effects eg. the Mott transition. Also, a periodic modulation of the spins – a spin density wave (SDW) – would lead to an energetically favoured configuration and an opening of a pseudogap at k_F. In addition, the well-known 3D BCS-singularity (Bardeen, Cooper and Schrieffer [50]) can also occur in 1D leading to Cooper pair formation and superconductivity [51]. Calculations are more complicated in this case, since the formation of a static CDW leading to an insulating ground state, and Cooper pairs leading to superconductivity are competing processes. Mean field theories can only describe one of them.

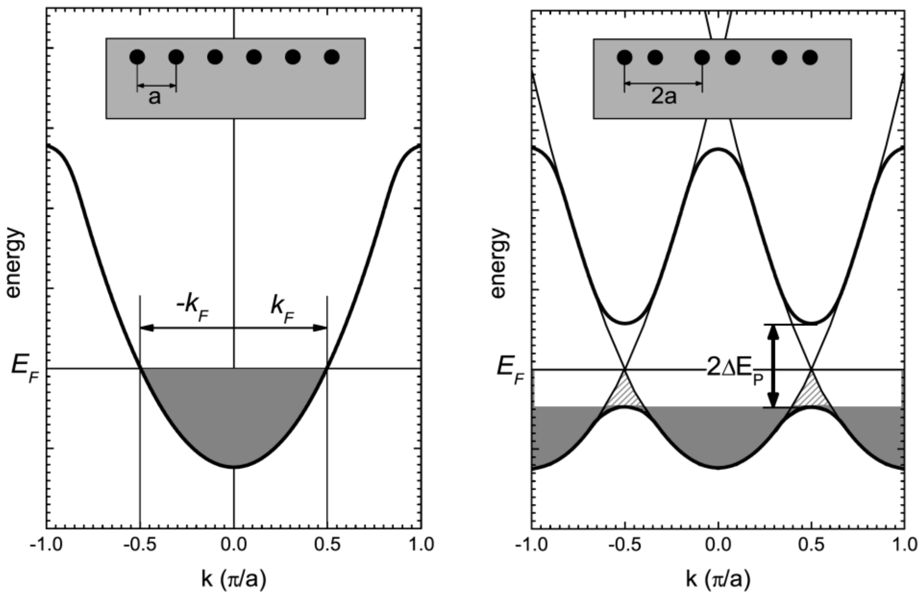

Figure 2.4 Graphical explanation of the energy gain at the Peierls transition. A system with a parabolic metallic state with $k_F=1/2(\pi/a)$ can gain energy by a distortion of periodicity 2a. The backfolding of the band leads to a gap opening at $1/2(\pi/a)$ with a Peierls gap (ΔE_P). Since no filled states exist above the new found valence band the system gains energy as depicted by the shaded area. The total energy gain though depends on the density of states around the Fermi vector k_F [54] .

2.4 Optical properties of LD structures

For bulk semiconductors the most important contribution to the dielectric function in the visible spectral range is interband transitions. The dielectric function ε of Si is shown in figure 2.5 (left). The maxima in ε can be attributed to certain transitions within the electronic band structure as shown in the right graph of figure 2.5. The absorption and also $\mathrm{Im}(\varepsilon)$ are large whenever the joint density of states (JDOS) is maximised. The two features at about 3.5 eV and 4.3 eV are labeled E_1 and E_2 and are related to aspects of the band structure as shown in the right hand graph of figure 2.5. The band edge absorption is completely negligible compared to the absorption coefficient in the spectral region around E_1 and E_2. This is a consequence of two factors. Firstly, the band edge absorption is weak because it is indirect, and secondly, the density of states at the band edge is comparatively small. The measured absorption is dominated by direct, k-conserving transitions at photon energies where the density of states is high. The band gap E_g is indirect and has a value of 1.1 eV, with the conduction band minimum located near X-point of the Brillouin zone. Direct transitions can take place between any state in the valence band and the conduction band states vertically above it, if the transitions are dipole allowed. The minimum direct

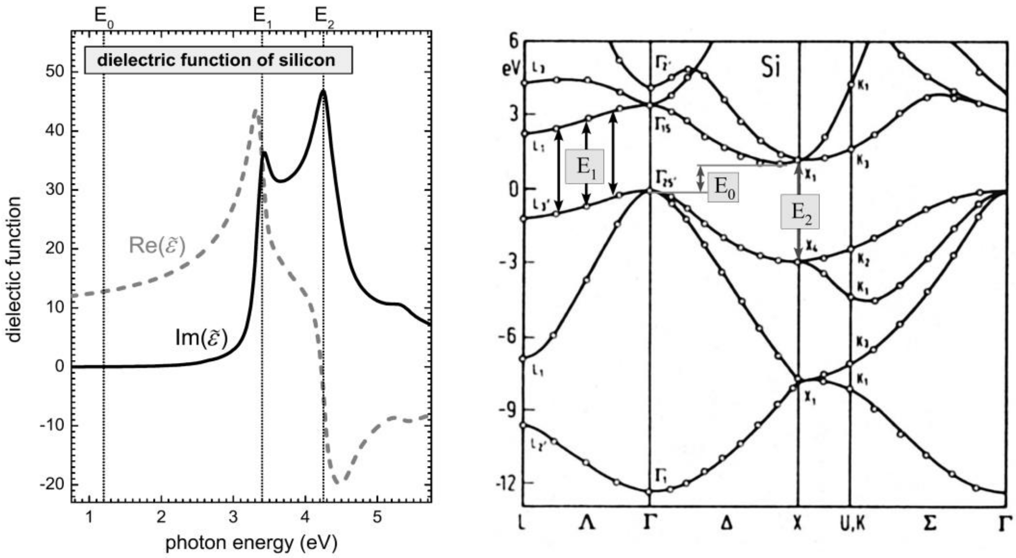

Figure 2.5 The dielectric function of silicon (left) solid line: imaginary part, dotted line: real part. In the right image the main transitions contributing to the bulk critical points are depicted by arrows in the bulk band structure [54].

separation between the conduction and valence bands occurs near the L point, where the transition energy is 3.4 eV. The energy of these transitions is labelled E_1, and corresponds to the sharp increase in the absorption at 3.4 eV, observed in the data shown in figure 2.5 (left). The separation of the conduction and valence bands near the X point is also significant. This energy is labelled E_2 and corresponds to absorption maximum at 4.3 eV [52]. The transitions near the L and X points are particularly important because of the ‘camel’s back’ shape of the conduction band, leading to conduction and valence bands being approximately parallel to each other. The joint density of states factor is therefore very high at E_1 and E_2. The maxima in the JDOS or Im(ε) are usually called critical point energies.

For the discussion of the optical properties of nanowires there are two important points regarding the interband transitions. Firstly, since no free standing nanowires are investigated, the reflectivity of the substrate will the influence optical measurements. Optical models will have to be developed to relate structures in the measured spectra to the wires themselves. Secondly, the interband transitions of the nanowire will differ from the bulk, and will vary with size of the wire. Models are needed in order to relate structures in the optical spectra to the properties of the nanowires

2.4.1 Drude-Lorentz oscillator

The simplest models of absorption and dispersion are due to Lorentz and Drude. The Lorentz model can be applied to direct interband transitions; i.e., all transitions for which the final state of an electron lies in a different band but with no change in k-vector in the reduced zone scheme. The Drude model can be applied to intraband transitions.

Within the the Lorentz model, the dielectric response at frequency ω for an isotropic medium is given by

$$\begin{aligned} \varepsilon' &= 1 + \frac{4\pi N e^2}{m} \frac{\left(\omega_0^2 - \omega^2\right)}{\left(\omega_0^2 - \omega^2\right)^2 + \Gamma^2 \omega^2} \\ \varepsilon'' &= \frac{4\pi e^2}{m} \frac{\Gamma \omega}{\left(\omega_0^2 - \omega^2\right)^2 + \Gamma^2 \omega^2} \end{aligned} \tag{2.6}$$

where ε' and ε'' are the real and imaginary part of the dielectric function, N denotes the charge density, m the electron mass, Γ the damping factor, e the electron charge and ω_0 is the oscillator position where absorption is maximum.

The region below the interband transitions can be assumed to be nearly free-electron-like and can be described within the Drude model, which describes the absorption of an electron gas. The Drude model for metals is obtained directly from the Lorentz model by equating the restoring force to zero as the conduction electrons of a metal are assumed not to be bound. Furthermore, because the wavefunction for a free electron is distributed fairly uniformly throughout the metal, the field acting is just the average field. Taking $\omega_0 = 0$, equation (2.6) becomes

$$\begin{aligned} \varepsilon' &= 1 - \frac{4\pi N e^2}{m} \frac{1}{\left(\omega^2 + \Gamma^2\right)} \\ \varepsilon'' &= \frac{4\pi N e^2}{m} \frac{\Gamma}{\omega\left(\omega^2 + \Gamma^2\right)} \end{aligned} \tag{2.7}$$

The origin of the viscous damping term for a free-electron metal is the ordinary scattering of electrons associated with electrical resistivity. The scattering rate or damping factor, Γ, can be replaced by τ^{-1}, where τ is the inelastic scattering relaxation time. In the Drude model the scattering rate of the electrons is not explained, since the electrons are assumed to be non-interacting. In the Fermi liquid picture introduced earlier this is changed. The electron-electron and electron-phonon interactions can be included in this model and the scattering rate quantitatively described [53]. The Drude function for the free carrier absorption remains valid. The Drude model of non-interacting electrons is a rather crude model. Nevertheless the agreement with the IR response of metals and also doped semiconductors is astonishing if the electron mass is replaced by the effective mass, m^*, which accounts for interactions of the electrons with the screened core potentials. In figure 2.6 ε'' is shown for several metals [54].

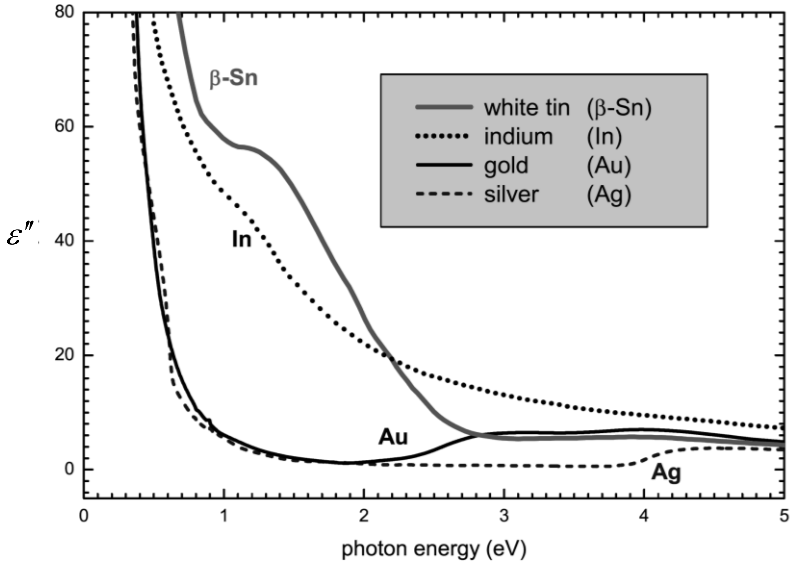

Figure 2.6 Imaginary part of the dielectric function for various metals. For all metals the characteristic Drude tail of the free carrier absorption is observed in the infrared. Additional structures arise from interband transitions [54].

.

Quasi-1D nanowires are structurally anisotropic and are expected to produce an anisotropic optical response. The optical anisotropy is most simply described by anisotropic values of the effective masses and/or scattering rates. The full anisotropic dielectric function, ε_i, can be described by the combination of Drude term and Lorentz oscillators, which account for the intraband absorption of the free electrons and the interband absorptions, respectively:

$$\begin{aligned}
\varepsilon_i' &= 1 - \frac{\omega_p^2}{\left(\omega^2 + \Gamma_i{}^2\right)} + \sum_{j=1}^{n} \frac{A_i\left(\omega_{0,i}^2 - \omega^2\right)}{\left(\omega_{0,i}^2 - \omega^2\right)^2 + \Gamma_i^2\omega^2} \\
\varepsilon_i'' &= \frac{\omega_p^2\Gamma_i}{\omega\left(\omega^2 + \Gamma_i{}^2\right)} + \sum_{j=1}^{n} \frac{A_i\Gamma_i\omega}{\left(\omega_{0,i}^2 - \omega^2\right)^2 + \Gamma_i^2\omega^2}
\end{aligned} \qquad (2.8)$$

for $i=x, y$ in the surface plane. Here, the amplitude A_i is proportional to the oscillator strength, Γ_i is the damping, $\omega_p^2 = 4\pi Ne^2 / m^*\varepsilon_\infty$ is the plasma frequency squared and m^* is the effective mass. The parameters can be adjusted to give optimal values by least square fitting to the experimental data.

References

1. Hasegawa S: **Surface-state bands on silicon as electron systems in reduced dimensions at atomic scales.** *Journal of Physics Condensed Matter* 2000, **12:**R463-495.
2. Takayanagi K, Tanishiro Y, Takahashi M, Takahashi S: **Structural analysis of Si(111)-7*7 by UHV-transmission electron diffraction and microscopy.** *Journal of Vacuum Science and Technology A (Vacuum, Surfaces, and Films)* 1985, **3:**1502-1510.
3. Woodruff DP: **Solved and unsolved problems in surface structure determination.** *Surface Science* 2002, **500:**147-171.
4. Haneman D: **Surfaces of silicon.** *Reports on Progress in Physics* 1987, **50:**1045-1086.
5. Binnig G, Rohrer H, Gerber C, Weibel E: **7*7 reconstruction on Si(111) resolved in real space.** *Physical Review Letters* 1983, **50:**120-123.
6. Culbertson RJ, Feldman LC, Silverman PJ: **Atomic displacements in the Si(111)-(7*7) surface.** *Physical Review Letters* 1980, **45:**2043-2046.
7. Tromp RM, van Loenen EJ, Iwami M, Saris FW: **On the structure of the laser irradiated Si(111)-(1*1) surface.** *Solid State Communications* 1982, **44:**971-974.
8. Aono M, Souda R, Oshima C, Ishizawa Y: **Structure analysis of the Si(111)7*7 surface by low-energy ion scattering.** *Physical Review Letters* 1983, **51:**801-804.
9. Tromp RM, Hamers RJ, Demuth JE: **Atomic and electronic contributions to Si(111)-(7*7) scanning-tunneling-microscopy images.** *Physical Review B (Condensed Matter)* 1986, **34:**1388-1391.
10. Chou MY, Cohen ML, Louie SG: **Theoretical study of stacking faults in silicon.** *Physical Review B (Condensed Matter)* 1985, **32:**7979-7987.
11. Robinson IK, Waskiewicz WK, Fuoss PH, Stark JB, Bennett PA: **X-ray diffraction evidence of adatoms in the Si(111)7*7 reconstructed surface.** *Physical Review B (Condensed Matter)* 1986, **33:**7013-7016.
12. Viernow J, Lin A-L, Petrovykh DY, Leibsle FM, Men FK, Himpsel FJ: **Regular step arrays on silicon.** *Applied Physics Letters* 1998, **72:**948-950.
13. Teichert C: **Self-organization of nanostructures in semiconductor heteroepitaxy.** *Physics Reports* 2002, **365:**335-432.
14. Gambardella P, Blanc M, Brune H, Kuhnke K, Kern K: **One-dimensional metal chains on Pt vicinal surfaces.** *Physical Review B (Condensed Matter)* 2000, **61:**2254-2262.
15. Gambardella P, Blanc M, Burgi L, Kuhnke K, Kern K: **Co growth on Pt(997): from monatomic chains to monolayer completion.** *Surface Science* 2000, **449:**93-103.
16. Yater JE, Shih A, Idzerda YU: **Structural characterization of stepped Ga/Si(112) surfaces.** *Physical Review B: Condensed Matter* 1995, **51:**7365.
17. McChesney JL, Kirakosian A, Bennewitz R, Crain JN, Lin J-L, Himpsel FJ: **Gd disilicide nanowires attached to Si(111) steps.** *Nanotechnology* 2002, **13:**545-557.
18. Himpsel FJ, Altmann KN, Bennewitz R, Crain JN, Kirakosian A, Lin JL, McChesney JL: **One-dimensional electronic states at surfaces.** *Journal of Physics-Condensed Matter* 2001, **13:**11097-11113.
19. Segovia P, Purdie D, Hengsberger M, Baer Y: **Observation of spin and charge collective modes in one-dimensional metallic chains.** *Nature* 1999, **402:**504-507.
20. Himpsel FJ, Mo YW, Jung T, Ortega JE, Mankey GJ, Willis RF: **Quantum well and quantum wire states at metal surfaces.** *Superlattices and Microstructures* 1994, **15:**237-245.

21. Jung T, Schlittler R, Gimzewski JK, Himpsel FJ: **One-dimensional metal structures at decorated steps.** *Applied Physics a (Materials Science Processing)* 1995, **61:**467-474.
22. Phaneuf RJ, Williams ED: **Step-height-tripling transition on vicinal Si(111).** *Physical Review B (Condensed Matter)* 1990, **41:**2991-3003.
23. Goldberg JL, Wang XS, Wei J, Bartelt NC, Williams ED: **Quantization of terrace widths on vicinal Si(111).** *Journal of Vacuum Science and Technology A (Vacuum, Surfaces, and Films)* 1991, **9:**1868-1873.
24. Okino H, Matsuda I, Tanikawa T, Hasegawa S: **Formation of facet structures by Au adsorption on vicinal Si(111) surfaces.** *e-Journal of Surface Science and Nanotechnology* 2003, **1**.
25. Becker RS, Golovchenko JA, McRae EG, Swartzentruber BS: **Tunneling images of atomic steps on the Si(111)7*7 surface.** *Physical Review Letters* 1985, **55:**2028-2031.
26. Lin JL, Petrovykh DY, Viernow J, Men FK, Seo DJ, Himpsel FJ: **Formation of regular step arrays on Si(111)7*7.** *Journal of Applied Physics* 1998, **84:**255-260.
27. Qian T, San-Qiang S, Limin Z: **Nanofabrication with atomic force microscopy.** *Journal of Nanoscience and Nanotechnology* 2004, **4:**948-963.
28. Fay B: **Advanced optical lithography development, from UV to EUV.** *Microelectronic Engineering* 2002, **61-62:**11-24.
29. Kovtyukhova NI, Mallouk TE: **Nanowires as building blocks for self-assembling logic and memory circuits.** *Chemistry - A European Journal* 2002, **8:**4354-4363.
30. Murphy CJ, Jana NR: **Controlling the aspect ratio of inorganic nanorods and nanowires.** *Advanced Materials* 2002, **14:**80-82.
31. Martin BR, Dermody DJ, Reiss BD, Fang M, Lyon LA, Natan MJ, Mallouk TE: **Orthogonal self-assembly on colloidal gold-platinum nanorods.** *Advanced Materials* 1999, **11:**1021-1025.
32. Wirtz M, Martin CR: **Template-fabricated gold nanowires and nanotubes.** *Advanced Materials* 2003, **15:**455-458.
33. Hirayama H, Horie R, Takayanagi K: **Nucleation of Ag nanodots at the Si(111)3*1-Ag surfaces.** *Surface Science* 2001, **482-485:**1277-1282.
34. Kuntze J, Mugarza A, Ortega JE: **Ag-induced zero- and one-dimensional nanostructures on vicinal Si(111).** *Applied Physics Letters* 2002, **81:**2463-2465.
35. Ragan R, Kim S, Li X, Williams RS: **Platinum passivation of self-assembled erbium disilicide nanowire arrays on Si(001).** *Applied Physics A: Materials Science and Processing* 2005, **80:**1339-1342.
36. Owen JHG, Miki K: **One-dimensional epitaxial growth of indium on a self-assembled atomic-scale bismuth template.** *Nanotechnology* 2006, **17:**430-433.
37. Fleischer K, Chandola S, Herrmann T, Esser N, Richter W, McGilp JF: **Free-electron response in reflectance anisotropy spectra.** *Physical Review B (Condensed Matter and Materials Physics)* 2006, **74:**195432-195410.
38. Strozak M, Hnatyuk V, Jalochowski M: **Optical properties of Pb nanowires on Si(3 3 5).** *Vacuum* 2004, **74:**241-245.
39. Leonard D, Krishnamurthy M, Reaves CM, Denbaars SP, Petroff PM: **Direct formation of quantum-sized dots from uniform coherent islands of InGaAs on GaAs surfaces.** *Applied Physics Letters* 1993, **63:**3203.
40. Venables JA, Spiller GDT, Hanbucken M: **Nucleation and growth of thin films.** *Reports on Progress in Physics* 1984, **47:**399-459.
41. Pimpinelli A, Villain J, Wolf DE: **Fractal terraces in MBE growth.** *Journal de Physique I (General Physics, Statistical Physics, Condensed Matter, Cross-Disciplinary Physics)* 1993, **3:**447-457.

42. Pimpinelli A, Villain J: *Physics of crystal growth.* Cambridge : Cambridge University Press; 1998.
43. Bales GS: **Crossover scaling during submonolayer epitaxy on vicinal substrates.** *Surface Science* 1996, **356:**439-444.
44. Rusanen M, Koponen IT, Kallunki J: **Mixing length scales: Step meandering and island nucleation on vicinal surfaces.** *European Physical Journal B* 2003, **36:**141-147.
45. Yeom HW, Takeda S, Rotenberg E, Matsuda I, Horikoshi K, Schaefer J, Lee CM, Kevan SD, Ohta T, Nagao T, Hasegawa S: **Instability and charge density wave of metallic quantum chains on a silicon surface.** *Physical Review Letters* 1999, **82:**4898-4901.
46. Yeom HW, Horikoshi K, Zhang HM, Ono K, Uhrberg RIG: **Nature of the broken-symmetry phase of the one-dimensional metallic In/Si(111) surface.** *Physical Review B (Condensed Matter and Materials Physics)* 2002, **65:**241307-241301.
47. Tsay SF: **Atomic and electronic structure of the (4*1) and (8*2) In/Si(111) surfaces.** *Physical Review B (Condensed Matter and Materials Physics)* 2005, **71:**35207-35201.
48. Gonzalez C, Ortega J, Flores F: **Metal-insulator transition in one-dimensional in-chains on Si(111): combination of a soft shear distortion and a double-band Peierls instability.** *New Journal of Physics* 2005, **7**.
49. Peierls RE, Sir, 1907- *Quantum theory of solids* Oxford : Clarendon University Press 1955.
50. Bardeen J, Cooper LN, Schrieffer JR: **Theory of superconductivity.** *Physical Review* 1957, **108:**1175-1203.
51. Voit J: **One-dimensional Fermi liquids.** *Reports on Progress in Physics* 1995, **58:**977-1116.
52. Yu PY, Cardona M: *Fundamentals of semiconductors 2. rev. ed.. Physics and materials properties.* Springer; 1999.
53. Kittel C: *Introduction to solid state physics, 5th edition.* Wiley; 1976.
54. Fleischer K: **Optical anisotropy and vibrational properties of Sn, In and Cs nanowires.** PhD thesis, Technischen Universitat 2005.

3

Phenomenology of RAS and SHG

3.1 Overview

The first half of this chapter deals with a more detailed discussion of RAS phenomenology. The second half deals with SHG and the phenomenological theories relevant to this work.

3.2 Optical response of materials

The interaction of an EM field of optical frequencyω, with condensed matter can be described in terms of the polarization amplitude, $P(\omega, 2\omega, ...)$, induced by the field, $E(\omega)$:

$$P(k, \omega, 2\omega, ..) = \varepsilon_0 \left[\chi^{(1)}(k, \omega) : E(k, \omega) + \chi^{(2)}(k, \omega, 2\omega) : E^2(k, \omega) + ... \right] \qquad (3.1)$$

$\chi^{(i)}$ is the *i*-th order dielectric susceptibility tensor describing the material response. The intensity of the EM radiation emitted depends on the square of the polarization amplitude. The first term on the right hand side of the equation, which depends linearly on the field, describes the linear optical response, is exploited in techniques like spectroscopic ellipsometry and RAS. The nonlinear terms in the equation becomes significant at high EM field strengths, and the second term in equation (3.1) has a polarization, which depends on the square of the EM field, describes the lowest order nonlinear optical response responsible for SHG.

3.3 Reflectance anisotropy spectroscopy

Reflection anisotropy spectroscopy (RAS) is a non-destructive optical probe of surfaces capable of operation within a wide range of environments. It achieves its surface sensitivity by a measurement of the difference in reflection of normal incidence plane polarised light in two directions at right angles, from the surface of a cubic crystal. The optical response of bulk signal cancels by symmetry leaving a signal that arises from the lower symmetry of the surface. The surface sensitivity of RAS has been demonstrated on silicon surfaces with observations of surface reconstruction [1, 2], dimer orientations [1, 3], atomic steps [4-6] and strain [7]. The technique has been used to study adsorption on metals [8-11], semiconductor surfaces [12-16] orientation of organic molecules bonded to metal surfaces [17, 18], alkali-induced surface reconstruction [19] and high pressure semiconductor growth [20]. An extensive review of RAS has appeared recently [21].

3.3.1 Analysis

RAS is one of a handful of techniques, including photoluminescence, and spectroscopic ellipsometry, that depend on $\chi^{(1)}$ (equation (3.1)). As mentioned earlier, it measures the difference in the near normal incidence (≈5^0) reflectance of linearly polarised light along two orthogonal axes in the surface plane of a crystal.

The geometry of such an arrangement is shown in figure 3.1. Here, E_p refers to light polarised in the plane of incidence, and E_s to light polarised perpendicular to the plane of incidence. Reflection from such a surface is described by the well-known Fresnel equations which can be found in [22].

In a strict sense, a surface that has reconstructed may be considered to be an interface between two crystals with dielectric tensor components ε_{ixx}, ε_{iyy}, and ε_{izz}. ε_{ixx} is the *x* response of the dielectric tensor to *x* components of the incident beam in medium *i*, with *i* = 1 (surface or thin film) or 2 (bulk substrate), and *x* and *y* are defined as in the surface plane and *z* perpendicular to it (figure 3.1). If the bulk material or substrate is isotropic, then the tensor components are the same along each material axis. This allows ε_{2jj}, where

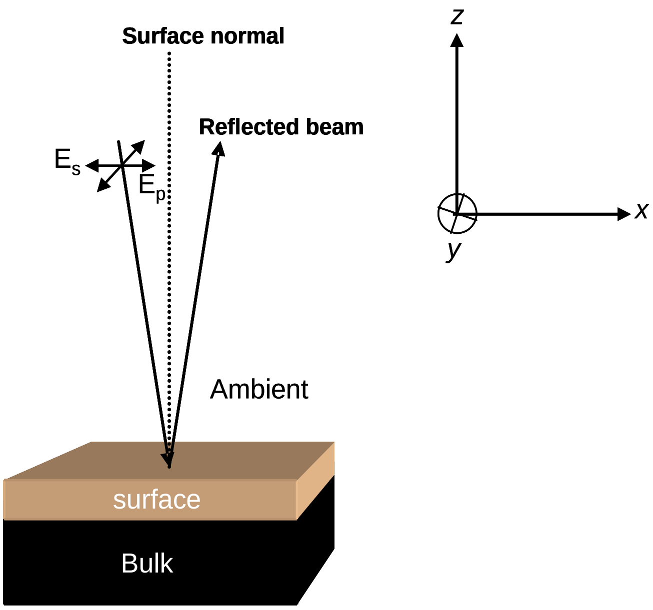

Figure 3.1 Reflection geometry from a three-phase system, with an exaggerated representation of the angles of incidence and reflection.

j = x, y or z, to be replaced by the single component ε_b, the isotropic bulk dielectric constant. The division of the sample into three distinct regions, bulk, thin film and vacuum, is known as the three-phase model [23] (figure 3.1).

Using this anisotropic three phase model and the Fresnel equations, expressions may be derived for the *s*- and *p*-polarised light from such a surface [23]. As RAS is only concerned with the reflectance of *p*-polarised light from a *p*-polarised incident beam, only that equation will be quoted.

$$\frac{r_{pp}(\phi_0,\psi)}{r^0_{pp}} = 1 + \frac{i4\pi d\cos\phi_0}{\lambda(\varepsilon_b-1)(\varepsilon_b\cos^2\phi_0-\sin^2\phi_0)}[(\varepsilon_b-\bar{\varepsilon})\varepsilon_b - \left(\left(\frac{\varepsilon_b^2}{\varepsilon_{zz}}\right)-\bar{\varepsilon}\right)\sin^2\phi_0 + \Delta\varepsilon(\varepsilon_b-\sin^2\phi_0)\cos 2\psi] \tag{3.2}$$

where

$$\varepsilon = \frac{\varepsilon_{xx}+\varepsilon_{yy}}{2} \text{ and } \Delta\varepsilon = \frac{\varepsilon_{yy}-\varepsilon_{xx}}{2}$$

r^0_{pp} = complex bulk reflection coefficient of *p*-polarised light from p-polarised incident beam

r_{pp} = complex surface reflection coefficient of *p*-polarised light from p-polarised incident beam

ϕ_0 =angle of incidence

ψ = azimuthal angle with respect to the place of incidence

d = surface thickness

and ε_{ixx} has been replaced with ε_{xx}, etc.

In the normal incidence case ϕ_o is 0 and this equation simplifies to:

$$\frac{r_{pp}(\phi_0,\psi)}{r_{pp}} = 1 + \frac{i4\pi d}{\lambda(\varepsilon_b - 1)}\left[\varepsilon_b - \bar{\varepsilon} + \Delta\varepsilon\cos 2\psi\right] \tag{3.3}$$

RAS measures:

$$\frac{\Delta r}{r} = 2\frac{r_{pp}\left(0^0,90^0\right) - r_{pp}\left(0^0,0^0\right)}{r_{pp}\left(0^0,90^0\right) + r_{pp}\left(0^0,0^0\right)} \tag{3.4}$$

where *Δr* is the difference in complex reflection coefficient between the two axes, and *r* is their average [24, 25].

Now, $r_{pp}\left(0^0,90^0\right) = 1 + \frac{i4\pi d}{\lambda(\varepsilon_b - 1)}\left[\varepsilon_b - \varepsilon_{yy}\right]$

and

$$r_{pp}\left(0^0,0^0\right) = 1 + \frac{i4\pi d}{\lambda(\varepsilon_b - 1)}\left[\varepsilon_b - \varepsilon_{xx}\right]$$

giving on substitution into equation (3.3),

$$\frac{\Delta r}{r} = \frac{i4\pi d(\varepsilon_{xx} - \varepsilon_{yy})}{\lambda(\varepsilon_b - 1)} \tag{3.5}$$

where *d* is the depth of the anisotropic surface region (medium 1) and λ the incident light wavelength. The quantity $d\left(\varepsilon_{xx} - \varepsilon_{yy}\right)$ is called the surface dielectric anisotropy (SDA). The SDA is a well defined quantity, while determining the surface dielectric function requires an assumption about the depth of the surface region. Equation (3.5) thus relates the measured RAS response to the product of the anisotropic dielectric function of the surface region and its depth. Models of the dielectric response were discussed in chapter 2, section 2.4.1. The real part of $\Delta r / r$ is commonly measured, and equation (3.5) gives

$$\mathrm{Re}\left(\frac{\Delta r}{r}\right) = \frac{4\pi d}{\lambda}\mathrm{Im}\left(\frac{(\varepsilon_{xx} - \varepsilon_{yy})}{(\varepsilon_b - 1)}\right) \tag{3.6}$$

3.4 Second harmonic generation

3.4.1 Nonlinear response

The electric polarisation $P(k,\omega)$ induced in a material by an electromagnetic field $E(k,\omega)$ is given by equation (3.1). Third harmonic generation, which depends on $\chi^{(3)}$, is a bulk probe in the absence of any strong resonantly-enhanced surface electric dipole effects, while higher order nonlinearities are too small to be detected, except for extremely short pulses [26]. Second harmonic generation (SHG) and other three-wave mixing phenomena, which depend on $\chi^{(2)}$, are potentially surface sensitive at non-destructive power densities [27, 28]. This is most easily seen for centrosymmetric materials where, in the standard multipole expansion of fields, the electric dipole term is parity forbidden, leaving only higher order contributions such as those from magnetic dipole and electric quadrupole effects. At a surface or interface the bulk symmetry is broken and electric dipole effects are allowed. An order of magnitude calculation shows that the surface effect should be at least comparable in size to the higher order bulk effects [28]. Bulk SHG measured in reflection will be limited to a region about a wavelength, λ, from the surface, while the surface contribution is assumed to come from the top atomic layer of dimension a. The surface to bulk SHG intensity ratio, which is proportional to the square of the field, will then scale as $\sim(a/\lambda)^2$; for λ in the optical region, this factor is $\sim10^{-6}$. Now, in the bulk of the solid, the standard multipole expansion of fields, gives contributions to the SHG intensity which scale as $(a/\lambda)^2$ with order. Thus, in the optical region, the electric quadrupole and magnetic dipole terms will contribute about $\sim10^{-6}$ of the SHG intensity of the electric dipole term, and the surface dipole effect becomes comparable to the bulk effect in centrosymmetric media where the bulk dipole contribution is forbidden.

The nonlinear polarisation induced by the surface dipole contribution can be written as

$$P_i(2\omega) = \chi^{(2)}_{ijk} E_j(\omega) E_k(\omega) \tag{3.7}$$

where $\chi^{(2)}_{ijk}$ is the second-order nonlinear susceptibility tensor reflecting the structure and symmetry properties of the surface layer. Physical and symmetry considerations allow the number of distinct non-zero elements of $\chi^{(2)}_{ijk}$ to be considerably reduced. As SHG is a special case of SFG, where $E_j E_k = E_k E_j$, the $3\times3\times3$ tensor can be represented by a 6×3 matrix, allowing the expansion of equation (3.7) to be written as

$$\begin{bmatrix} P_x^S \\ P_y^S \\ P_z^S \end{bmatrix} = \varepsilon_0 \begin{bmatrix} \chi_{xxx}^{(2)} & \chi_{xyy}^{(2)} & \chi_{xzz}^{(2)} & \chi_{xyz}^{(2)} & \chi_{xzx}^{(2)} & \chi_{xxy}^{(2)} \\ \chi_{yxx}^{(2)} & \chi_{yyy}^{(2)} & \chi_{yzz}^{(2)} & \chi_{yyz}^{(2)} & \chi_{yzx}^{(2)} & \chi_{yxy}^{(2)} \\ \chi_{zxx}^{(2)} & \chi_{zyy}^{(2)} & \chi_{zzz}^{(2)} & \chi_{zyz}^{(2)} & \chi_{zzx}^{(2)} & \chi_{zxy}^{(2)} \end{bmatrix} \begin{bmatrix} E_x(\omega)E_x(\omega) \\ E_y(\omega)E_y(\omega) \\ E_z(\omega)E_z(\omega) \\ 2E_z(\omega)E_y(\omega) \\ 2E_z(\omega)E_x(\omega) \\ 2E_x(\omega)E_y(\omega) \end{bmatrix} \tag{3.8}$$

A further conjecture due to Kleinman [29] uses a 3D symmetry argument to propose that all three indices *ijk* are permutable in the second order susceptibility when the frequency of excitation ω and its SH 2ω are far from resonance. Departures from Kleinman symmetry where these conditions are satisfied have been discussed recently [30], while the 3D symmetry breaking at the surface or interface prevents the use of Kleinmann symmetry in the phenomenological modelling. Nye [31] has tabulated the relationships between different elements of the piezoelectric tensor, which has the same form as $\chi_{ijk}^{(2)}$, for the various surface point groups. For the 2D point groups, table 3.1 lists the non-zero components.

First attempts at models of the SHG process at surfaces were made by Bloembergen and Pershan [32] who discussed nonlinear optical properties of a slab of vanishing thickness, representing a surface layer. Heinz [33] later applied appropriate boundary conditions to a surface induced dipole sheet, resulting in expressions for the SH power in terms of the surface $\chi^{(2)}$ and the properties of the excitation source. Higher-order nonlocal terms, magnetic dipolar and electric quadrupolar, were considered in the phenomenological analysis of Sipe, Moss and van Driel [34].

The large electric field gradients across the surface layers are expected to result in a significant electric quadrupolar response [35, 36]. This contribution is obviously highly surface specific. An effective theory, then, must combine local and nonlocal responses of the surface layer and bulk. The lowest-order bulk contributions to the SH response of adsorbate on Si systems is of magnetic dipolar and electric quadrupolar symmetry in the dipole approximation. The total effective nonlinear polarisation can be written as [34], regardless of the details of the mechanism as

$$P_i^B(2\omega,\mathrm{r}) = \Gamma_{ijkl} E_j(\omega,\mathrm{r}) \nabla_k E_l(\omega,\mathrm{r}) \tag{3.9}$$

Table 3.1 Independent non-zero elements of χ^{s}_{ijk} for crystallographic and continuous point groups for a surface in the *xy*-plane

Symmetry class	Independent non-zero elements χ^{s}_{ijk} for SHG
1	*xxx, xxy, xyy, yxx, yxy, yyy, xxz, xyz, yxz, yyz, zxx, zxy, zyy, xzz, yzz, zxz, zyz, zzz*
1m	*xxx, xyy, xzz, xzx, yzy, yxy, zxx, zyy, zxz, zzz*
2	*xzx, xyz, yxz, yzy, zxx, zyy, zxy, zxz, zzz*
2mm	xzx, yzy, zxx, zyy, zzz
3	*xxx = -xyy = -yyx, yyy = -yxx = -xyx,* *yzy = xzx, zxx = zyy, xyz = -yxz, zzz,*
3m	*xxx = -xyy = -yxy, xzx = yzy, zxx = zyy, zzz*
4,6,∞	*xxz=yyz, zxx = zyy, xyz = -yxz, zzz*
4mm,6mm,∞ m	*xxz=yyz, zxx = zyy, zzz*

where ∇_k is taken with respect to the field co-ordinates, Γ_{ijkl} is a fourth rank tensor, and the E_i are the components of the exciting field inside the medium. Bloembergen et al. [37] have expressed this equivalently, for cubic centrosymmetric semiconductors, as

$$P_i^B(2\omega,\mathrm{r}) = (\delta-\beta-2\gamma)(\mathrm{E}.\nabla)E_i + \beta E_i(\nabla\mathrm{E}) + \gamma\nabla_i(\mathrm{E}.\mathrm{E}) + \xi E_i\nabla_i E_i \qquad (3.10)$$

where δ,β,γ,ξ are frequency-dependent phenomenological constants derived from Γ_{ijkl}. For excitation of bulk Si by a single transverse wave, the first two terms of equation (3.10) vanish. The third term is isotropic while the fourth is anisotropic. The total bulk contribution of Si reduces to $P_i^B(2\omega) = \gamma\nabla_i(\mathrm{E}.\mathrm{E}) + \xi E_i\nabla_i E_i$ consisting of a constant background and a face dependent signal. Using a generalised Green's function approach, the resultant SH fields have been calculated [38] for a polarisation of the form $p(\mathrm{r}.t) = P\exp(i\kappa.R - 2i\omega t)$ where $R = R(x,y)$ and κ is real. By matching this polarisation to that in equation (3.10), the SH fields due to $P_i^B(2\omega)$ can be found. The fields due to the bulk isotropic source are found to be the same for all crystal faces and are found to be of *p*-polarisation only, while those due to the anisotropic term are face dependent and are of both *s*- and *p*- polarisation.

The symmetry-allowed dipole term of the surface region and the bulk contribution due to the large discontinuity of the normal component of the exciting electric field across the surface, can be amalgamated into an effective nonlinear polarisation [34] $P_i^S(2\omega)=\varepsilon_0\chi_{ijk}^S E_j E_k \delta\left(z-z_0^+\right)$ where z is the outward surface normal, and χ_{ijk}^S is the surface nonlinear susceptibility tensor transforming with the point group of the surface. The delta function $\delta\left(z-z_0^+\right)$ strongly localises the surface contribution.

3.4.2 The two-phase model of Sipe, Moss, van Driel and Mizrahi

A phenomenological treatment of surface SHG has been presented by Sipe *et al.* [34, 39] The form of the SH fields generated in vacuum at the (111), (100) and (110) faces of a centrosymmetric crystal have been deduced. Limiting the discussion to reflection and together with the bulk contributions outlined earlier, the total SH fields from the (111) or (100) face can now be expressed in the following way, where E_{mn} refers to the m-polarised second harmonic response to the n-polarised probe and ψ is the angle between the crystal x axis and the plane of incidence:

$$\begin{aligned}
E_{pp}(2\omega) &= \left(a_1 + c_1 \cos\kappa\psi\right)E_p^2(\omega)A_p \\
E_{ps}(2\omega) &= \left(a_2 + c_2 \cos\kappa\psi\right)E_s^2(\omega)A_p \\
E_{sp}(2\omega) &= \left(b_1 \sin\kappa\psi\right)E_p^2(\omega)A_s \\
E_{ss}(2\omega) &= \left(b_2 \sin\kappa\psi\right)E_s^2(\omega)A_s
\end{aligned} \qquad (3\ .11)$$

The a_i mix bulk and surface isotropic contributions, the b_i and c_i are the bulk and surface anisotropic coefficients and the A_i are Fresnel terms, all tabulated in detail by Sipe et al.[34]. The coefficient κ in the azimuthal dependence of the above equations is related to the symmetry point group of the surface and takes the value 3 for the (111) face. Isolation of the individual components of the surface $\chi^{(2)}$ is difficult since the bulk terms are inextricably tied to the surface terms, and may even be of the same order of magnitude. For clean Si surfaces, the bulk terms are negligible, for the fundamental wavelengths here and equations (3.11) can be simplified , using Sipe *et al.*'s tabulations [34], to

$$\begin{aligned}
E_{pp}(2\omega) &= \left[f_1\chi_{zzz}^{(2)} + f_2\chi_{zxx}^{(2)} + f_3\chi_{xxz}^{(2)} + f_4\chi_{xxx}^{(2)}\cos 3\psi\right]E_p^2(\omega) \\
E_{ps}(2\omega) &= \left[f_5\chi_{zxx}^{(2)} + f_6\chi_{xxx}^{(2)}\cos 3\psi\right]E_s^2(\omega) \\
E_{sp}(2\omega) &= \left[f_7\chi_{xxx}^{(2)}\sin 3\psi\right]E_p^2(\omega) \\
E_{ss}(2\omega) &= \left[f_8\chi_{xxx}^{(2)}\sin 3\psi\right]E_p^2(\omega)
\end{aligned} \qquad (3.12)$$

where f_i are Fresnel factors for off-normal incidence. Equation (3.12) can be utilized to analyze the experimental plots of SH intensity for sample rotation.

However, sample rotation studies are difficult in UHV systems. An alternative approach can be used which involves rotating the input polarisation angle, instead of the sample. Assuming the fundamental wave vector *E* makes an angle α with respect to the plane of incidence, the field components are related to *E* by

$$\begin{vmatrix} E_x \\ E_y \\ E_z \end{vmatrix} = \begin{vmatrix} a\cos\alpha \\ b\sin\alpha \\ c\cos\alpha \end{vmatrix} E \tag{3.13}$$

where *a*, *b* and *c* are Fresnel coefficients, then *p*- and *s*- components of the reflected SH wave can be written as

$$\begin{aligned} E_p^r &= \left(A\cos^2\alpha + B\sin^2\alpha + C\sin 2\alpha\right)E^2 \\ E_s^r &= \left(F\cos^2\alpha + G\sin^2\alpha + H\sin 2\alpha\right)E^2 \end{aligned} \tag{3.14}$$

The terms *A*, *B*, *C*, *F*, *G* and *H* are functions of the second-order susceptibilities and the Fresnel factors [40] and are discussed in detail in chapter 7. Experimental plots of SH intensity versus polarisation angle carried out in this work are analysed in light of these plots.

For vicinal surfaces, small modifications of the Fresnel coefficients and some missing of tensor components occurs, as tabulated by Lupke *et al.*[41]. The substrates used in this work have vicinalities of only a few degrees, and the corrections can be safely neglected.

3.4.3 Simplification at normal incidence

The phenomenological treatment of normal incidence SHG is straightforward when the bulk signal can be ignored. For light incident normal to the surface, the excitation field's polarisation vector is confined to the plane of the surface and there is no refraction. For an *E* field's polarisation vector at an angle α to the x axis, simplified expressions can be immediately extracted from equation (3.14) by substituting the *E* field components.

$$\begin{aligned} P_x(2\omega) &= \varepsilon_o E^2\left[\chi_{xxx}^{(2)}\cos^2\alpha + \chi_{xyy}^{(2)}\sin^2\alpha + \chi_{xyx}^{(2)}\sin 2\alpha\right] \\ P_y(2\omega) &= \varepsilon_o E^2\left[\chi_{yxx}^{(2)}\cos^2\alpha + \chi_{yyy}^{(2)}\sin^2\alpha + \chi_{yyx}^{(2)}\sin 2\alpha\right] \end{aligned} \tag{3.15}$$

The detected intensity with the 2*ω* field along the *i* axis is then given by $I_i(2\omega) \propto |P_i|^2$. Plots of $I_i(2\omega)$ obtained by sweeping the input polarisation vector α, for fixed output polarisation, can then be matched to the above equations to obtain values for those $\chi^{(2)}$ components allowed by symmetry (table 3.1, with all *z*-dependent components set to zero).

References

1. Wassermeier M, Kamiya I, Aspnes DE, Florez LT, Harbison JP, Petroff PM: **Optical spectroscopy of (001) GaAs and AlAs under molecular-beam epitaxy growth conditions.** *Journal of Vacuum Science & Technology B (Microelectronics Processing and Phenomena)* 1991, **9:**2263-2267.
2. Aspnes DE, Harbison JP, Studna AA, Florez LT: **Application of reflectance difference spectroscopy to molecular-beam epitaxy growth of GaAs and AlAs.** *Journal of Vacuum Science & Technology A (Vacuum, Surfaces, and Films)* 1988, **6:**1327-1332.
3. Power JR, Weightman P, Bose S, Shkrebtii AI, Del Sole R: **Sensitivity of reflectance anisotropy spectroscopy to the orientation of Ge dimers on vicinal Si(001).** *Physical Review Letters* 1998, **80:**3133-3136.
4. Power JR, Farrell T, Gerber P, Chandola S, Weightman P, McGilp JF: **The influence of monolayer coverages of Sb on the optical anisotropy of vicinal Si(001).** *Surface Science* 1997, **372:**83-90.
5. Jaloviar SG, Lin J-L, Liu F, Zielasek V, McCaughan L, Lagally MG: **Step-Induced Optical Anisotropy of Vicinal Si(001).** *Physical Review Letters* 1999, **82:**791-794.
6. Baumberger F, Herrmann T, Kara A, Stolbov S, Esser N, Rahman TS, Osterwalder J, Richter W, Greber T: **Optical recognition of atomic steps on surfaces.** *Physical Review Letters* 2003, **90:**177402-177401.
7. Hingerl K, Balderas-Navarro RE, Bonanni A, Tichopadek P, Schmidt WG: **On the origin of resonance features in reflectance difference data of silicon.** *Applied Surface Science* 2001, **175-176:**769-776.
8. Stahrenberg K, Hermann T, Esser N, Richter W: **Surface optical properties of clean Cu(110) and Cu(110)-(2*1)-O.** *Physical Review B* 2000, **61:**3043-3047.
9. Stahrenberg K, Hermann T, Esser N, Sahm J, Richter W, Hoffmann SV, Hofmann P: **Surface-state contribution to the optical anisotropy of Ag(110) surfaces: A reflectance-anisotropy-spectroscopy and photoemission study.** *Physical Review B (Condensed Matter)* 1998, **58:**10207-10209.
10. Hofmann P, Rose KC, Fernandez V, Bradshaw AM, Richter W: **Study of surface states on Cu(110) using optical refiectance anisotropy.** *Physical Review Letters* 1995, **75:**2039.
11. Hansen JK, Bremer J, Hunderi O: **The electronic structure of Cu(110) and Ag(110) surfaces studied by reflection anisotropy spectroscopy.** *Surface Science* 1998, **418:**58-61.
12. Fleischer K, Chandola S, Esser N, Richter W, McGilp JF: **Reflectance anisotropy spectroscopy of Si(111)-(4*1)-In.** *physica status solidi (a)* 2001, **188:**1411-1416.
13. Chandola S, Jacob J, Fleischer K, Vogt P, Richter W, McGilp JF: **Optical response of Ag-induced reconstructions on vicinal Si(111).** *Physica Status Solidi B* 2005, **242:**3017-3021.
14. Chandola S, Jacob J, Fleischer K, Vogt P, Richter W, McGilp JF: **Optical and electronic properties of Ag nanodots on Si(111).** *Journal of Physics: Condensed Matter* 2006, **18:**6979-6986.
15. Fleischer K, Chandola S, Herrmann T, Esser N, Richter W, McGilp JF: **Free-electron response in reflectance anisotropy spectra.** *Physical Review B (Condensed Matter and Materials Physics)* 2006, **74:**195432-195410.

16. Fleischer K, Chandola S, Esser N, Richter W, McGilp JF, Schmidt WG, Wang S, Lu W, Bernholc J: **Atomic indium nanowires on Si(111): the (4*1)-(8*2) phase transition studied with reflectance anisotropy spectroscopy.** *Applied Surface Science* 2004, **234:**302-306.
17. Frederick BG, Power JR, Cole RJ, Perry CC, Chen Q, Haq S, Bertrams T, Richardson NV, Weightman P: **Adsorbate azimuthal orientation from reflectance anisotropy spectroscopy.** *Physical Review Letters* 1998, **80:**4490-4493.
18. Frederick BG, Cole RJ, Power JR, Perry CC, Chen Q, Richardson NV, Weightman P, Verdozzi C, Jennison DR, Schultz PA, Sears MP: **Molecular orientation with visible light: Reflectance-anisotropy spectroscopy of 3-thiophene carboxylate on Cu(110) surfaces.** *Physical Review B (Condensed Matter)* 1998, **58:**10883-10889.
19. Martin DS, Davarpanah AM, Barrett SD, Weightman P: **Reflection anisotropy spectroscopy of the Na/Cu(110)(1*2) surface reconstruction.** *Physical Review B (Condensed Matter)* 2000, **62:**15417-15419.
20. Zettler JT, Rumberg J, Ploska K, Stahrenberg K, Pristovsek M, Richter W, Wassermeier M, Schutzendube P, Behrend J, Daweritz L: **Reflectance anisotropy oscillations during MOCVD and MBE growth of GaAs (001).** *Physica Status Solidi a-Applied Research* 1995, **152:**35-47.
21. Weightman P, Martin DS, Cole RJ, Farrell T: **Reflection anisotropy spectroscopy.** *Reports on Progress in Physics* 2005, **68:**1251-1341.
22. Hecht E: *Optics.* Addison-Wisely Publishing Co.Inc; 1987.
23. Azzam RMA, Bashara NM: *Ellipsometry and polarized light.* North-Holland; 1977.
24. Aspnes DE: **Above-bandgap optical anisotropies in cubic semiconductors: a visible-near ultraviolet probe of surfaces.** *Journal of Vacuum Science & Technology B* 1985, **3:**1498-1506.
25. Berkovits VL, Makarenko IV, Minashvili TA, Safarov VI: **Optical transitions on GaAs [110] surface.** *Solid State Communications* 1985, **56:**449-450.
26. Kempf RW, Wilson PT, Canterbury JD, Mishina ED, Aktsipetrov OA, Downer MC: **Third and fourth harmonic generation at Si-SiO2 interfaces and in Si-SiO2-Cr MOS structures.** *Applied Physics B-Lasers and Optics* 1999, **68:**325-332.
27. McGilp JF: **Epioptics - Linear and Nonlinear Optical Spectroscopy of Surfaces and Interfaces.** *Journal of Physics-Condensed Matter* 1990, **2:**7985-8006.
28. Shen Y, R: *The Principles of Non-linear Optics.* New York, Wiley; 1984.
29. Kleinman DA: *Physical Review* 1962, **126:**1977.
30. McGilp JF: **Using steps at the Si -SiO2 interface to test simple bond models of the optical second-harmonic response.** *Journal of Physics: Condensed Matter* 2007, **19:**016006.
31. Nye JF: *Physical properties of crystals.* Oxford University Press; 1957.
32. Bloembergen N, Pershan PS: **Light Waves at the Boundary of Nonlinear Media.** *Physical Review* 1962, **128:**606.
33. Heinz TF: **Ph.D dissertation.** University of California, 1982.
34. Sipe JE, Moss DJ, van Driel HM: **Phenomenological theory of optical second- and third-harmonic generation from cubic centrosymmetric crystals.** *Physical Review B-Condensed Matter* 1987, **35:**1129-1141.
35. Guyot-Sionnest P, Chen W, Shen YR: **General considerations on optical second-harmonic generation from surfaces and interfaces.** *Physical Review B (Condensed Matter)* 1986, **33:**8254-8263.

36. Guyot-Sionnest P, Shen YR: **Local and nonlocal surface nonlinearities for surface optical second-harmonic generation.** *Physical Review B (Condensed Matter)* 1987, **35:**4420-4426.
37. Bloembergen N, Chang RK, Jha SS, Lee CH: **Optical second-harmonic generation in reflection from media with inversion symmetry.** *Physical Review* 1968, **174:**813-822.
38. Sipe JE: **New Green-function formalism for surface optics.** *Journal of the Optical Society of America B (Optical Physics)* 1987, **4:**481-489.
39. Mizrahi V, Sipe JE: **Phenomenological treatment of surface second-harmonic generation.** *Journal of the Optical Society of America B (Optical Physics)* 1988, **5:**660-667.
40. Power JR, O'Mahony JD, Chandola S, McGilp JF: **Resonant Optical 2nd-Harmonic Generation at the Steps of Vicinal Si(001).** *Physical Review Letters* 1995, **75:**1138-1141.
41. Lüpke G, Bottomley DJ, van Driel HM: **Second- and third-harmonic generation from cubic centrosymmetric crystals with vicinal faces: phenomenological theory and experiment.** *Journal of the Optical Society of America B-Optical Physics* 1994, **11:**33-44.

4

Experimental details

4.1 Overview

This chapter describes sample preparation, including the use of evaporation sources, and elemental and structural characterisation. Detailed descriptions of the RAS and SHG experimental configurations are also provided.

4.2 Sample preparation

4.2.1 Substrate cleaning

All the Si samples in the experiments were prepared from commercially available wafers, cut 1^{o}, 2^{o} and 3^{o} off the [111] axis towards the high symmetry $[\bar{1}\bar{1}2]$, and 4^{o} towards the $[11\bar{2}]$ directions. Si(557) wafers were also used: these are cut 9.5^{o} off the [111] axis towards $[\bar{1}\bar{1}2]$. In order to use stepped surfaces as templates for producing one-dimensional wires or stripes by decorating the step edges, it is essential to start with regular step arrays which exhibit atomically straight step edges and low kink densities as discussed in chapter 2 section 2.2.2. The cleaning of the Si(111) surface plays a major role in obtaining regular step arrays. A number of different methods can be employed for thermal treatment of Si surfaces in UHV. For instance, electrons can be accelerated to the rear of the sample from a hot filament by means of a large bias voltage. This is termed electron bombardment. Another method is resistive heating. Silicon, a semiconductor, has a negative thermal coefficient of resistance. Its electrical conductivity, as for all semiconductors, depends on the fact that, at room temperature, the distribution of thermal energies of electrons, (characterised by Boltzmann distribution of the form, $\exp^{(-E_{gap}/kT)}$, where E_{gap} is the energy band gap of the semiconductor), is such that a significant population of states in the conduction band results. This, together with holes left in the valence band, provides mobile carriers for the current. The effect of heating is to further populate the conduction band with electrons and valence band with holes, resulting in lower resistance at higher temperature. In this work, samples were cleaned by resistive heating. The first stage of resistive heating is to apply a high voltage across the sample to breakdown the native oxide layer, to create enough carriers for current to begin flowing. This method does have the advantage of being able to uniformly heat Si samples routinely right up to the melting point, provided feedthroughs can handle the current. This requires proper clamping of the Si samples in their sample holders to ensure even heating. In this work, sample ends were wrapped in a tantalum foil and clamped securely with stainless steel clamps as illustrated in figure 4.1. Extensive repetition of resistive heating can lead to the electromigration of steps [1], but no evidence of this has been found for the limited heating of samples reported in this work.

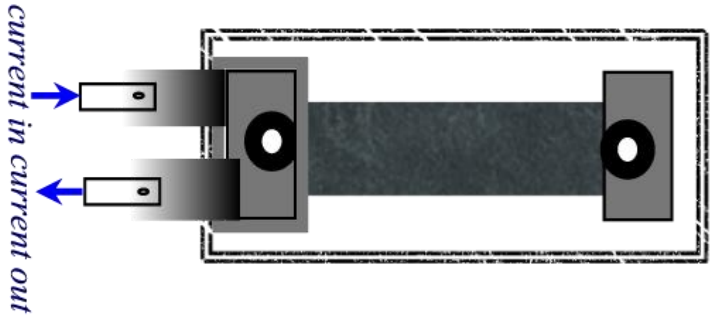

Figure 4.1 Top view of sample holder used for UHV experiments

Silicon temperature control was achieved using an optical pyrometer. The emissivity of Si through the optical port of the UHV chamber in use is required for accurate readings by pyrometer. For standard UHV conditions, the emissivity of Si is ~0.66. The procedure used to obtain regular array of ordered single height steps (single height steps on the Si(111) surface are defined as the spacing between first and second Si bilayers, a distance of 0.3135 nm) is detailed in O'Mahony et al [2] . Degassing of samples and sample holders was achieved by annealing to 800°C for a number of hours in UHV until good chamber pressures were recovered. Removal of the oxide layer occurred on flashing samples to 1200°C. The sample was then rapidly cooled to inhibit step bunching. The whole heating cycle was then repeated and Auger electron spectra (figure 4.2(a)) showed negligible contamination. A low energy electron diffraction (LEED) pattern of the 7×7 reconstruction obtained following this surface treatment is shown in figure 4.2(b).

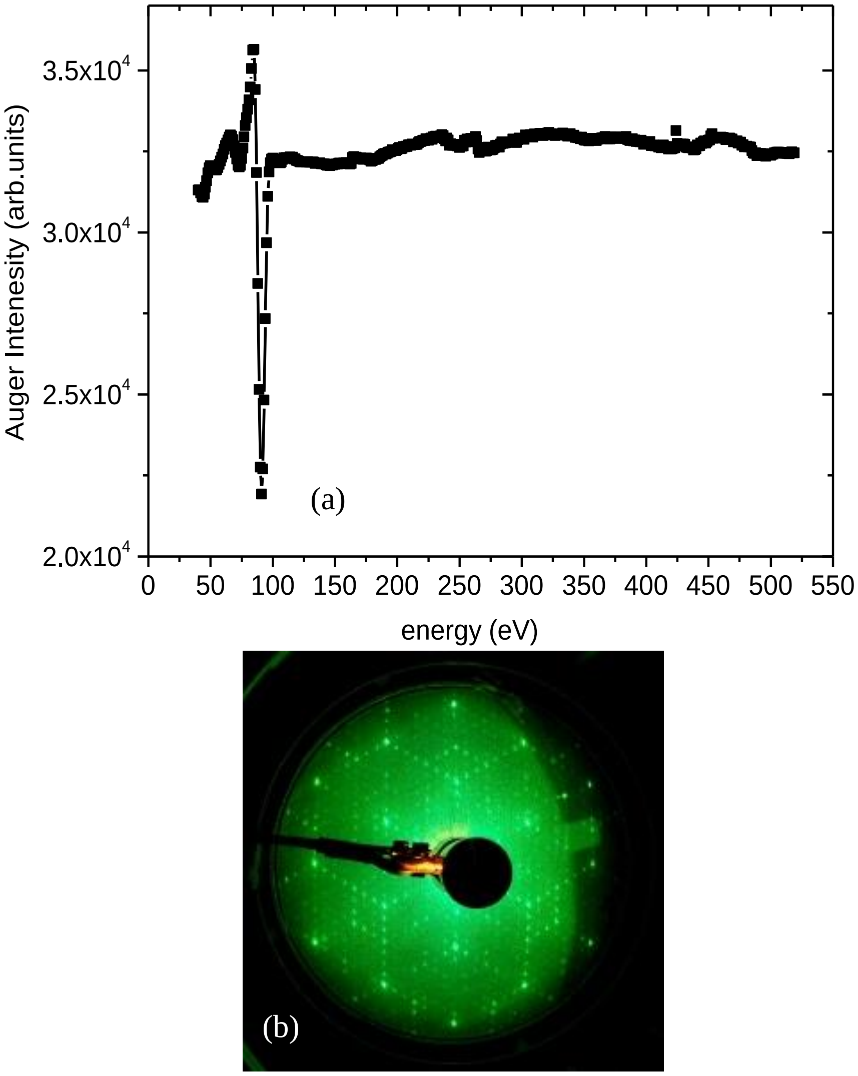

Figure 4.2 (a) Auger electron spectrum of clean silicon. (b) LEED pattern of Si(111)-7×7.

LEED spot splitting due to the regular array of steps is not generally seen on the low angle offcuts, due to the coherence length of the LEED gun. Scanning tunneling microscopy (STM) was used by Dr. Sandhya Chandola, at the Technische Universität Berlin, to check that the thermal processing recipe used led to regular, well-ordered step structure (see chapter 6).

Auger-electron spectroscopy (AES), LEED and RHEED are standard surface science techniques for determining the elemental composition and crystallographic structure of surfaces. An electron beam of energy 150 eV has a wavelength of around 0.1 nm, making it suitable for electron diffraction experiments. However, this energy is roughly at the minimum in the universal path length curve (figure 4.3(a)), giving these electrons optimum surface sensitivity. The elastic backscattering of low energy electrons incident normally on a crystal surface forms the basis of the technique of LEED. An alternative is to use high energy electrons incident at a grazing angle on the crystal surface. In this case the penetration depth of the electron beam into the surface is also very small, as the component of the incident electron momentum normal to the surface is very small. This forms the basis of RHEED. A standard four-grid Omicron nanotechnology combined rear view-LEED/AES apparatus was used. The system comprises of a normal incidence electron gun and a retarding field analyser (RFA). Electron gun filament currents of approximately 6A gave emission currents of 0.2mA. Diffraction patterns were viewed on a screen at +4kV relative to the grounded sample. AES studies were carried out by applying a modulating voltage (10V peak-peak) to the middle grids of the RFA detecting total secondary electrons, and using a lock-in amplifier. Energy resolution (in eV) of Auger peaks was approximately that of the modulating voltage used. A standard RHEED apparatus (Eiko engineering systems Ltd., Japan) was used with a beam energy of 15keV. The contrasting sampling depths of electron spectrocopies and epioptic techniques are shown in figure 4.3, where it can be seen that optical sampling depths around the visible region are typically ~10 nm, sufficient to penetrate ultra-thin capping layers.

4.2.2 In, Au and Ag evaporation source

A WCK-2 Knudsen cell from WA technology was used for evaporating In on to the substrates. A collimated flux for controlled and reproducible deposition is produced from a crucible made of very fine graphite, the inside of which is coated with pyrolytic boron nitride (PBN), which shows minimal interaction with the deposition material. The crucible is heated using a tantalum foil element, which is insulated with a PBN thermal shield. The Knudsen cell can operate up to temperatures of ~1000°C with a low background pressure of $\sim 5\times10^{-10}$ mbar. Accurate temperature control was by means of a proportional-integrated-differentiated (PID) controller, which has a thermocouple mounted in good

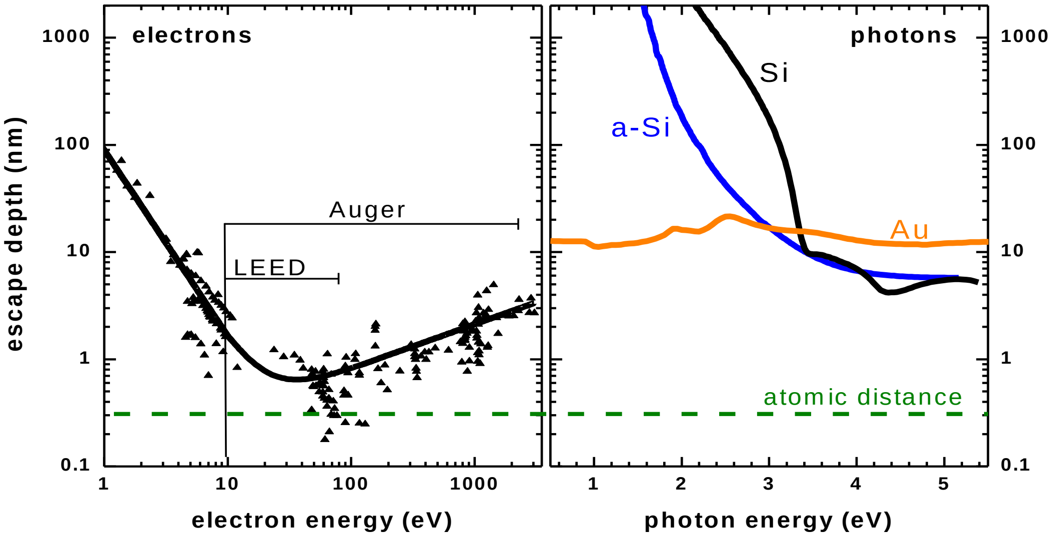

Figure 4.3 Sampling depths of electron spectroscopies and optical techniques

thermal contact with the crucible and is stable to within ±2°C. A High Temperature Effusion cell (HTEZ-40) from MBE-Komponenten designed for clean UHV operation up to 1900°C was used for the evaporation of Ag and Au. Figure 4.4(a) shows the schematic drawing of the main parts of the HTEZ heating system. Due to the high operation temperature the filament is made of tungsten and direct contact between filament insulation parts is avoided. Additional insulating PBN ceramic plates are shielded by tantalum plates to prevent out gassing during operation. The HTEZ provided very reproducible evaporation and precise regulation. The crucible material used for the evaporation was Al_2O_3. Calibration of In, Au, Ag were done using Auger electron spectroscopy and LEED. A quartz crystal oscillator was used instead of AES to calibrate the Ag cell. It was often found that RAS spectral signatures could be used routinely to follow the sample coverage, after initial calibration using AES and LEED. Details of calibration are given in sample preparation section of chapter 5.

4.2.3 Si evaporation source

Silicon capping studies of the Si(111)/In system used a home made evaporator. This was achieved by resistive heating of a piece of silicon near to its melting point. Although a reasonable deposition rate could be achieved, an overall heating of the chamber walls due to the lack of proper shielding and water cooling lead to an increase in base pressure of the system. Later, a Silicon Sublimation Source (SUSI) from MBE-Komponenten was purchased and this was used for the evaporation of silicon for capping studies on Si(111)/Ag. The SUSI allowed growth of high quality ultra-thin Si layers, not otherwise

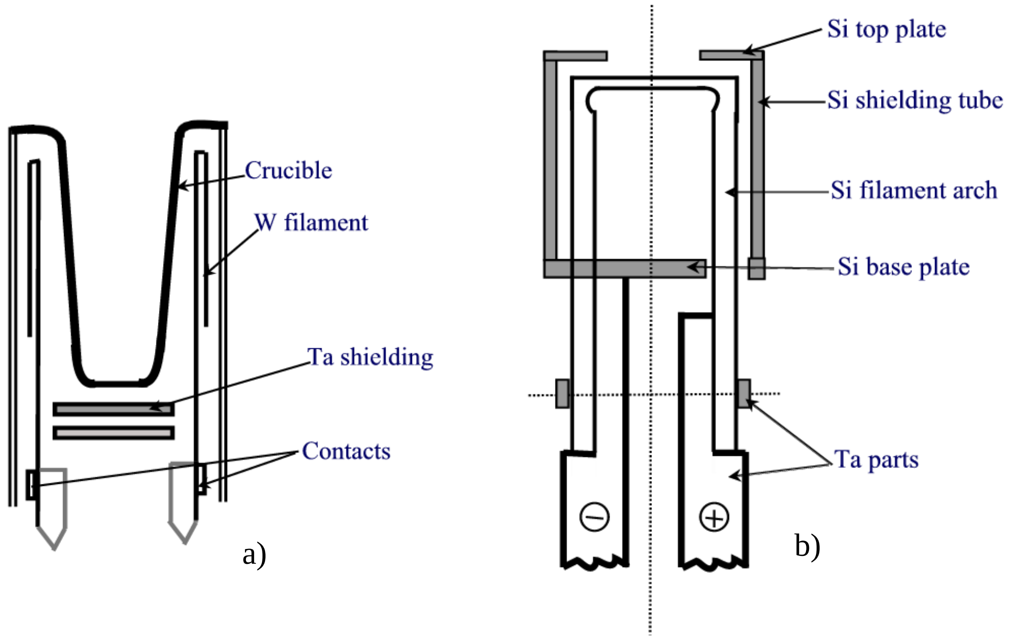

Figure 4.4 Schematic view of a) high temperature effusion cell b) silicon sublimation source.

using effusion cells. It provided a very clean and constant Si flux, although at a low growth rate. The SUSI is commonly used for Si-doping of GaAs epilayers in MBE growth facilities. Figure 4.4(b) shows the schematic diagram of SUSI source. The specially designed free standing silicon filament arch is directly heated by electrical current and is surrounded by high purity silicon shielding parts. Heating of metal and ceramic parts is minimised by very effective water cooling of the electrical contacts. No insulating ceramic parts are used in the hot zone.

4.3 Reflectance anisotropy spectrometer

4.3.1 RAS Experimental configuration

Typical RAS experimental configurations have been described in detail in a recent review [3]. RAS measurements were performed using a system initially constructed by Dr. Fran Pedreschi and Dr. Des O'Mahony of the Dublin Institute of Technology. The performance of this system was improved by Dr. Karsten Fleischer by adding active computer control of the photoelastic modulator (PEM) voltage and replacing the photomultiplier tube (PMT) with a Si/InGaAs dual photodiode. The set-up is based on the configuration designed by Aspnes *et al* [4]. Figure 4.5 shows the schematic diagram of the optical components upon

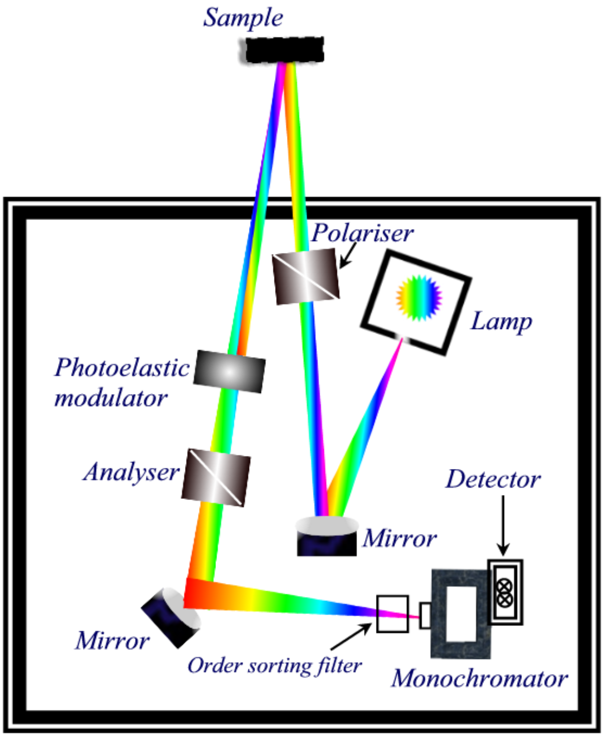

Figure 4.5 Schematic diagram of the RAS optics

the baseplate. Light from the xenon lamp is reflected off the first mirror. The lamp-to-mirror distance is approximately the focal length of the mirror so that the diverging beam is made nearly parallel. The light then passes through a polariser which specifies the axes with regard to which the RA response is being measured. The beam then passes through an optically flat, strain free, fused silica window (FSW) (Bomco USA) into the UHV chamber and strikes the sample. This window consists of an optically flat face which extends out of the vacuum chamber on a glass cylindrical wall. The construction allows the walls to dissipate the strain brought about by mounting the window in the vacuum chamber, leaving the optically flat window largely unaffected. The reflected beam then passes through the PEM and an analyser. The slowly diverging beam is reflected off the second mirror towards the monochromator. The distance from the second mirror to the monochromator is also approximately the focal length of the mirror, and the beam is nearly in focus at the entrance slit. The detector used for RAS measurements of In induced reconstructions was a PMT. Due to the limitation of spectral range to 1.5 eV, any free carrier anisotropy of the RAS signal which will be mainly in the IR region could not be observed. The detector was replaced by a Si photodiode for measurements from 1.3 eV to 5 eV, and an InGaAs detector for 0.85 eV to 1.5 eV. All RA measurements of Ag and Au on Si were performed using this detector. Brief specifications for individual components of the RAS system are

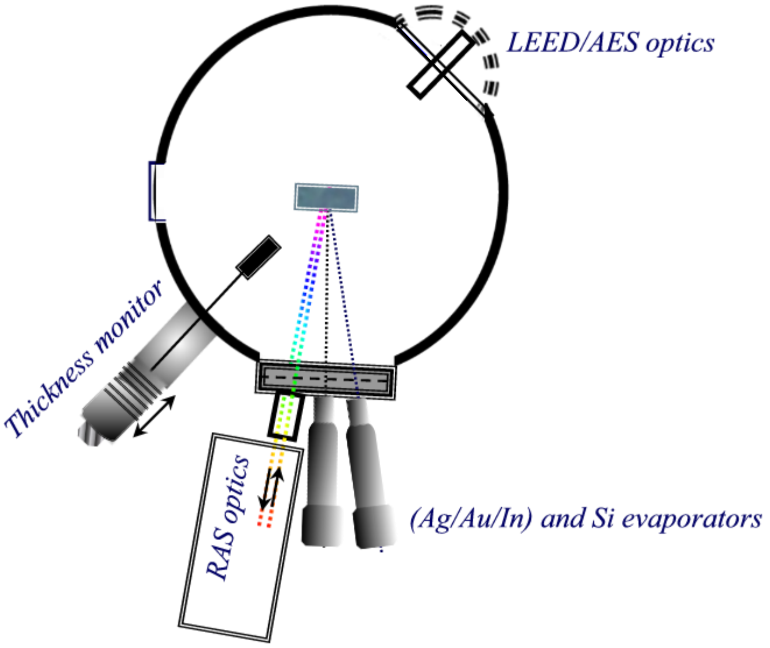

Figure 4.6 RAS set-up with respect to the sample in the UHV chamber

given in Appendix A. Figure 4.6 shows the configuration of RAS set-up and evaporators with respect to the UHV chamber. The configuration allowed real time monitoring of adsorbates on the Si sample with RAS.

The influence of each component on the polarisation state of the light must be considered in determining the output equation for the system. The Jones Vector approach is ideally suited to this task. It represents polarised light as a vector, and optical components as 2×2 matrices. Subsequent interactions of the light with the optical components are calculated by multiplying the element matrices and applying the result to the vector. Hence by applying Jones matrix formalism, the proportionality factors between the time-varying current in the photodetector and reflectance anisotropy can be obtained [3].

$$\begin{aligned}\frac{\Delta I}{I} &= 2\left[-\operatorname{Im}\left(\frac{\Delta r}{r}\right)+\delta_1\cos 2\gamma_1+\delta_2\cos 2\gamma_2-2a_F\right]J_1(\delta_{PEM})\sin\omega t\\ &+2\left[\operatorname{Re}\left(\frac{\Delta r}{r}\right)+2\Delta P+2\Delta M\right]J_2(\delta_{PEM})\cos 2\omega t+\ldots\ldots \end{aligned} \tag{4.1}$$

I	Photodetector current
ΔI	change in photodetector current
γ_1	azimuthal offset of window strain for incident beam

γ_2	azimuthal offset of window strain for reflected beam.
δ_1	incident beam window strain retardation
δ_2	reflected beam window strain retardation
a_F	Polarizer imperfection
δ_{PEM}	PEM retardation
ΔP	misalignment of polarizer
ΔM	misalignment of PEM
J_1, J_2	Bessel functions
ω	PEM modulation angular frequency

and Δr and r are as defined in chapter 3. The terms in this equation reveal many important points about the effective operation of an RA spectrometer. Only first order terms are included, as the others are assumed to be negligible on a properly set up system. It also shows on which part of the RAS response (real or imaginary) that the effects are strongest. For example, ΔP and ΔM has a substantial effect on the real part, but not on the imaginary part (again, to first order). Possibly the most important aspect of the equation is that the anisotropy is modulated at the PEM frequency, and its real and imaginary parts have different frequency dependencies (2ω and ω respectively). This makes them easily distinguishable by lock-in detection, via the f and $2f$ modes.

4.3.2 RA signal processing

Figure 4.7 shows the layout of the electronics. The detector is connected to a unit which contains a preamplifier to amplify the output voltage from the diodes. This unit also contains an active filter box which splits the signal into its AC and DC components. The DC component is measured by the analogue-to-digital converter of the lock-in-amplifier and the AC component goes to the main input of the amplifier. The PEM control voltage is varied remotely via the digital-to-analogue converter of the lock-in-amplifier. The modulating frequency of the PEM provides the external reference signal for the lock-in-amplifier. The PEM, monochromator and lock-in-amplifier (and therefore the whole measurement of $\Delta r / r$ are controlled by a PC. The RMS output from the lock-in-amplifier is converted into peak amplitude.

This output must still undergo minor processing to obtain $\Delta r / r$. This processing can be formulated by considering equation (4.1). This reveals that, in order to get an accurate, maximised output, as well as minimising the misalignments, the relevant Bessel function,

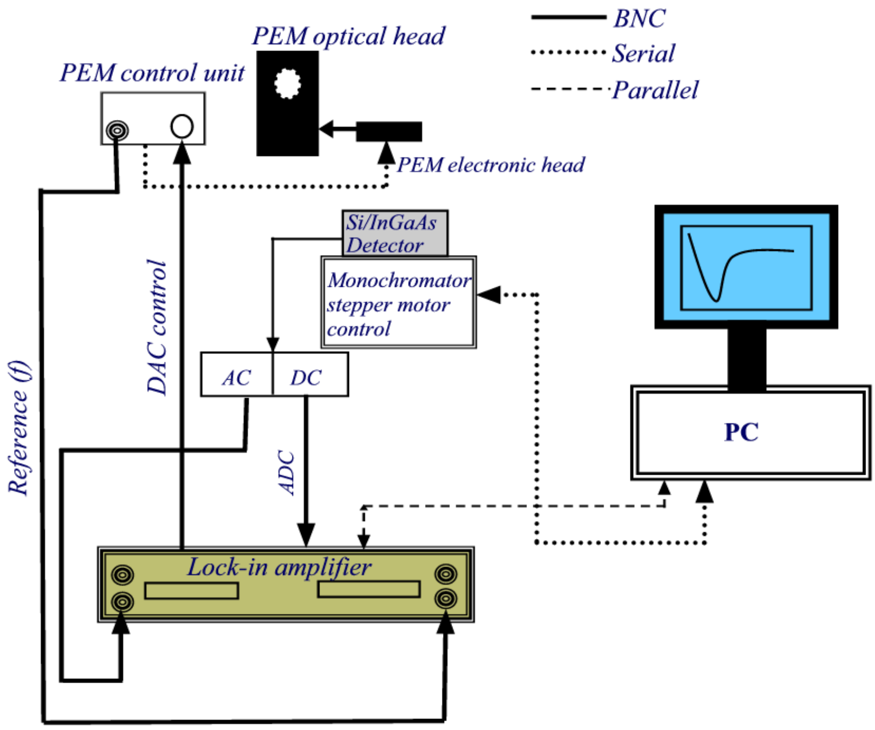

Figure 4.7 Layout of RAS electronics

J_1 or J_2 should be at its peak value. As the value of the Bessel function depends on the PEM retardation, plots of J_1 and J_2 will yield the appropriate values of δ_{PEM} for the imaginary and real response respectively. The DC component is proportional to the intensity I and the AC component of thr real part to the modulation $\Delta I_{2\omega}$.

So, in the absence of any alignment errors and window strain, the 2ω component can be related to the RA response using the following expression derived from equation (4.1)

$$\mathrm{Re}\left(\frac{\Delta r}{r}\right)=\frac{1}{2J_2(\delta_{PEM})}\frac{\Delta I_{2\omega}}{I} \tag{4.2}$$

4.4 Second Harmonic Generation

4.4.1 SHG experimental configuration

The general SHG setup involves impinging a pulsed fundamental beam at an incident angle of 67.5° on the sample and then separating and collecting the SH beam generated which in this work is collinear with the specularly reflected fundamental. A MIRA 900-F fs-laser was used as the fundamental-frequency light source. Pumped with a solid-state

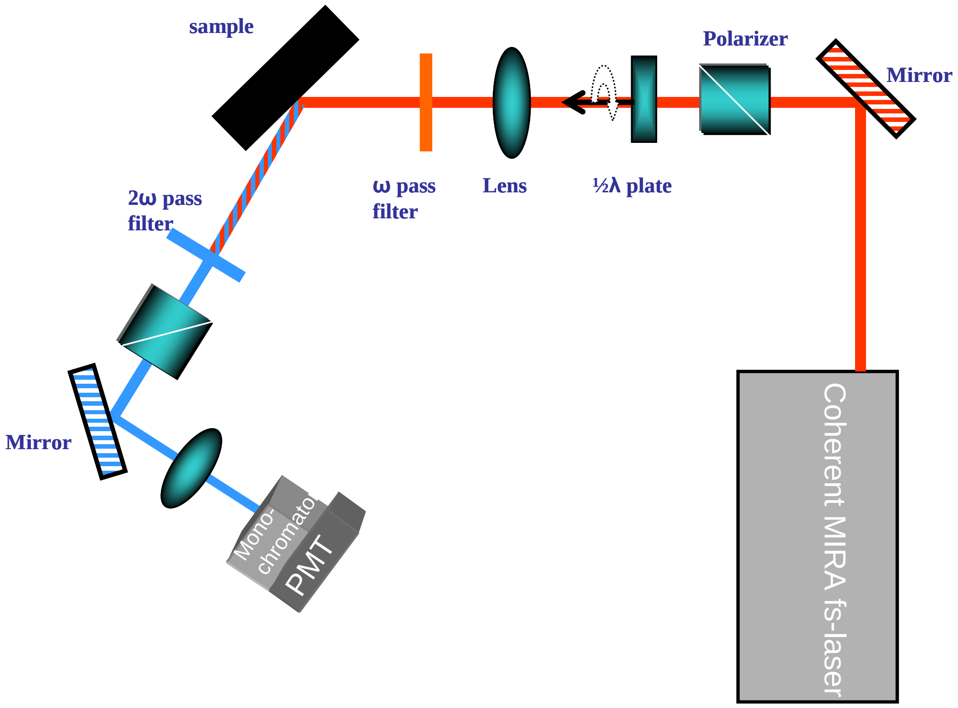

Figure 4.9 Optical set-up for SHG measurements

VERDI V-10 laser, the MIRA generates 130fs pulses of laser light at a 76MHz repetition rate reaching peak powers of approximately 10W necessary for SHG. However, the maximum average power is 0.9W, which does not damage the sample and, indeed, produces negligible heating. The central output-wavelength of the MIRA is continuously tuneable between 710 nm and 980 nm (1.25 eV to 1.75 eV) with a FWHM of about 12 nm caused by the time-bandwidth product of ultra-short pulses. Figure 4.9 shows the optical set up. All elements were attached to an aluminium plate which was bolted to the UHV chamber. The polarised pulsed laser beam of frequency ω is first steered using mirrors. The beam then progresses to a Glan-Air polariser with an extinction coefficient of 10^{-5} and set for maximum transmission. A motorised half wave plate acts as a polarisation rotator which allows the plane of polarisation of the beam to be set or continually changed under PC control. These are 2θ devices, meaning their rotation through θ results in a polarisation rotation of 2θ. The beam then passes through a lens and an OG550 filter. The filter eliminates any 2ω generated in the input optics. The lens allowed the beam to be focussed to a 190 μm FWHM-diameter on the sample. After reflection from the sample, the beam passes through a BG39 filter, which removes most of the fundamental, allowing the 2ω to be passed through a second Glan-air polariser. The orientation of this polariser determined the output polarization alignment of the experiment. The beam then impinges on a dichroic mirror that transmits the residual fundamental frequency component, while reflecting SH frequency component. The beam is then focussed using a lens onto the entrance slit of the monochromator. The 2ω photons are detected by a side-on photon-counting PMT (Hammamatsu R1527P). The initial alignment was carried out using a HeNe beam (2mW CW at 632.8 nm). The advantages of using this laser are its visibility and its safety during alignment. A computer-controlled photon-counter (SR400) was used to discriminate and count the pulses from the PMT. The fs laser controller provided an output channel indicating the intensity of the fundamental beam, allowing real-time normalization of the PMT SHG signal against the input intensity. Figure 4.10 shows the SHG set-up configuration with respect to sample in the UHV chamber, where both SHG and RAS can be measured.

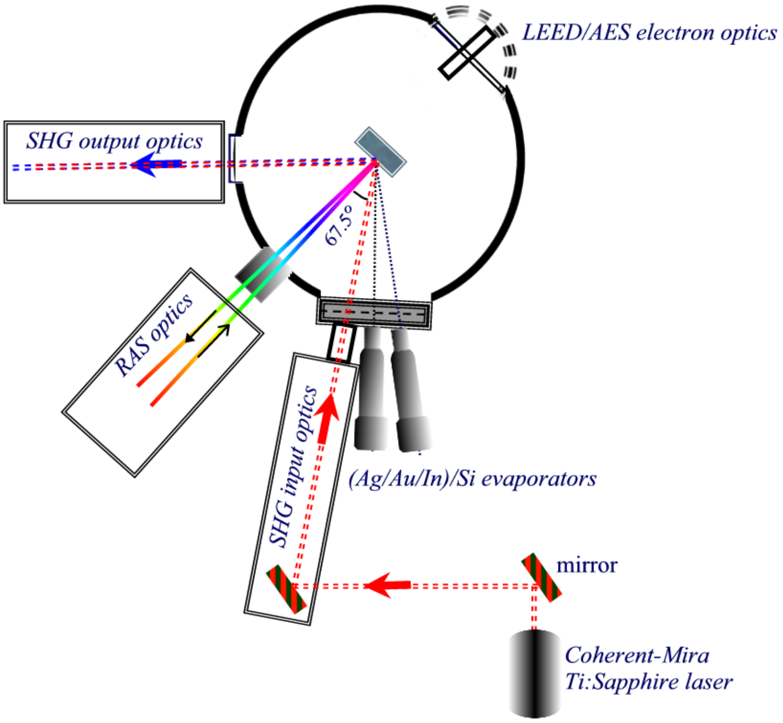

Figure 4.10 SHG set-up with respect to sample in the UHV chamber, allowing both the SHG and RAS to be measured

4.4.2 Minimisation of errors

Since the intensity of the SH signal is related to the fourth power of the amplitude of the excitation field, variations of the excitation field, such as changes in intensity or polarisation mixing, must be eliminated. Any intensity variation is taken care of by using the normalisation method, while MIRA proved to be very stable. The use of specially constructed fused silica windows minimises any strain-induced birefringence.

Misalignment is a potentially significant source of error, particularly arising from polarisation mixing of the *s*- and *p*-SH signal at the output polariser. The precise orientation is crucial in order to avoid any leakage of the *p*-SH signal into the *s*-polarised output, which is typically at least an order of magnitude smaller. The orientation was determined using a cross polarised set-up with respect to the input laser beam.

The net error due to any remaining misalignments and polarisation mixing can be determined by measuring the SH response from a sample where the plane of incidence can be aligned with a mirror plane of the surface. The polarisation rotation plot from a clean, vicinal Si(111)-7×7 surface, offcut by 1^o, is shown in figure 4.11. Plots of SH intensity as a function of input polarisation should produce an even-lobed $\sin^2(2\alpha)$ response with well defined nulls (see chapter 7). Figure 4.11 shows the result, together with the phenomenological curve fit. The clean and sharp nulls, plus the even lobes at 90^o intervals, show that any residual misalignment or polarisation mixing in the apparatus can be considered as negligible.

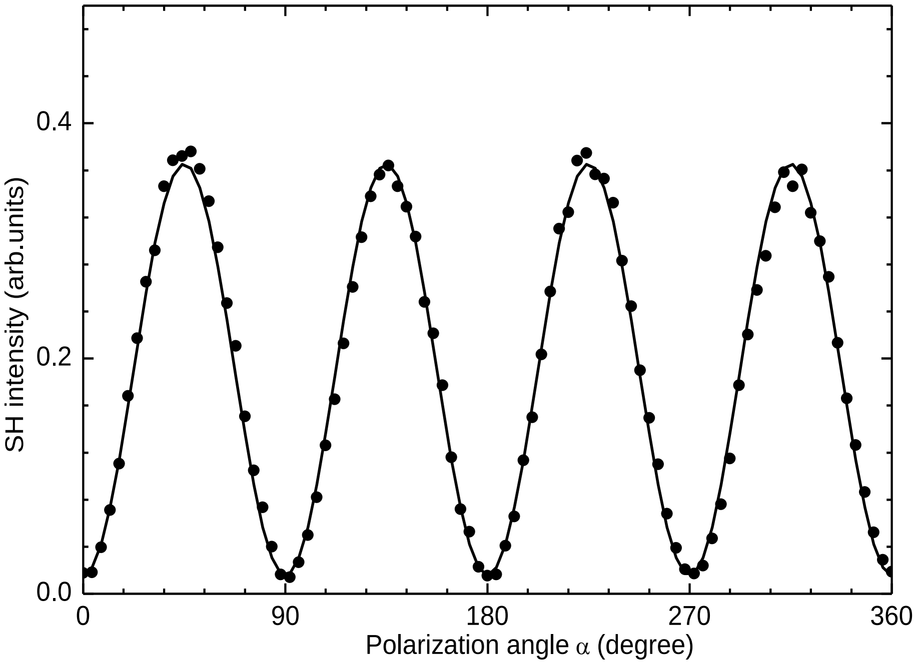

Figure 4.11 α-*sx* (*s*-polarized SH output, *x*-azimuth) rotation plots as a function of angle of polarisation of the fundamental beam, incident at an angle 67.5^o . The substrate was Si(111)-7×7. Experimental points are indicated by dots, and the theoretical fit by solid line.

The nulls are slightly displaced from zero by the dark count of the PMT, while the small difference between the 45^o and 225^o maxima, and the 135^o and 315^o maxima, are systematic and appear to be associated with a slight error in the halfwave plate manufacture.

References

1. Latyshev AV, Aseev AL, Krasilnikov AB, Stenin SI: **Transformations on clean Si(111) stepped surface during sublimation.** *Surface Science* 1989, **213:**157-169.
2. O'Mahony JD, McGilp JF, Leibsle FM, Weightman P, Flipse CFJ: **Control of Terrace Width and Atomic Step Distribution on Vicinal Si(111) Surfaces by Thermal-Processing.** *Semiconductor Science and Technology* 1993, **8:**495-501.
3. Weightman P, Martin DS, Cole RJ, Farrell T: **Reflection anisotropy spectroscopy.** *Reports on Progress in Physics* 2005, **68:**1251-1341.
4. Aspnes DE, Studna AA: **Anisotropies in the above-band-gap optical spectra of cubic semiconductors.** *Physical Review Letters* 1985, **54:**1956-1959.

5

RAS of anisotropic structures grown on vicinal Si(111)

5.1 Overview

The atomic structures of Si(111)-4×1-In, Si(111)-3×1-Ag and Si(111)-5×2-Au, are reviewed. All these structures possess in plane anisotropy. Details of the preparation of various nanostructures and the RAS spectra obtained on different offcut Si(111) samples are presented and discussed.

5.2 Si(111)-4×1-In

Indium on silicon represents an interesting overlayer system which allows us to study the interfacial bonding between a simple metal and an elemental semiconductor in a variety of different interfaces. Indium is known to induce a number of ordered surface phases on Si(111)-7×7 up to coverages of 1-2 ML. The sequence of structures for Si(111)-7×7 as a function of In coverage is [1]:

$$(7\times7)\rightarrow(1\times1)\rightarrow\left(\sqrt{3}\times\sqrt{3}\right)R30^{o}\rightarrow\left(\sqrt{31}\times\sqrt{31}\right)\rightarrow(4\times1)\rightarrow(1\times1)R30^{o}.$$

The $\left(\sqrt{3}\times\sqrt{3}\right)R30^{\circ}$ surface has been studied experimentally by k-resolved direct and inverse UV photoelectron spectroscopy (ARUPS and IPES) [2-4], STM [5], and electron energy loss spectroscopy (EELS) [6]. The pseudomorphic $(1\times 1)R30^{\circ}$ layer, which is observed for coverage greater than 1 ML marks the transition layer growth to 3D islanding, and as well the onset of metallicity in In overlayers [1]. Si(111)-4×1-In is a member of a class of quasi-1D systems that possess chain-like overlayer structures on Si(111) that includes Si(111)-5×2-Au [7] and Si(111)-3×1-X where X ={Li, Na, K, Cs, Ag} [8, 9]. The (4×1)-In forms at coverage between 0.6 - 1 ML at elevated temperature and is presumably the basic interfacial layer for the subsequent Stranski-Krastanov growth. Figure 5.1 shows the model generally accepted for (4×1)-In, based on surface x-ray diffraction analysis [10].

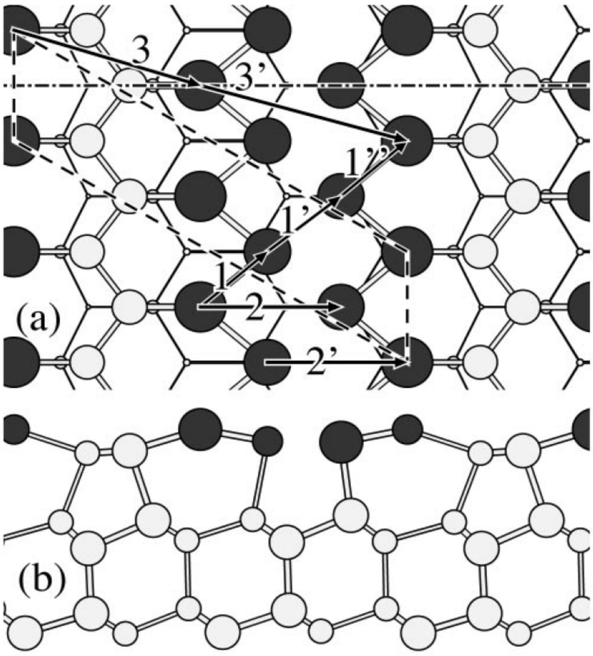

Figure 5.1 Ball-and-stick model of the Si(111)-4×1-In reconstruction in top (a) and side (b) views. Indium atoms are drawn dark grey, silicon atoms are drawn light grey. The standard LEED (4×1) unit cell is indicated by a dashed line. The dash-dotted line along $[11\bar{2}]$ indicates a mirror line [10].

Indium atoms arrange in four lines along the $[1\bar{1}0]$ direction between which zigzag Si chains run. These atomic chains are seen as stripes in the STM image figure taken at RT [11]. Each stripe corresponds to the four In chains, aligned with a spacing corresponding to the four-times super-periodicity. Along each stripe, corrugations corresponding to the fundamental periodicity can be seen. According to the ARUPS study by Abukawa *et al.* [12], it is metallic along the In chains, while insulating in the perpendicular direction.

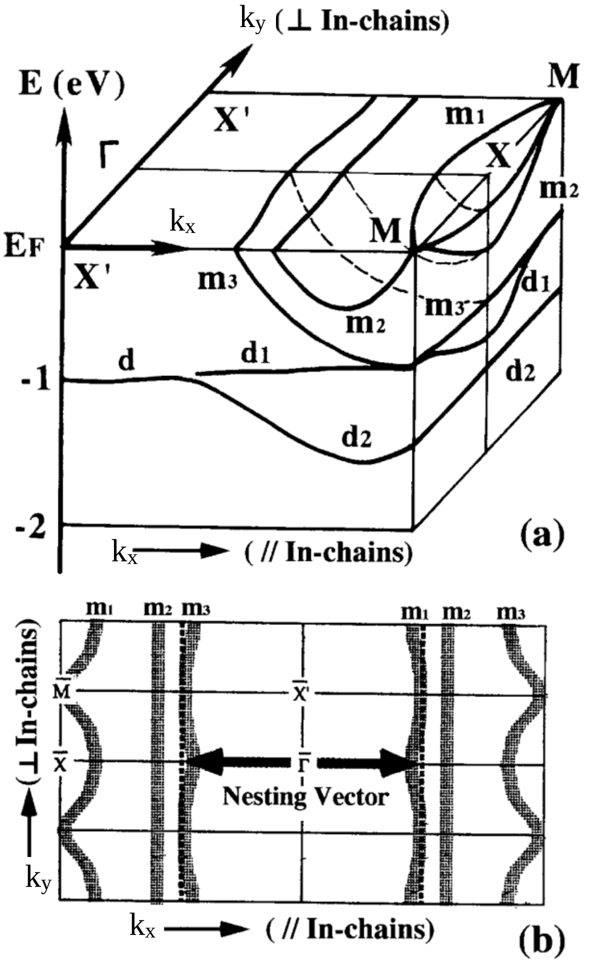

Figure 5.2 Surface-state bands of the Si(111)-4×1-In structure, determined by ARUPS at RT (k_x and k_y are the components of wavevector along the In chains and perpendicular to them, respectively). (a) The band dispersion is drawn three dimensionally. (b) The Fermi surface in the surface Brillouin zone [11].

Along the In chains, three dispersive bands, m_1, m_2, m_3 are found, all of which cross E_F, indicating metallic bands. On the other hand, perpendicular to the In chains, these bands show no significant dispersion. Figure 5.2(a) shows the band dispersion diagram. This indicates that the electrons in these bands are mobile along the stripes, while it hard to make them hop to the neighbouring stripes, i.e, this is a quasi-1D metal. This nature is also consistent with IPES studies of the unoccupied states [13].

Another interesting feature in figure 5.2(a) is, that the m_3 band crosses E_F at around the middle of the surface Brillouin zone and its Fermi surface (line) is roughly parallel to k_y as shown in the figure 5.2(b). This means that a nesting vector of $2k_F$ exists along the In chains, where k_F is the Fermi wavevector. Therefore, the formation of charge-density waves with double periodicity, due to the Peierls instability of one-dimensional metals might be expected at a sufficiently low temperature. The instability of the (4×1) phase is indeed observed when the surface is cooled to a temperature below ~100K [14]. The RHEED/LEED pattern shows streaks indicating a doubled periodicity along the chains. These streaks indicate that there is a lattice distortion of $2a_o$ (a_o = 0.384 nm) periodicity along the linear chains, which is poorly correlated between the chains. The low-temperature phase has been labelled the (4×”2”)-In phase though its actual periodicity turned out to be (8×2) from electron diffraction experiments [15]. Streaky half-order reflections are due to weak inter-chain correlation along the chains. Comparison of ARUPS spectra measured along the linear chains at RT and ~100K show that the metallic states lose their spectral weight at $E_{F,}$ showing a semiconducting nature. This means that a metal to non-metal transition occurs on cooling. This phase transition is related to the formation of a charge density wave (CDW) and the opening of a Peierls half-band gap. However, it has been argued, using surface X-ray diffraction results, that the CDW is not the driving force for the phase transition as the formation of (8×2) is not complete at even 20K [15]. It is suggested that a glide line occurs causing a doubling of the unit cell in the direction perpendicular to the In chains and the periodicity along the In chains doubles due to the outer indium atoms forming In trimers.

5.2.1 Sample preparation

RAS of (4×1)-In has been studied extensively [16-21]. Hence the main aim of the present work is to use it as a model system to understand the preparation of the single domain structures and its characterisation using the RAS system. A vicinal Si(111) substrate, n-type of resistivity 0.1-20 Ω cm, polished 2^o off the [111] toward $[\bar{1}\bar{1}2]$ was used. The sample cleaning procedure was described in section 4.2. Using the Knudsen cell evaporator, with a crucible temperature of 850^oC, between 0.75-1 ML of In was deposited on the clean surface at a substrate temperature of approximately 400^oC to form the single domain (4×1)-In. The structure was confirmed using RHEED or LEED depending on the UHV system used and the surface composition using AES. Figure 5.3(a) shows the single domain (4×1)-In LEED. Figure 5.3(b) shows the calibration of In deposition using AES with the substrate at room temperature. The ratio of the decaying Si LVV Auger transition at 92 eV to the rising In MNN at 400 eV, both normalized to the primary electron current, is used as an estimate of In coverage. (1 ML In = 7.8×10^{14}atoms/cm^2 on the Si(111) surface). Indium was evaporated onto a clean Si(111) substrate held at room temperature and the peak-peak height of Si and In signals measured as a function of time.

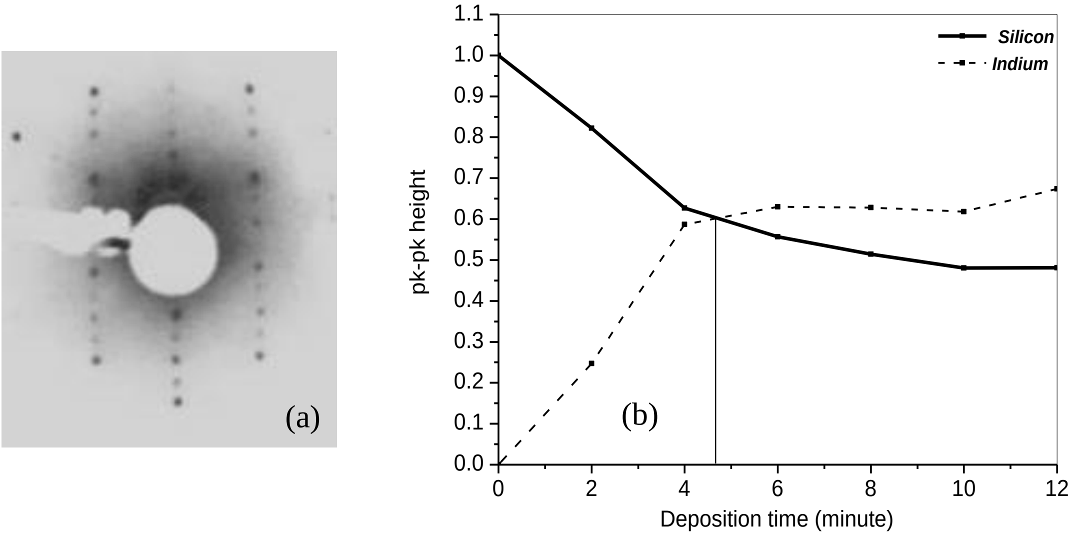

Figure 5.3 (a) Si(111)-4×1-In LEED (b) AES calibration of In coverage. In was deposited at a fixed rate with substrate at room temperature.

The linear relationship up to monolayer coverage demonstrates the absence of metal clustering at low coverages and the uniform growth of first monolayer at RT. The crossover of Si and In AES signals gives a reasonable estimate of 1 ML coverage.

5.2.2 RAS results

The RA spectrometer used follows the design of Aspnes *et al.* [22], details of which are given in section 4.3, using a PMT as the detector. Figure 5.4 shows the transient at 1.9 eV during deposition, with the substrate at 400°C. The formation of (4×1) structure is marked by the appearance of the non-zero RAS signal at around 200 seconds. As ($\sqrt{3}\times\sqrt{3}$)-In is optically isotropic, no RAS is signal is observed before the on-set of the formation of (4×1) structure. Figure 5.5 shows the RAS spectrum after cooling the sample to room temperature. The spectrum agrees well with the previous work [16-21] .The spectrum is dominated by a feature centered at 1.9 eV, and two bulk related features at 3.4 eV and 4.2 eV, corresponding to optical transition across the direct silicon band gap from step modified bulk states. As the energy region is far below the direct optical gap of Si, the 1.9 eV must involve surface states. The negative sign of the (4×1)-In peak is a feature found in the RAS of all chain-like metal-induced structures on vicinal Si(111) studied so far. RAS of other structures are reported in the following sections of this chapter.

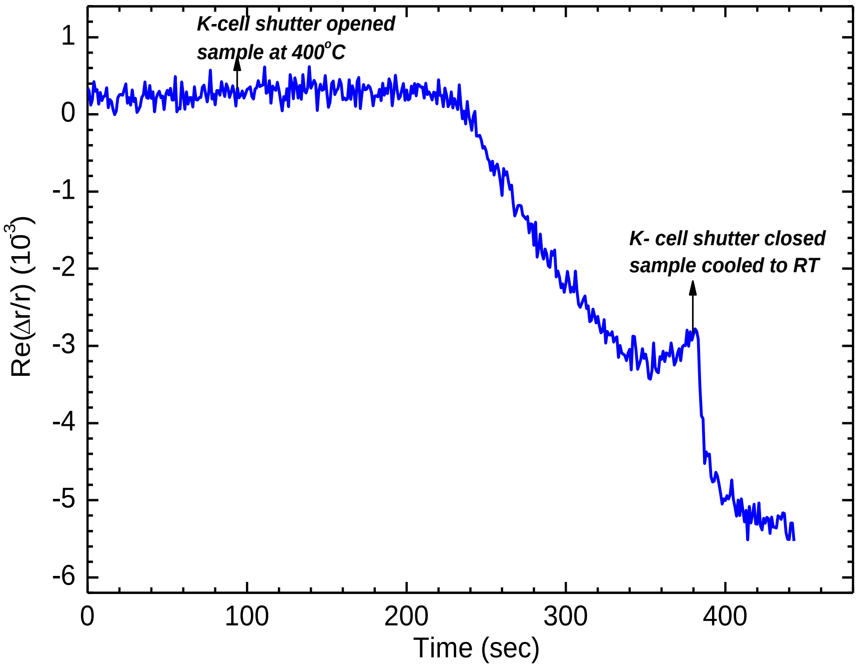

Figure 5.4 Transient of In deposition at 1.9 eV with sample at 400°C, where $\Delta r = r_{11} - r_{\perp}$.

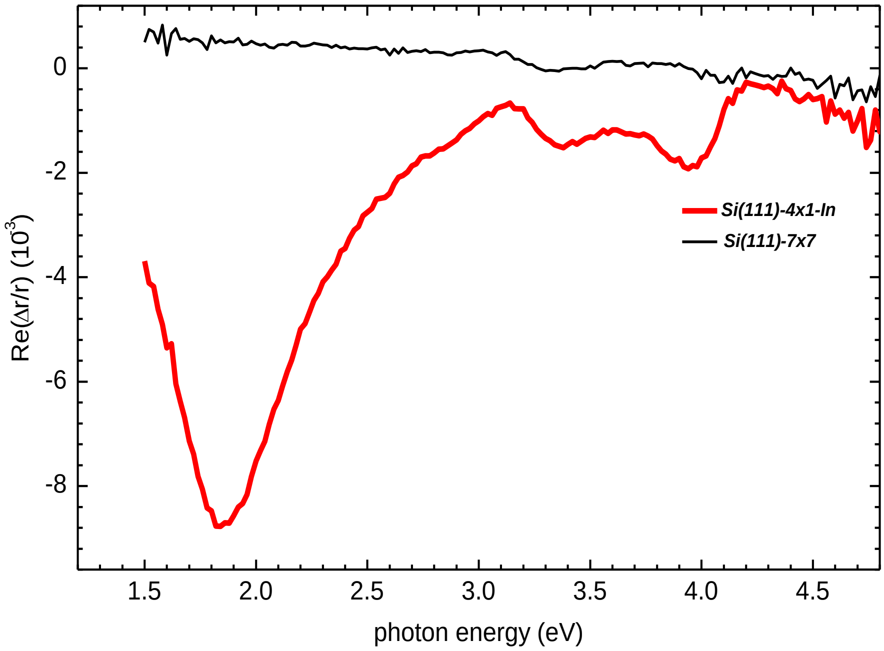

Figure 5.5 RAS spectra of clean Si(111)-2° offcut sample towards $[\bar{1}\,\bar{1}\,2]$ and In-induced (4×1) reconstruction, where $\Delta r = r_{11} - r_{\perp}$

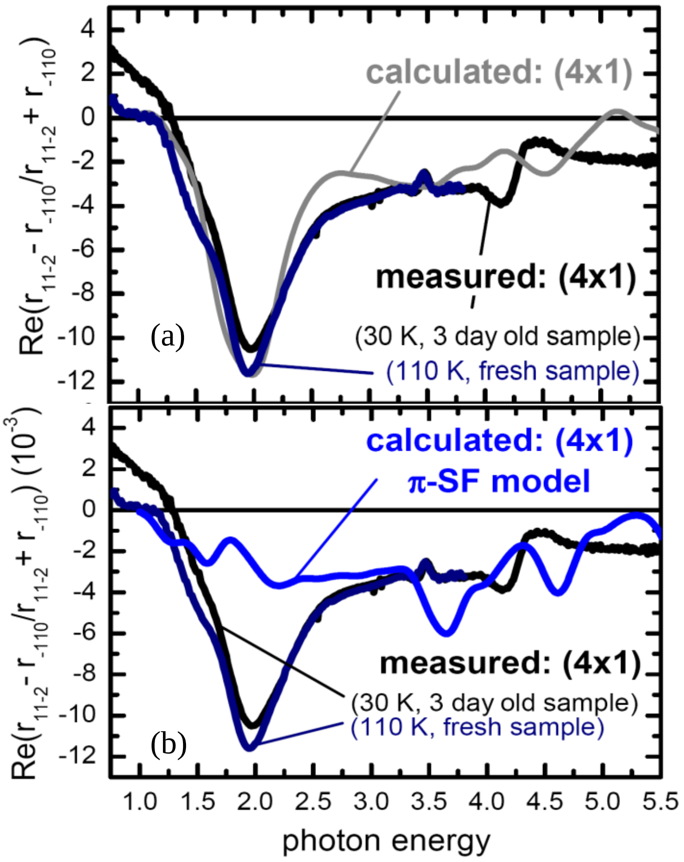

Figure 5.6 RAS spectrum of the (4×1)-In surface compared with calculations of the (a) Zig-Zag chain model (b) π-SF model [21].

The real part of the reflectance signal (equation (3.6)) from the surface layer of thickness, *d*, is given by

$$\mathrm{Re}\left[\frac{\Delta r}{r}\right] = \frac{4\pi d}{\lambda}\,\mathrm{Im}\left[\frac{\varepsilon_{yy} - \varepsilon_{xx}}{\varepsilon_b - 1}\right] = \frac{4\pi d}{\lambda}\,\mathrm{Im}\left[\frac{\varepsilon_{11} - \varepsilon_{\perp}}{\varepsilon_b - 1}\right] \tag{5.1}$$

where λ is the optical wavelength, ε_b is the bulk dielectric function, and ε_{ii} are the components of the surface dielectric function. $\varepsilon_{yy} = \varepsilon_{11}$ is parallel to the step edges ($[1\bar{1}0]$ direction), while $\varepsilon_{xx} = \varepsilon_{\perp}$ is perpendicular to step edges ($[\bar{1}\bar{1}2]$ direction). The negative sign of the 1.9 eV peak suggests a dominant polarizability in the *x*-direction, perpendicular to the In chains, presumably arising from the Si-In backbonds. In the IR region, below 1.2 eV, the anisotropy becomes positive [17, 18, 21], indicating that the polarizability along the chains becomes dominant in this spectral region. Based on the structural model proposed by Bunk *et al.* [10], recent *ab initio* calculations have produced (figure 5.6) excellent agreement with the experimentally observed optical anisotropy [21, 23]. Figure 5.6 also shows the sensitivity of the RAS response to surface structure, as the spectra clearly allow an alternative π-chain/stacking fault [24] to be excluded. Unfortunately, the density functional theory approach does not allow qualitative discussion of the nature of the bonding.

5.3 Si(111)-3×1-Ag

The growth of silver on Si(111) has been the focus of many studies, as a proto-typical metal-semiconductor interface. This is partially due to the fact that there is limited reaction or intermixing between the two species. Ag growth proceeds in a layer-by-layer-like fashion at room temperature (RT) with the overlayer showing features characteristic of bulk Ag after a few monolayers. Above about 200^{o}C, the growth process becomes a Stranski-Krastanov. At approximately 1 ML, the surface structure is characterized by a $\sqrt{3}\times\sqrt{3}$ periodicity and further deposition results in the nucleation of 3D Ag crystallites. In the submonolayer region, the $\sqrt{3}\times\sqrt{3}$ phase undergoes a transformation to an anisotropic, chain-like 3×1 structure when the surface is annealed at temperatures high enough to induce some desorption of Ag. Figures 5.7(a)-(d) show the various models proposed for the Si(111)-3×1-X reconstruction. The LeLay model (figure 5.7(a)) consists of adsorbate rows along $<1\bar{1}0>$ separated by two empty rows, giving an absolute coverage of 1/3 ML [25]. The model of Jeon *et al.* (figure 5.7(b)) has two adsorbate rows leaving one row of dangling bonds exposed, giving a coverage of 2/3 ML [26]. The model of Wan *et al.* (figure 5.7 (c)) consists of a missing row arrangement of Si atoms along $<1\bar{1}0>$ also with 2/3 ML coverage [27, 28]. In this Missing Top Layer (MTL) model metal atoms are bonded to the dangling bonds along the Si chains. However, half-filled dangling bonds still exist in the empty channels The Fan and Ignatiev model (figure 5.7(d)) consists of a missing row arrangement of Si atoms, but the metal atom positions were not considered since the reconstruction was thought to be impurity induced [8, 29].

Based on transmission electron diffraction results, a new model (CGM) was suggested [30]. The model consists of a partial Si double layer with a Si chain, and has a missing row where the adsorbate atoms lie. The Ag atoms bond to a single atom in the Si chain on one side of the trench and can bond to one of two atoms in the partial double layer on the other side. In this way, by choosing either the partial double layer atom in the $[\bar{1}10]$ direction or the one in the opposite direction, the Ag atom breaks the mirror symmetry along $[11\bar{2}]$. Such a picture explains the deviation towards p1 symmetry seen in STM images [9, 27] as well as the tip-induced shifting of entire rows between scans [9]. Starting from the CGM

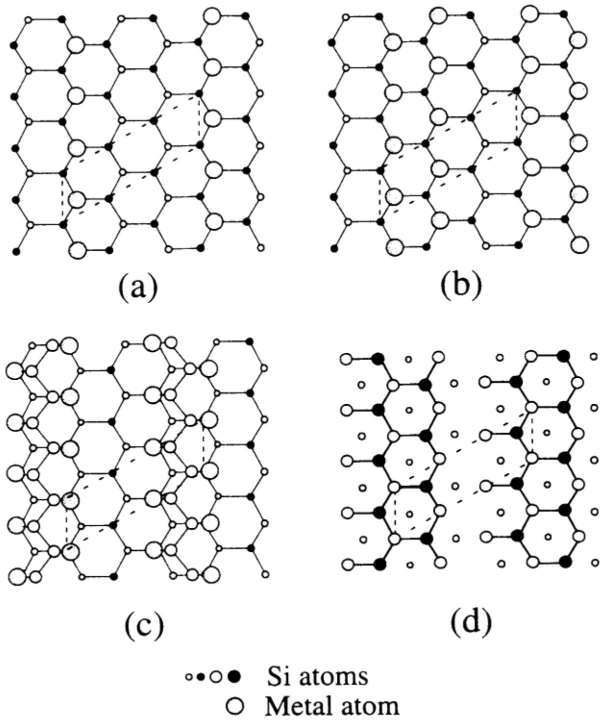

Figure 5.7 Structural models for the metal induced Si(111)-3×1-X reconstruction according to (a) LeLay *et al.* [25] (b) Jeon *et al.*[26] (c) Wan *et al.* [27, 28] (d) Fan *et al.*[8, 29]

model [30], Erwin and Weitering [31] proposed another model, the honeycomb chain-channel (HCC) model (figure 5.8), which exhibits the lowest energy of the any of the proposed structures to date. In the HCC structure, four Si atoms in the top layer construct a honeycomb chain lying in a plane parallel to the surface. The Ag atom sits in a channel formed by neighbouring honeycomb chains. The Ag atom occupies an asymmetric location with respect to the $[\bar{1}10]$ direction and thus breaks the mirror plane symmetry. Physically this asymmetry is attributed to formation of weak Ag-Si bonds, which favours twofold coordination of the Ag atom. The HCC model is supported by an ARUPS study of the single domain surface [32]. ARUPS measurements, in both the $\bar{\Gamma}-\bar{M}$ and $\bar{\Gamma}-\bar{K}$ directions of the (1×1) SBZ, corresponding to the $[11\bar{2}]$ and the $[10\bar{1}]$ crystallographic directions, detected no photoemission intensity at the Fermi level, in either direction confirming that the Si(111)-3×1-Ag reconstruction is a semi-conducting surface. The electronic band structures show that there are at least two surface states in the $\bar{\Gamma}-\bar{K}$ direction, and at least two in the $\bar{\Gamma}-\bar{M}$ direction.

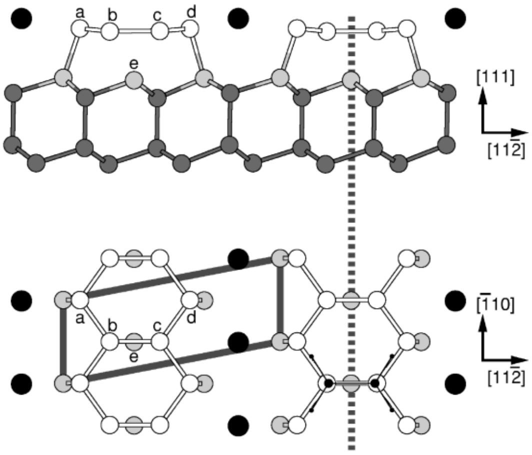

Figure 5.8 Ball and stick model of the HCC structure. Black circle are X atoms. White, light grey, and dark grey circles are the surface layer, first layer, and deeper Si layers, respectively. The heavy dotted line is an approximate mirror-symmetry plane for the top two Si layers. The (3×1) surface unit cell is shown as a heavy solid line [31].

5.3.1 Sample preparation

The Ag films were deposited onto the substrate using a high temperature effusion cell. A slow deposition rate (0.1 ML/min) was used, with a crucible temperature of 820^{o}C. Here 1 ML corresponds to 7.8×10^{14} atoms/cm^{2}, the atomic density of a bulk-terminated Si(111) 1×1 surface. The thickness of the films was monitored using a quartz-crystal oscillator (QCO), which could be moved directly in front of the Ag source. The Ag coverage was determined by timed exposure to the source. The vicinal Si(111) sample was n-type, phosphorous doped, with a resistivity in the range 0.1–20 Ω cm, offcut by 1°, 2^{o} and 3^{o} towards the $[\bar{1}\,\bar{1}\,2]$ direction. Direct current heating of the sample produced a regular array of single height steps, as in section 4.2, with a sharp 7×7 LEED pattern forming after cooling. The clean Si(111) surface was exposed to less than 0.3-0.4 ML of Ag, at a substrate temperature of 600^{o}C.

5.3.2 RAS results

Measurements were performed with a RAS spectrometer, using the dual Si/InGaAs detector, which can measure down to 0.85 eV (section 4.3). RAS was used to follow the growth of Ag on the surface by monitoring the RAS transient at 2.2 eV. Figure 5.9 shows RAS transients of multi-domain Si(111)-3×1-Ag. After a sequence of flash heating to 1200^{o}C, a single domain structure was obtained, with noticeable change in the slope of the RAS transient (figure 5.9), and increased optical anisotropy. Figure 5.10(a) shows the LEED pattern, with the atomic chains aligned in the direction of the step edges. The preparation of the single-domain (3×1)-Ag structure became quite routine when RAS was used to monitor the surface reconstructions. Figure 5.10(b) shows RAS spectra of the (3×1)-Ag surfaces offcut 1^o, 2^o and 3^o towards $[\bar{1}\bar{1}2]$. The very small spectral features near 3.4 and 4.2 eV for the clean surface arise from step-modified bulk optical transitions across the direct silicon band gap, similar to those published by Yasuda *et al.* [33].

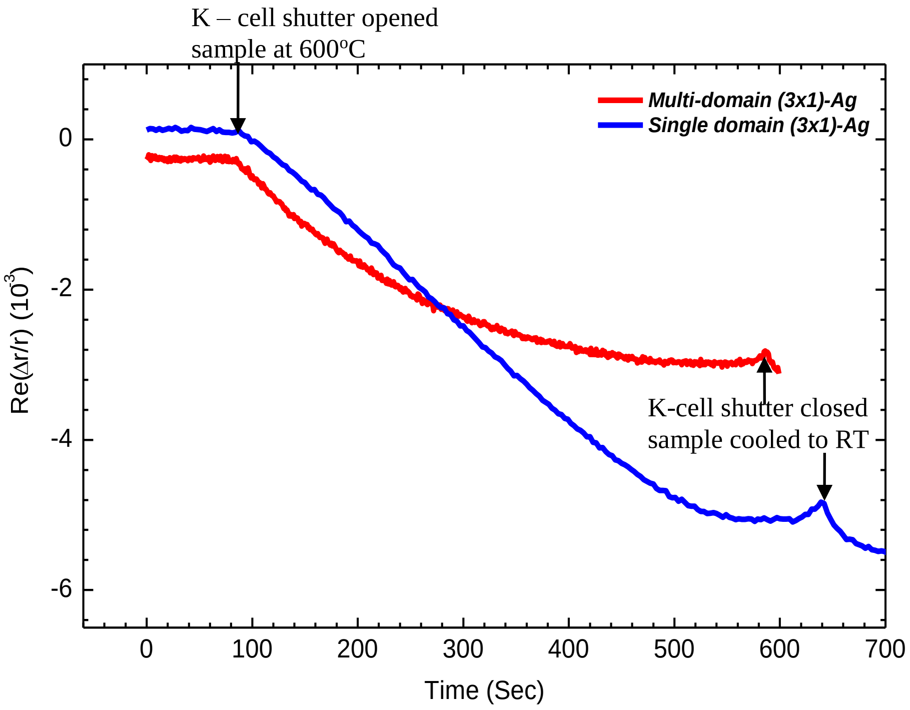

Figure 5.9 RAS transient at 2.2 eV of the formation of (3×1)-Ag surface on 3^o offcut Si(111) surface at 600°C, where $\Delta r = r_{11} - r_{\perp}$.

The RAS spectrum for the (3×1)-Ag surface is dominated by the negative feature at 2.2 eV. Defects and disorder in the surface, and domain averaging, reduce the anisotropy of the signal. The 2.2 eV feature can be unambiguously related to surface and interface states, as this energy region is far below the direct optical gap of Si. A differential photo-reflectance spectroscopy study of singular Si(111)-7×7-Ag, Si(111)-$\sqrt{3}\times\sqrt{3}$-Ag, and Si(001)-2×1–Ag interfaces found a wide peak around 2.3 eV [34]. This feature was interpreted as arising from electronic transitions involving localised interface states associated with covalent Ag-Si bond formation, giving a semiconductor character to these interfaces. It was suggested that the peak was an “optical signature” [34] of the bonding between Ag and Si atoms, as the feature was found for a variety of Ag/Si interfaces and appeared to be independent of the structure: the 2.2 eV feature in figure 5.10(b) may be another manifestation of this “optical signature”. Its negative nature indicates a dominant polarizability in the $[\bar{1}\bar{1}2]$ direction, orthogonal to the chains and steps. ARUPS data [32]

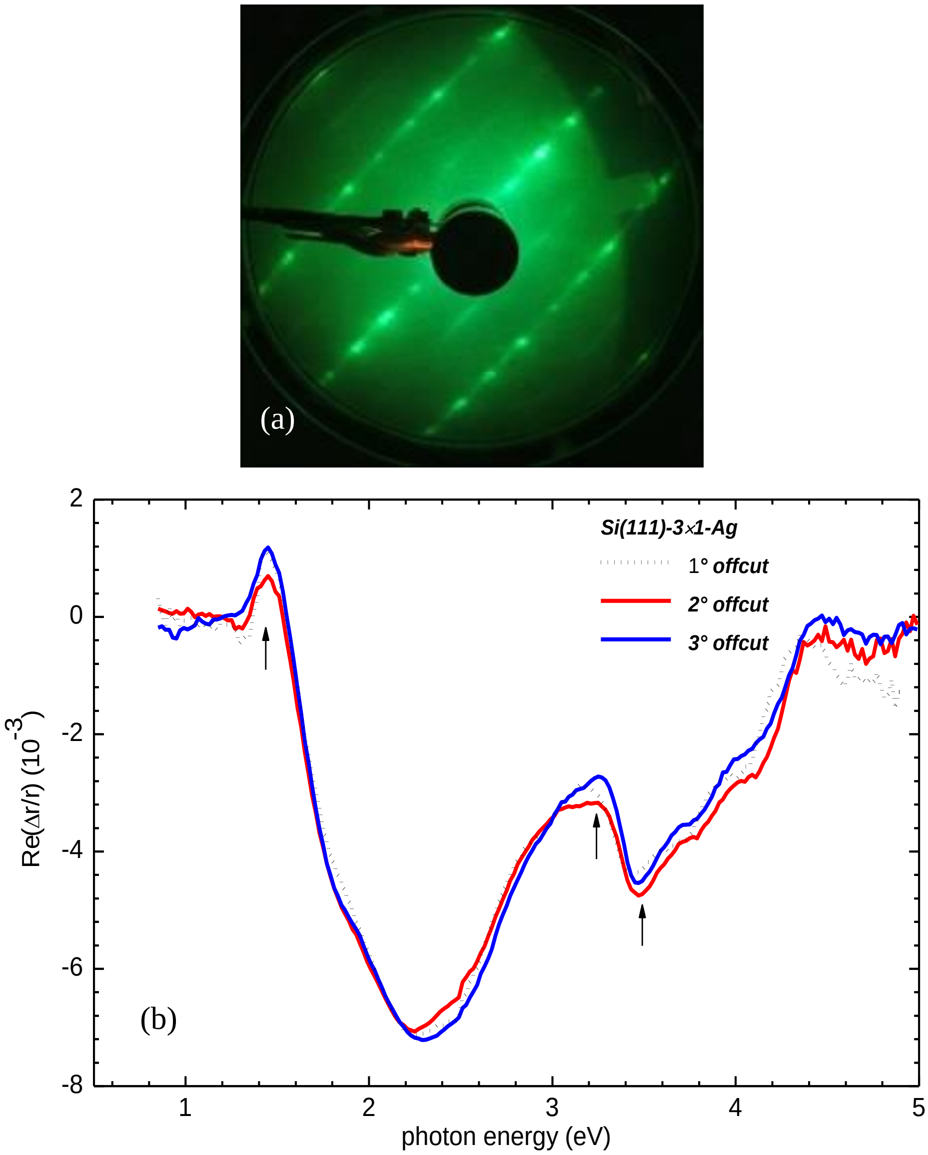

Figure 5.10 (a) LEED pattern of Si(111)-3×1-Ag at 70 eV (b) RA spectra of Si(111)-3×1-Ag on 1°, 2° and 3° offcut towards [$\bar{1}\,\bar{1}\,2$] samples, where $\Delta r = r_{11} - r_{\perp}$.

from this structure show that there are at least two surface states in the [$\bar{1}\,\bar{1}\,2$], $\bar{\Gamma} - \bar{M}$ direction, within ~1.5 eV of the Fermi level, that could contribute to optical transitions in this spectral region. The 2.2 eV feature showed a small decrease in intensity after one week in UHV, with LEED still showing a single domain 3×1 structure, although the third order spots were not as sharp. This is consistent with several transitions contributing to this feature, with only some being affected by surface contamination. Large and reproducible structures also appear at 1.4, 3.3 and 3.5 eV (see arrows in figure 5.10(b)). The changes in spectra above 3.1 eV are complicated by the onset of bulk related features, but any features below are surface specific. The negative, broad, composite feature around 2.2 eV is very similar to features observed in other metal induced chain-like structures of Si(111)-4×1–In, Si(111)-5×2–Au and Si(111)-3×1-Ca [35]. For Si(111)-5×2-Au, the optical anisotropy has been attributed to the effects of transverse bonding in the $[\bar{1}\bar{1}2]$ direction, within the Au-induced chain structures on the 5×2 terraces [36]. When the RAS data for the (3×1)-Ag and (3×1)-Ca structures are also considered, it appears likely that the large negative composite feature is directly related to the covalent backbonds between the Si and adsorbate atoms, and that this signature appears in the RA spectra on formation of Si(111)-m×n–X structures, with $m \neq n$, as these have anisotropic unit cells.

The other area of interest is the region below 1 eV, where Si(111)-4×1-In shows a positive anisotropy that is associated, at least in part, with a Drude-like response arising from a dominant metallic polarizability along the In chains [20]. In contrast, the negligible RAS response from Si(111)-3×1–Ag below 1 eV is consistent with its semiconducting character [32]. Finally, figure 5.10(b) shows that the change in the step density arising from the variation in vicinal angle has a negligible effect on the main features of the RAS spectra.

5.4 Si(111)-5×2-Au

Gold on Si(111) exhibits a particularly rich phase diagram containing both 1D and 2D structures. At the lowest coverage, a Si(111)-5×2-Au phase is observed that consists of stripes with 1D character. With higher coverage several 2D phases are formed, such as two related $\sqrt{3}\times\sqrt{3}$ phases and, eventually, a 6×6 structure that consists of an ordered array of $\sqrt{3}\times\sqrt{3}$ domains [37]. There are opportunities for using stepped Si(111) surfaces to produce tailored, 1D structures with exotic electronic states, which have been extensively explored by Himpsel *et al.* in particular [38-40]. Low step densities with miscut angle of about 1^{o} stabilize a single domain of the 1D 5×2 structure. High miscut angles such as 9.5^{o} for Si(557) create a whole new category of one-dimensional structures that incorporate a step into the unit cell [40]. The 5×2 surface phase forms in the coverage regime 0.4 - 0.5 ML. Early LEED studies [41, 42] suggested that the surface consists of rows of (5×2) unit cells where neighbouring rows may be in phase or out of phase. STM images showed the surface to be decorated by bright protrusions with apparent height ~0.15 nm. Away from the protrusions, STM images showed a “Y”-shaped topograph of a *2a* spacing [43]. Bright protrusions in STM images have been identified as Si adatoms by evaporating small amounts of Si and Au onto the reconstructed surface [44]. While extra silicon increases the density of protrusions, extra Au transforms the reconstruction partially into a Si(111)-$\sqrt{3}\times\sqrt{3}$ reconstruction.

Several structural models have been proposed for Si(111)-5×2-Au. The model proposed by Marks and Plass [45] based on high resolution electron microscopy and electron diffraction, consists of two rows of Au atoms lying over Si missing rows plus a *2a* missing arrangement of Si adatoms (*a* is the unit length of the (1×1) surface, 0.387 nm). Another model proposed by Hasegawa *et al.* [46] also contain two rows of Au atoms but with a different bonding configuration. It consists of a Si trimer instead of a Si adatom and two fewer Si atoms in the first double layer. These two models were modified subsequently to explain the observed features in an ARUPS and STM study [47].

A new model proposed recently for the Si(111)-5×2-Au is consistent with the experimental data [48]. The model is closely related to the widely "honeycomb chain-channel" (HCC) model of Si(111)-3×1-X structures discussed in section 5.3 [31]. The model shown in figure 5.11 has the basic structure of a double honeycomb chain (DHC) with underlying 5×1 periodicity. One chain is formed by hexagons of alternating Au and Si atoms, and the other by hexagons of all Si atoms, as in the HCC model. Simulated STM images from this model reproduce a number of experimentally observed features, including the in-plane location and apparent height of the bright protrusions due to the adatoms, and the Y-shaped features seen away from these protrusions.

Another important effect which occurs during metal adsorption on semiconductors is the large-scale modification of the surface morphology, such as faceting. Due to the symmetry of bulk Si crystal structure, the surface misoriented toward $[11\bar{2}]$ and $[\bar{1}\bar{1}2]$ have inherently different structures from each other. These two surfaces have different chemical bond configurations at step edges: one dangling bond (DB) at a step-edge Si atom for the $[11\bar{2}]$-directed miscut; while two DBs for the $[\bar{1}\bar{1}2]$. On vicinal Si(111) surfaces misoriented towards the $[\bar{1}\bar{1}2]$ direction, the formation of (557) facets has been observed by RHEED after adsorption of 0.2 ML of Au and further annealing to 600^{o}C [49]. Upon Au adsorption on vicinal Si(111) surface misoriented towards $[11\bar{2}]$, it was observed by STM that (775) and (995) facets with (1×2) and (1×3) symmetry form for T>650^{o}C at 0.7 ML. The Si(775)-1×2 structure appeared to be closely related to the Si(111)-5×2-Au surface reconstruction. Additional adsorption of 0.5 ML of Au, giving a total coverage of 1.2 ML of Au, causes the formation of Si(111)-$\sqrt{3}\times\sqrt{3}$-Au and the disappearance of the (775) facets [50].

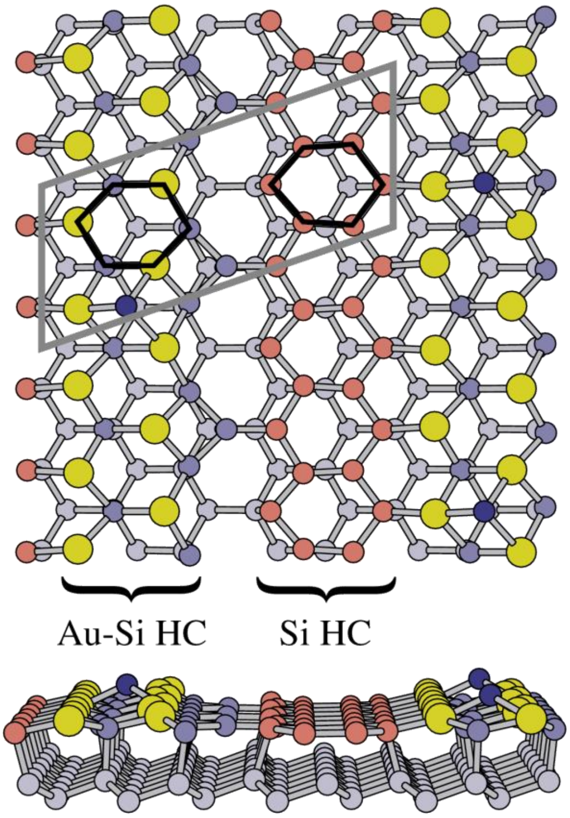

Figure 5.11 ‘‘Double honeycomb chain’’structure of Si(111)-5×2-Au. Large circles are Au, small circles are Si. The elementary 5×2 unit cell is outlined. Each unit cell contains two honeycomb chains (HC) based on the outlined hexagons, one of alternating Au and Si atoms, the other of all Si [48]).

STM studies of Au deposition (0.3 ML) on a vicinal Si(111) surface misoriented 4^{o} toward $[11\bar{2}]$, found that the Au adsorption transformed bunched steps into well-ordered, Au adsorbed (111) terraces [51]. Gold adsorption on Si(557) (vicinal Si(111) miscut 9.5^{o} towards $[\bar{1}\bar{1}2]$), produces a series of facets depending on coverage. The clean surface shows a periodic arrangement of narrow surfaces with the 7×7 structure, separated by triple steps running along the $[\bar{1}10]$ direction. At 0.2 ML coverage, the surface becomes a uniform (557) facet with a terrace width of 1.88 nm [52]. This surface has been a centre of discussion about exotic LD electronic structure [53, 54].

Figure 5.12(a) shows the structural model proposed for Si-(557)-Au [40] . The structure consists of a single gold chain in the unit cell. Adsorption of 0.25 ML of Au on the Si(775) offcut (miscut 8.5^{o} towards $[11\bar{2}]$, produces a uniform (775) facet structure. Figure 5.12(b) shows the structural model proposed for the (775) facet. The model consists of two Au chains per unit cell, very similar to that of the S(111)-5×2-Au [55]. Both surfaces have a high band filling with extra flat bands near the Fermi level giving them metallic character, which prompted the use of a structure similar to Si(111)-5×2-Au as a model for the terrace of Si(775)-Au [40]. ARUPS measurement on a single domain Si(111)- 5×2-Au revealed a quasi-1D metallic nature. The spectra recorded parallel to the chains showed spectral intensity at the Fermi level, characteristic of a metallic material while the spectra recorded perpendicular to the chains showed a lack of spectral intensity [56].

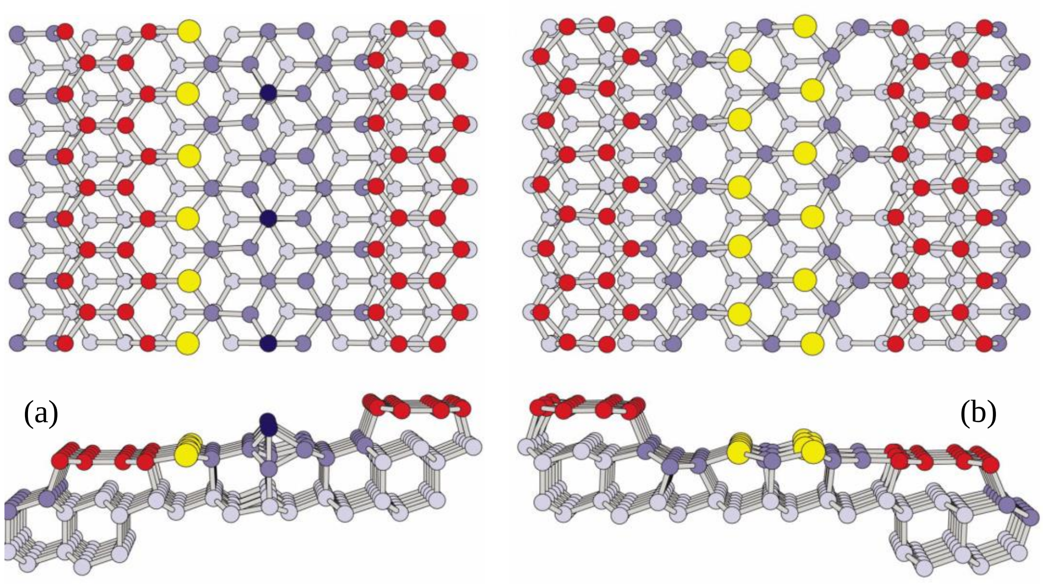

Figure 5.12 Structural models for gold chain structures on vicinal Si(111). Large circles are Au, small circles are Si, and dark blue circles are Si adatoms (a) Si(557)-Au (b) Si(775)-Au [40].

5.4.1 Sample preparation

Vicinal Si(111) substrates were used, offcut 2^{o}, 3^{o} and -4^{o} towards $[\bar{1}\bar{1}2]$, together with Si(557). Gold was deposited from a high temperature Knudsen cell, keeping the pressure below 4×10^{-10} mbar. The samples were held at 600^{o}C during Au deposition and the formation of the (5×2) was monitored *in situ* with RAS. Post-deposition annealing at 600^{o}C maximised the RAS signal, resulting in well ordered, single domain (5×2) surfaces (figure 5.13(a)). Si(557) only formed a (5×1)-Au structure, with no trace of $(\sqrt{3}\times\sqrt{3})$ LEED spots (figure 5.13(b)). Other methods of preparation were explored, such as stepwise room temperature deposition, followed by annealing [36]. However, no systematic variation in RAS line shape was found, and the RAS amplitude – and hence surface ordering – was maximised by using the first procedure.

5.4.2 RAS results of Si(111) - offcut dependence

The RAS spectra of the (5×2)-Au and (5×1)-Au structures prepared on the vicinal Si(111) samples, are shown in figure 5.14(a). As mentioned previously, the amplitude of the response will be reduced by any domain averaging. The clean (7×7) surfaces are shown in figure 5.14(b) for comparison, where the only significant difference with offcut occurs near the E_1 and E_2 bulk critical points, marked in the figure, where step-related features are known to occur [33], possibly strain related [57]. The difference between the -4° and 3° offcut, $\delta r / r$, is plotted in figure 5.14(c) for the (7×7) and (5×2) surfaces. The similarity of these plots near the bulk critical point region, where figure 5.14(b) shows a significant difference, indicates that there is no evidence of major step reconstruction or strain relief on Au deposition. The spectra differ considerably with the direction of offcut in the spectral region around 1.8 eV. As discussed in section 5.4, the major difference that occurs with offcut direction is that only single Au chains form on the terraces near the steps of $[\bar{1}\bar{1}2]$ offcuts, while double Au chains can form near the steps of $[11\bar{2}]$ offcuts [40]. The extreme example of this is Si(557)-5×1-Au, where only single Au chains form and the (5×2) LEED structure is not observed. The RAS spectrum of the (5×1) structure (see figure 5.14(a)) has a narrower minimum at 2.5 eV, compared to the broader minima found for all the (5×2) samples. The spectra of the 2° and 3° samples can be generated by using a linear combination of the (5×1) response of single Au chains and the (5×2) response of the double Au chains of the -4° sample.

Below about 1.2 eV, the RAS signal is positive, indicating a dominant polarizability along the chain direction. These results show, for the first time, an intriguing difference in the anisotropic optical response of the single- and double-chain structures. It is clear from figure 5.14 that the single-chain structure has much lower polarizability in the 0.8 to 1.2eV spectral region. The density of states at the Fermi level of the single-chain structure is known to be lower from ARUPS measurements [40], but the RAS measurements do not extend far enough into IR to conclude that different Drude-free carrier tails are being observed. However, the dramatic difference between the single- and double-chain structures in this spectral region will provide a stringent test of *ab initio* calculations of the anisotropic response.

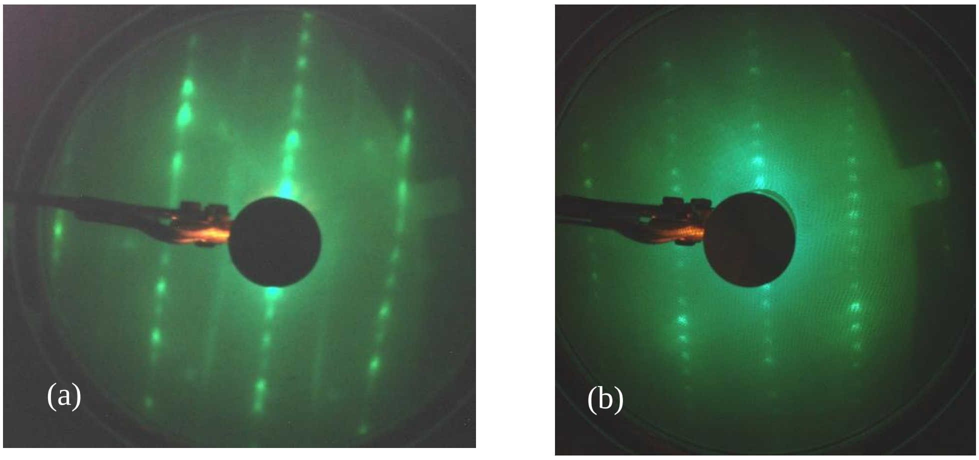

Figure 5.13 LEED pattern of (a) Si(111)-5×2-Au (b) Si(557)-5×1-Au

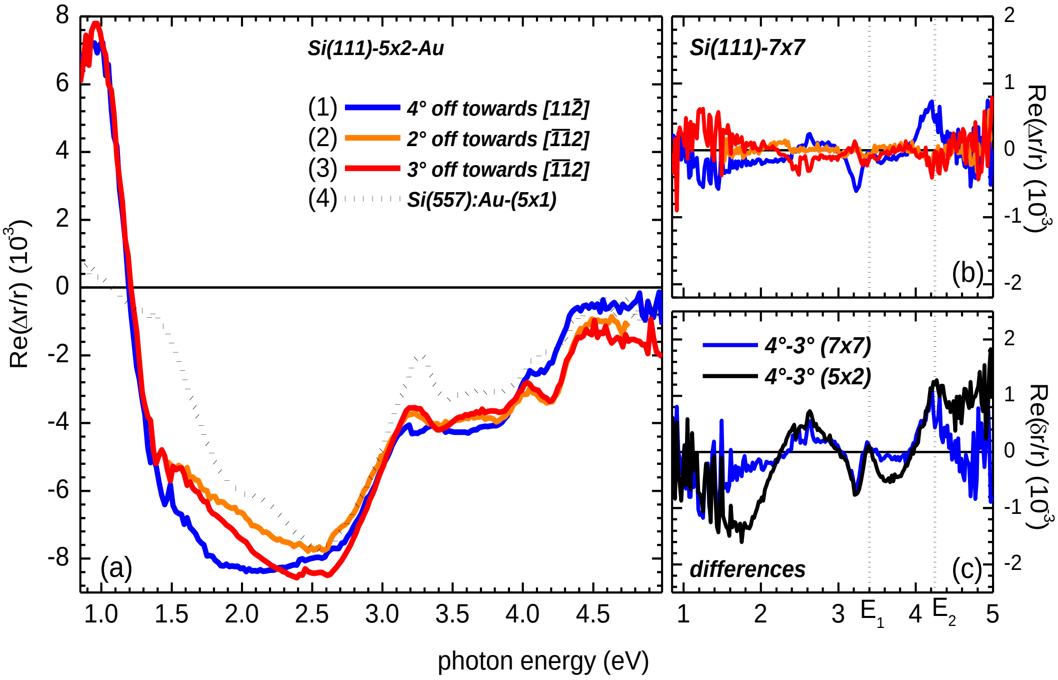

Figure 5.14 (a) RAS spectra of the Au-induced (5×2) surface on 2°, 3° and -4° offcut Si(111) and also Si(557)-5×1-Au, where $\Delta r = r_{11} - r_{\perp}$ (b) Spectra of the clean Si-(7×7) surface. The offcut dependence is best seen in the $\delta r / r$ spectra, (c), where the difference of the 3° and -4° sample is shown for the (7×7) and (5×2) surfaces. The *y*-axes of (a), (b) and (c) have different scales. The E_1 and E_2 bulk critical points are shown by dotted lines.

5.4.3 Preparation dependence

The RAS spectrum for the -4° offcut Si(111)-5×2-Au surface, shown in figure 5.14(a), differs significantly from the only previously published spectrum [36], also measured on p-type Si(111). Vicinal structures are often sensitive to the preparation method, and figure 5.15 compares RAS spectra of samples prepared by *in situ* monitoring during Au deposition on samples held at 600°C, post-annealed samples, and samples prepared by stepwise deposition at RT with subsequent annealing, as described in [36]. Two main conclusions can be drawn. Firstly, the sample prepared by Au deposition at 600°C, followed by a 20 minute post-annealing, shows the largest RAS amplitude and thus the largest single domain Si(111)-5×2-Au surface area, as both the Si(111)-7×7 and the Si(111)-$\sqrt{3}\times\sqrt{3}$ -Au surfaces are isotropic. Secondly, the general line shape of previous measurements for the same offcut could not be reproduced by any of the preparation methods. An overall reduction in amplitude indicates some domain averaging, but scaling still leaves a significant discrepancy. Systematic errors between the RAS spectrometers are excluded by similarity of the vicinal Si(111)-7×7 spectra. Also, reproducible results were obtained on a third RAS spectrometer by Dr. Sandhya Chandola at the Technische Universität, Berlin. The stepwise result is closest to the previous work and it is possible

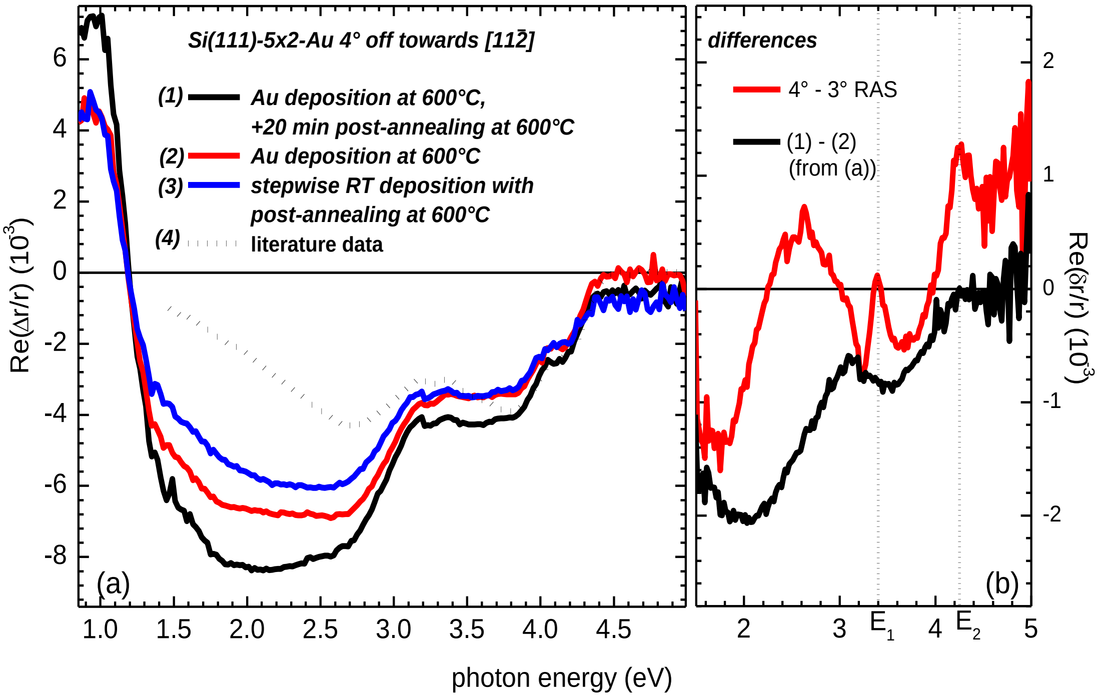

Figure 5.15 (a) RAS spectra of the Au-induced (5×2) surface on -4° offcut silicon for various preparation methods, where $\Delta r = r_{11} - r_{\perp}$ (b) $\delta r / r$ before and after annealing, compared with the difference between 3° and -4° sample from figure 5.14(c)

reducing the Au deposition rate of 1 ML in 5 minutes to the much lower value used previously (~1 ML in 50 minutes) would produce better agreement. The dependence in the RAS spectra on the detail of the preparation technique differs from previous studies of vicinal Si(111)-4×1-In [20] and Si(111)-3×1-Ag [58] structures. However, the vicinal Si(111)-Au system is known to show complex behaviour. Annealing such samples can alter terrace widths and step structure, while Si adatom structures can form on the Au chains [48], as discussed in section 5.4. However, figure 5.15(b) shows that, spectra taken before and after annealing are similar to offcut-dependent differences, and it appears likely that at least some of the difference from the previous work arises from small variations in the single to double Au chain population.

References

1. Ofner H, Surnev SL, Shapira Y, Netzer FP: **In overlayers on Si(111)7*7: growth and evolution of the electronic structure.** *Physical Review B-Condensed Matter* 1993, **48:**10940-10949.
2. Hansson GV, Nicholls JM, Martensson P, Uhrberg RIG: **Electronic structure of Si(111) surfaces with group III ad-atoms.** *Surface Science* 1986, **168:**105-113.
3. Kinoshita T, Ohta H, Enta Y, Yaegashi Y, Suzuki S, Kono S: **Empty- and filled-electronic states of the Si(111) sqrt[3]*sqrt[3]-Sn, sqrt[3]*sqrt[3]-In and 2sqrt[3]*2sqrt[3]-Sn surfaces.** *Journal of the Physical Society of Japan* 1987, **56:**4015-4021.
4. Nicholls JM, Reihl B, Northrup JE: **Unoccupied surface states revealing the Si(111) sqrt[3]*sqrt[3]-Al,-Ga, and -In adatom geometries.** *Physical Review B (Condensed Matter)* 1987, **35:**4137-4140.
5. Nogami J, Park S, Quate CF: **Indium-induced reconstructions of the Si(111) surface studied by scanning tunneling microscopy.** *Physical Review B (Condensed Matter)* 1987, **36:**6221-6224.
6. Hirayama H, Baba S, Kinbara A: **Electron energy loss spectra of In/Si(111) superstructures.** *Japanese Journal of Applied Physics, Part 2 (Letters)* 1986, **25:**452-454.
7. Hill IG, McLean AB: **Role of Si adatoms in the Si(III)-Au(5*2) quasi-one-dimensional system.** *Physical Review B: Condensed Matter* 1997, **55:**15-664.
8. Fan WC, Ignatiev A: **Metal-adsorbate-induced Si(111)-(1*3) reconstruction.** *Physical Review B (Condensed Matter)* 1990, **41:**3592-3595.
9. Carpinelli JM, Weitering HH: **Scanning tunneling microscopy study of the metal-induced Si(111)3*1 reconstruction: evidence for dimerized chain formation.** *Surface Science* 1995, **331-333:**1015-1021.
10. Bunk O, Falkenberg G, Zeysing JH, Lottermoser L, Johnson RL, Nielsen M, Berg-Rasmussen F, Baker J, Feidenhans'l R: **Structure determination of the indium-induced Si(111)-(4*1) reconstruction by surface X-ray diffraction.** *Physical Review B-Condensed Matter* 1999, **59:**12228-12231.
11. Hasegawa S: **Surface-state bands on silicon as electron systems in reduced dimensions at atomic scales.** *Journal of Physics Condensed Matter* 2000, **12:**463-495.

12. Abukawa T, Sasaki M, Hisamatsu F, Goto T, Kinoshita T, Kakizaki A, Kono S: **Surface electronic structure of a single-domain Si(111)4*1-In surface: a synchrotron radiation photoemission study.** *Surface Science* 1995, **325:**33-44.
13. Hill IG, McLean AB: **Metallicity of In chains on Si(111).** *Physical Review B-Condensed Matter* 1997, **56:**15725-15728.
14. Yeom HW, Takeda S, Rotenberg E, Matsuda I, Horikoshi K, Schaefer J, Lee CM, Kevan SD, Ohta T, Nagao T, Hasegawa S: **Instability and charge density wave of metallic quantum chains on a silicon surface.** *Physical Review Letters* 1999, **82:**4898-4901.
15. Kumpf C, Bunk O, Zeysing JH, Su Y, Nielsen M, Johnson RL, Feidenhans'l R, Bechgaard K: **Low-temperature structure of indium quantum chains on silicon.** *Physical Review Letters* 2000, **85:**4916-4919.
16. Pedreschi F, Omahony JD, Weightman P, Power JR: **Evidence of electron confinement in the single-domain (4*1)-In superstructure on vicinal Si(111).** *Applied Physics Letters* 1998, **73:**2152-2154.
17. Fleischer K, Chandola S, Esser N, Richter W, McGilp JF: **Reflectance anisotropy spectroscopy of Si(111)-(4*1)-In.** *physica status solidi (a)* 2001, **188:**1411-1416.
18. Fleischer K, Chandola S, Esser N, Richter W, McGilp JF: **Phonon and polarized reflectance spectra from Si(111)-(4*1)In: evidence for a charge-density-wave driven phase transition.** *Physical Review B (Condensed Matter and Materials Physics)* 2003, **67:**235318-235311.
19. Fleischer K: **Optical anisotropy and vibrational properties of Sn, In and Cs nanowires.** PhD thesis, Technischen Universitat 2005.
20. Fleischer K, Chandola S, Herrmann T, Esser N, Richter W, McGilp JF: **Free-electron response in reflectance anisotropy spectra.** *Physical Review B (Condensed Matter and Materials Physics)* 2006, **74:**195432-195410.
21. Fleischer K, Chandola S, Esser N, Richter W, McGilp JF, Schmidt WG, Wang S, Lu W, Bernholc J: **Atomic indium nanowires on Si(111): the (4*1)-(8*2) phase transition studied with reflectance anisotropy spectroscopy.** *Applied Surface Science* 2004, **234:**302-306.
22. Aspnes DE, Studna AA: **Anisotropies in the above-band-gap optical spectra of cubic semiconductors.** *Physical Review Letters* 1985, **54:**1956-1959.
23. Shuchun W, Wenchang L, Schmidt WG, Bernholc J: **Nanowire-induced optical anisotropy of the Si(111)-In surface.** *Physical Review B (Condensed Matter and Materials Physics)* 2003, **68:**35329-35321.
24. Saranin AA, Khramtsova EA, Ignatovich KV, Lifshits VG, Numata T, Kubo O, Katayama M, Katayama I, Oura K: **Indium-induced Si(111)4*1 silicon substrate atom reconstruction.** *Physical Review B-Condensed Matter* 1997, **55:**5353-5359.
25. Le Lay G: **Physics and electronics of the noble-metal/elemental-semiconductor interface formation: a status report.** *Surface Science* 1983, **132:**169-204.
26. Jeon D, Hashizume T, Sakurai T, Willis RF: **Structural and electronic properties of ordered single and multiple layers of Na on the Si(111) surface.** *Physical Review Letters* 1992, **69:**1419-1422.
27. Wan KJ, Lin XF, Nogami J: **Comparison of the 3*1 reconstructions of the Si(111) surface induced by Li and Ag.** *Physical Review B (Condensed Matter)* 1992, **46:**13635-13638.
28. Wan KJ, Lin XF, Nogami J: **Surface reconstructions in the Ag/Si(111) system.** *Physical Review B (Condensed Matter)* 1993, **47:**13700-13712.
29. Fan WC, Ignatiev A: **Reconstruction of the Si(111) surface induced by alkali metals.** *Surface Science* 1993, **296:**352-357.
30. Collazo-Davila C, Grozea D, Marks LD: **Determination and refinement of the Ag/Si(111)-(3*1) surface structure.** *Physical Review Letters* 1998, **80:**1678-1681.

31. Erwin SC, Weitering HH: **Theory of the "honeycomb chain-channel" reconstruction of M/Si(111)-(3*1).** *Physical Review Letters* 1998, **81:**2296-2299.
32. Gurnett M, Gustafsson JB, Magnusson KO, Widstrand SM, Johansson LSO: **Angle-resolved photoemission study of the single-domain Si(111)(3*1)/(6*1)-Ag surface.** *Physical Review B-Condensed Matter* 2002, **66:**161101-161101-161104.
33. Yasuda T, Aspnes DE, Lee DR, Bjorkman CH, Lucovsky G: **Optical Anisotropy of Singular and Vicinal Si-Sio2 Interfaces and H-Terminated Si Surfaces.** *Journal of Vacuum Science & Technology a-Vacuum Surfaces and Films* 1994, **12:**1152-1157.
34. Borensztein Y, Alameh R: **Optical evidence for interface electronic states at Ag/Si interfaces.** *Surface Science* 1992, **274:**509-514.
35. McGilp JF, Chandola S: *unpublished work.*
36. Power JR, Weightman P, O'Mahony JD: **Strong optical anisotropy of the single-domain 5*2-Au reconstruction on vicinal Si(111).** *Physical Review B-Condensed Matter* 1997, **56:**3587-3590.
37. Le Lay G, Faurie JP: **AES study of the very first stages of condensation of gold films on silicon (111) surfaces.** *Surface Science* 1977, **69:**295-300.
38. Crain JN, Kirakosian A, Altmann KN, Bromberger C, Erwin SC, McChesney JL, Lin JL, Himpsel FJ: **Fractional band filling in an atomic chain structure.** *Physical Review Letters* 2003, **90:**176805/176801-176804.
39. Losio R, Altmann KN, Kirakosian A, Lin J-L, Petrovykh DY, Himpsel FJ: **Band splitting for Si(557)-Au: Is it spin-charge separation?** *Physical Review Letters* 2001, **86:**4632-4635.
40. Crain JN, McChesney JL, Fan Z, Gallagher MC, Snijders PC, Bissen M, Gundelach C, Erwin SC, Himpsel FJ: **Chains of gold atoms with tailored electronic states.** *Physical Review B (Condensed Matter)* 2004, **69:**125401-125401.
41. Bishop HE, Riviere JC: **Segregation of gold to the silicon (111) surface observed by Auger emission spectroscopy and by LEED.** *British Journal of Applied Physics (Journal of Physics D)* 1969, **2:**1635-1642.
42. Lipson H, Singer KE: **Disorder in a film of gold deposited on silicon: investigation by low-energy electron diffraction.** *Journal of Physics C (Solid State Physics)* 1974, **7:**12-14.
43. O'Mahony JD, McGilp JF, Flipse CFJ, Weightman P, Leibsle FM: **Nucleation and Evolution of the Au-Induced 5*2 Structure on Vicinal Si(111).** *Physical Review B* 1994, **49:**2527-2535.
44. Kirakosian A, Crain JN, Lin J-L, McChesney JL, Petrovykh DY, Himpsel FJ, Bennewitz R: **Silicon adatoms on the Si(1 1 1)5*2-Au surface.** *Surface Science* 2003, **532-535:**928-933.
45. Marks LD, Plass R: **Atomic structure of Si(111)-(5*2)-Au from high resolution electron microscopy and heavy-atom holography.** *Physical Review Letters* 1995, **75:**2172-2175.
46. Hasegawa T, Hosoki S, Yagi K: **Stable phase boundaries between the 7*7 and the 5*2 Au structures on a Si(111) surface studied by high-temperature STM.** *Surface Science* 1996, **355:**L295-L299.
47. Kang M-H, Lee JY: **Theoretical investigation of the Au/Si(111)-(5*2) surface structure.** *Surface Science* 2003, **531:**1-7.
48. Erwin SC: **Self-doping of gold chains on silicon: A new structural model for Si(111)-(5*2)-Au.** *Physical Review Letters* 2003, **91:**206101-206101.
49. Jalochowski M, Strak M, Zdyb R: **Gold-induced ordering on vicinal Si(111).** *Surface Science* 1997, **375:**203-209.

50. Seehofer L, Huhs S, Falkenberg G, Johnson RL: **Gold-induced facetting of Si(111).** *Surface Science* 1995, **329:**157-166.
51. Shibata M, Sumita I, Nakajima M: **Scanning-tunneling-microscopy study of initial stages of Au adsorption on vicinal Si(111) surfaces.** *Physical Review B (Condensed Matter)* 1996, **53:**3856-3860.
52. Okino H, Matsuda I, Tanikawa T, Hasegawa S: **Formation of facet structures by Au adsorption on vicinal Si(111) surfaces.** *e-Journal of Surface Science and Nanotechnology* 2003, **1**.
53. Sanchez-Portal D, Martin RM: **First principles study of the Si(557)-Au surface.** *Surface Science* 2003, **532-535:**655-660.
54. Sanchez-Portal D, Gale JD, Garcia A, Martin RM: **Two distinct metallic bands associated with monatomic Au wires on the Si(557)-Au surface.** *Physical Review B (Condensed Matter and Materials Physics)* 2002, **65:**081401-081401.
55. Altmann KN, Crain JN, Kirakosian A, Lin JL, Petrovykh DY, Himpsel FJ, Losio R: **Electronic structure of atomic chains on vicinal Si(111)-Au.** *Physical Review B-Condensed Matter* 2001, **64:**035406/035401-035411.
56. Collins IR, Moran JT, Andrews PT, Cosso R, O'Mahony JD, McGilp JF, Margaritondo G: **Angle-resolved photoemission from an unusual quasi-one-dimensional metallic system: a single domain Au-induced 5*2 reconstruction of Si(111).** *Surface Science* 1995, **325:**45-49.
57. Rossow U, Mantese L, Aspnes DE: **Lineshapes of surface induced optical anisotropy spectra measured by RDS/RAS.** *Applied Surface Science* 1998, **123:**237-242.
58. Chandola S, Jacob J, Fleischer K, Vogt P, Richter W, McGilp JF: **Optical and electronic properties of Ag nanodots on Si(111).** *Journal of Physics: Condensed Matter* 2006, **18:**6979-6986.

6

RAS of uncapped and capped metal nanostructures

6.1 Overview

The first half of this chapter deals with RAS studies of the formation of In islands and the capping of In quasi-1D structures and islands with Si. The second half deals with RAS and STM studies of Ag nanodots and Ag islands on Si(111)-3×1-Ag, and their capping with Si. Capping with Si was not attempted for the Si(111)/Au system, because Au is known to react with Si at interfaces to form an alloy [1].

6.2 Metal nanostructures

The various methods to prepare metal nanostructures are discussed in chapter 2. A common characteristic of metal films grown on semiconductor systems is the appearance of preferred thicknesses, which are attributed to quantum size effects (QSE) in the electronic structure. These quantum-well states (resonances) have been reported to show, additionally, intriguing physical properties such as spin polarization, anomalous in-plane dispersion, and oscillation of the superconducting transition temperature with thickness [2]. Furthermore, it has been predicted that the Fermi surface topology can be changed by an interface layer (electronic topological phase transition). Such topological regulation induces various effects of geometry on the physical properties of electrons, attracting interest in LD physics and technology. Depending on the competition between the effects of quantum confinement, charge spilling and interface induced Friedel oscillations, different types of film stability are obtained, characterized by the existence of critical/magic thickness for smooth growth [2].

Deposition at low temperatures has attracted wide attention, since this kinetic path has allowed the growth of perfectly flat 2D films with apparently fully wetting properties, even for systems which should be non-wetting. By using two-step growth process consisting of deposition at low temperatures, followed by annealing to room temperature, growth of flat 2D Ag films have been achieved on a variety of Si substrates [3]. With increasing film thicknesses, Ag films on clean Si(111)-7×7 and Si(001)-2×1 surfaces exhibited clusters, islands with flat top terraces, interconnected islands and flat films with voids and also no voids [3]. Low energy electron microscopy (LEEM) and photoemission electron microscopy (PEEM) studies of high temperature (620^{o}C) self assembly of Ag on vicinal Si(001), miscut 4^o in the [110] direction, showed growth of wire-like structures, after the formation of an initial wetting layer [4]. The wires display quasi-1D behaviour as their length was observed to increase while their width remains constant. The length of the wires was observed to increase to more than 100 μm. It is believed that the step-bunches act as a barrier to surface diffusion in the direction perpendicular to the wire. The high temperature is sufficient for the slow diffusion along the steps to supply the ends of the wire with sufficient adatoms to continuously increase the wires length.

Surface morphology plays an important role in fabrication of nanowires on anisotropic crystalline substrates or anisotropic surface reconstructions. The anisotropy of the surface can influence the growth via anisotropic strain and the confinement of adatom diffusion to 1D. The role of anisotropic stain on the formation of elongated Ag islands has been shown in the case of Ag on Si(100) [4, 5]. Nanowires of Pb have also been grown on different vicinal Si substrates [6, 7]. This was achieved by controlled pre-faceting of the surface by depositing submonolayer coverages of Au at RT and annealing to high temperature. The Au-induced reconstructions create quasi-1D facets and superstructures. Parallel aligned mesoscopic wires were obtained during Pb deposition on substrates cooled slightly below room temperature. Wires with length to width ratio reaching 130 were obtained on Si(775) and the Si(553) substrates. The driving force for the formation of these mesoscopic wires has been attributed to the large misfit between the Pb and the Si lattice and 1D diffusion of Pb [6, 7].

The potential role of the quasi-1D interface in the formation of 1D electronic states has been shown by Ag film growth on the array of In chains, on the Si(111)-4×1-In surface. Electron motion in the film appears to be confined parallel to the interface and along the chain direction [8, 9]. ARUPS measurements have revealed that quantized states show parabolic dispersion along the In chain direction but negligible dispersion in the perpendicular direction.

6.3 Capped nanostructures

The nanostructures discussed above have to be protected from contamination and corrosion by the environment if they are to be the basis of useful electronic devices. In principle, ultra-thin capping layers can provide this protection. However, capping may change the shape and composition of nanostructures, altering their electronic properties. Even inhomogeneous strain due to the lattice mismatch between the nanostructure and the capping materials, may affect electronic properties.

Self-organised nanostructure arrays are ideal test structures to investigate changes in metallic properties upon capping. Optical techniques are ideally suited to probe the properties of buried nanostructures, as their penetration is significantly larger than that of conventional surface probes, (figure 4.3) and the lower symmetry of aligned nanostructures helps to discriminate the nanostructure response from the response of the interface and bulk [10]. Interface sensitive optical techniques are less important for larger nanostructures, such as the ~10 - 100 nm Ag dots grown on substrates like mica, where standard optical spectroscopies can be used to probe surface plasmon-polariton resonances, and the shifts in resonance frequency that occur on capping [11-13]. However, for ~1 nm nanostructures, where QSE becomes important, interface sensitivity is crucial. Several optical techniques are capable of probing the properties of buried nanostructures of this size. For example, RAS, can probe not only buried interfaces but has also been shown to be capable of extracting the conductance anisotropy of metallic nanowires [14].

6.4 In nanostructures

6.4.1 RAS results from In nanostructures

In island formation has been reported during STM studies on singular Si(111)-4×1-In surface [15]. STM images showed hexagonal metal islands of height ~0.3 nm, and a clear (1×1) LEED pattern was observed. The UPS and IPES spectra of the (1×1) surface indicated a flat, well-ordered surface layer, which displays no In bulk plasmon excitation but instead an interface plasmon in the EELS spectra [16]. Between 1 and 2 ML In coverage a metallic phase appears to be formed as evidenced by the DOS at the Fermi-level. In this work, approximately 3 ML of In was deposited on a 2^o offcut Si(111)-7×7 surface, held at 400^{o}C. Figure 6.1(a) shows the RHEED pattern, and figure 6.1(b) shows the RAS transient at 1.6 eV. It can be seen that the RHEED still shows the presence of a (4×1)-In structure showing that the coverage is not enough to form a full (1×1) structure and that the area fraction on the surface covered by Indium islands is smaller than the previous studies [15, 16]. The 1.6 eV transient, close to the 1.9 eV minimum, (figures 5.5 and 6.2) shows the formation of the (4×1)-In structure, and then the loss of this signal as

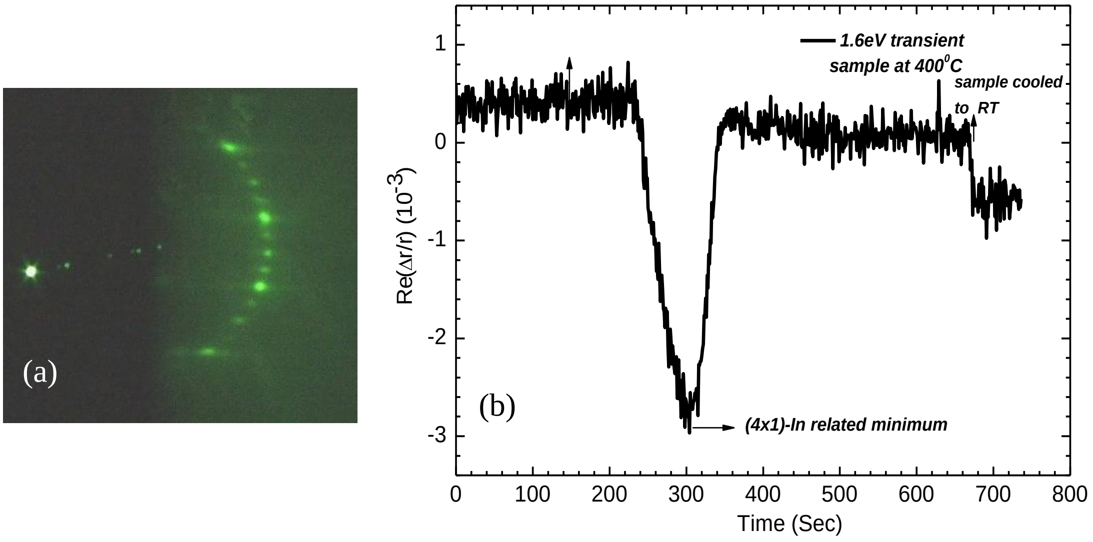

Figure 6.1 (a) RT RHEED pattern of ~3 ML of In on Si(111)-7×7 surface offcut by 2^o towards [$\bar{1}\,\bar{1}\,2$], held at 400^{o}C. (b) RAS transient at 1.6 eV during In deposition, where $\Delta r = r_{11} - r_{\perp}$.

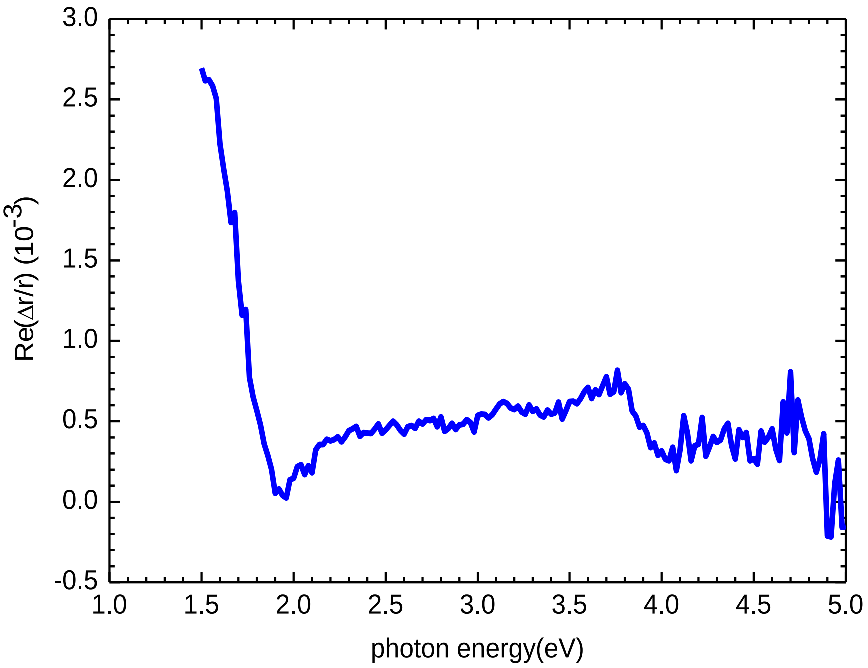

Figure 6.2 RAS of ~3 ML of In on Si(111)-7×7 surface offcut by 2° towards $[\bar{1}\,\bar{1}\,2]$, held at 400°C, where $\Delta r = r_{11} - r_{\perp}$.

the islands form. The RAS spectrum (figure 6.2) of 3 ML coverage shows only a small (4×1)-In related signal at 1.9 eV in a spectrum dominated by a large positive signal below 1.8 eV. The spectral range of the RAS system was limited to 1.5 eV by the PMT detector. The large positive response is consistent with the presence of anisotropic metal islands with long axes parallel to the step edges. The mobility of In atoms is reportedly high [17], which should favour the formation anisotropic islands on stepped Si(111) surfaces. This is discussed further in section 6.5.

6.4.2 RAS results from capping studies of Si(111)-4×1-In

An attempt was made to cap the ordered surface of Si(111)-4×1-In using an amorphous Si (a-Si) layer. A major problem of capping such structures is the potential perturbation or destruction of the quasi-1D character of the nanostructure. The preparation details of (4×1)-In Surface is given in section 5.2.1. Silicon was deposited from a resistively heated Si bar at a rate of approximately 0.05ML/minute. The rate was estimated by depositing Si on Si(111)-5×2-Au, and using the Si LVV and Au NOO Auger intensities, the Auger response having been previously calibrated using Au deposition on Si(111). The stability of the reconstruction was monitored using RAS. Figure 6.3 shows the RAS transient at 1.9 eV during Si deposition with sample at RT. It can be seen that (4×1)-In related RAS signal

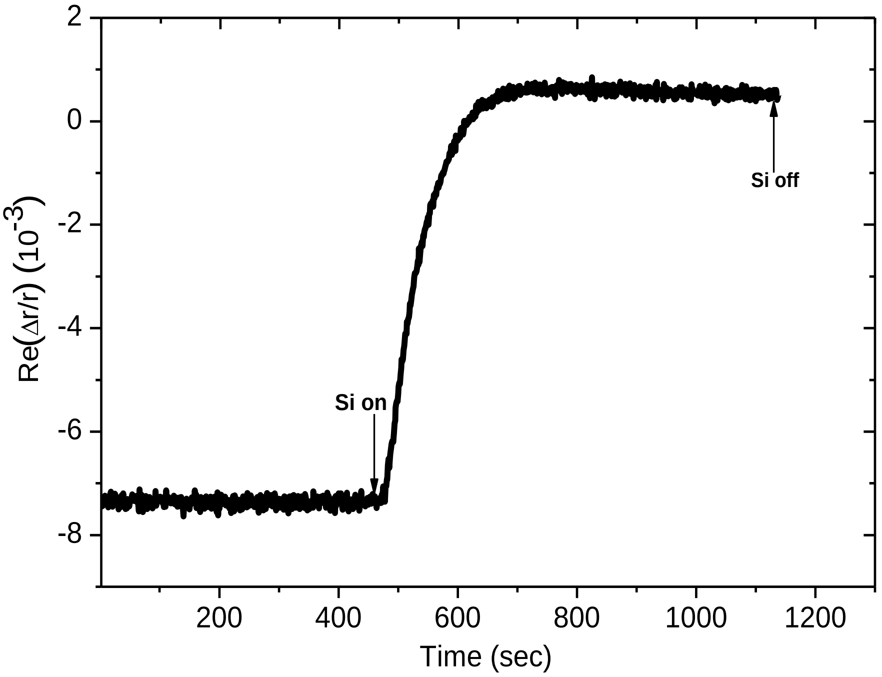

Figure 6.3 RAS transient at 1.9 eV during Si deposition (~0.6ML) on Si(111)-4×1-In at RT, where $\Delta r = r_{11} - r_{\perp}$.

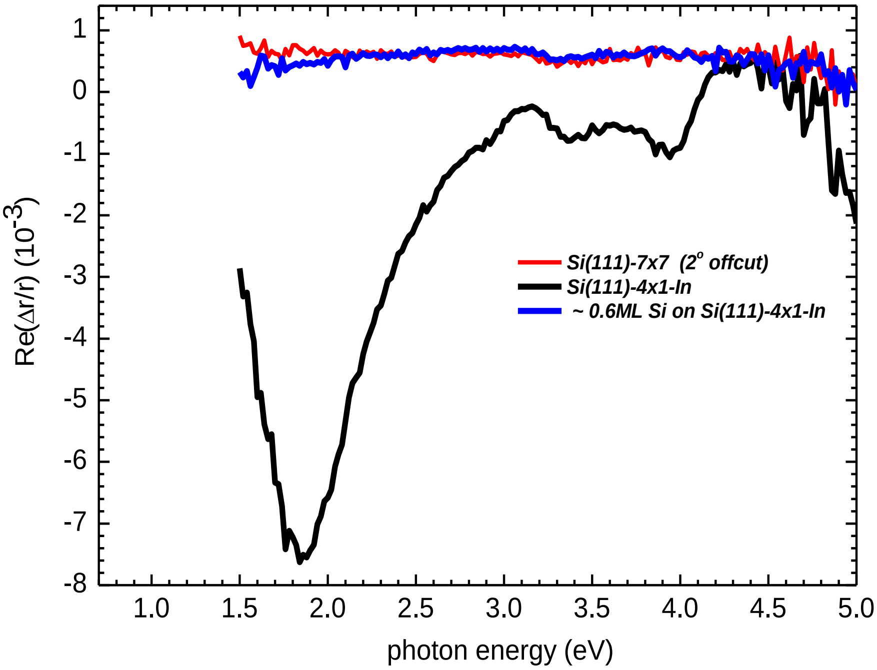

Figure 6.4 RAS of clean Si(111)-7×7, 2° offcut sample, Si(111)-4×1-In (black line) and Si(111)-4×1-In-(0.6 ML a-Si), where $\Delta r = r_{11} - r_{\perp}$.

at 1.9 eV quenches rapidly during the Si deposition. Figure 6.4 shows the RAS of Si(111)-4×1-In-(a-Si). LEED showed a diffuse pattern consistent with the amorphous growth of Si at RT. It is clear from the figure that RAS is a sensitive probe of the buried Si(111)/In interface, and that depositing a-Si at RT disrupts the Si(111)-4×1-In.

AES and LEED studies of a-Si capping of Si(111)/B, Si(111)/Al revealed that only Si(111)-$\sqrt{3}\times\sqrt{3}$-B, the Si(111)-Al "γ-phase", and Si(111)α7×7-Al appeared to preserve their ordered structures at a buried interface, while other reconstructions were disrupted by deposition of 0.2-0.4 ML of a-Si [18]. RT deposition of a-Si on Si(111)-$\sqrt{3}\times\sqrt{3}$-Ga also appears to disrupt the reconstruction. [19]. It was decided that it was unlikely that varying sample temperature and deposition rates would lead to successful capping by a-Si, and that the Si(111)/Ag system was more interesting.

Capping the In islands, with a-Si had a similar effect, removing the large positive peak below 1.8 eV (figure 6.2).

6.5 Ag nanostructures

6.5.1 RAS and STM results from Ag nanodots on Si(111)-3×1-Ag

The formation of Si(111)/Ag interfaces has been the subject of quite large number of studies. The lattice mismatch between Ag and Si crystals amounts to 25%, and the resulting interface energy is very large. The lattice strain and large interface energy greatly affect the Ag growth, eventually leading to formation of 3D islands with widely varying island density and size depending on the growth conditions. The high mobility of Ag atoms on the Si surface at RT is known to accelerate the 3D island growth. The growth mode and Ag morphology of Ag thin films on Si(111) substrates depend on the adsorbate termination of the surface [4, 7, 20]. Novel electronic structure-driven growth mechanisms have been proposed, in which the energy contribution of the quantized electrons confined in the metal overlayer affects the morphology of the growing film and prevails over the strain, surface and interface energies [9, 21].

It has been reported [22, 23] that Si(111)-3×1-Ag can act as a template for the growth of 1D arrays of Ag quantum dots, aligned along the <110> chain direction, at RT. The nanodots nucleate in the trenches between the Ag chains of the HCC structure (see section 5.3) and appear to be monodisperse. The dots are 1 nm in diameter by 0.15 nm in height and contain an estimated 19 ± 1 atoms [22, 23]. Above 0.5 ML Ag, the self-assembling nucleation of the nanodots breaks down and larger 3D islands start growing [23]. In the present work, the optical and electronic response of the Si(111)-3×1-Ag surface, and of nanodots and larger islands grown on this surface, have been studied with RAS (1°, 2° and 3° offcut towards $[\bar{1}\bar{1}2]$) and STM and STS (1° offcut).

STM measurements were taken by Dr. Sandhya Chandola at the Technische Universität Berlin, in an UHV chamber, equipped with an Omicron STM and low-energy electron diffraction (LEED) system. The vicinal Si(111) samples were n-type, phosphorous doped, with a resistivity in the range 0.1–20 Ω cm. Direct current heating of the sample produced a regular array of single height steps, with a sharp 7×7 LEED pattern forming after cooling. The preparation of (3×1)-Ag surface is described in section 5.3.1. Using the (3×1)-Ag surface as a template, an additional approximately 0.5 ML of Ag was deposited at RT to form 1D arrays of nanodots, aligned along the <110> chain direction. LEED showed that the single-domain 3×1 pattern was still preserved, but the spots were slightly diffuse. RAS measurements were also made in Berlin, and then repeated in Dublin. Very good reproducibility was found using the two different RAS instruments. The RAS structures between 1.4 and 3.9 eV showed significant attenuation and some modification (figure 6.5),

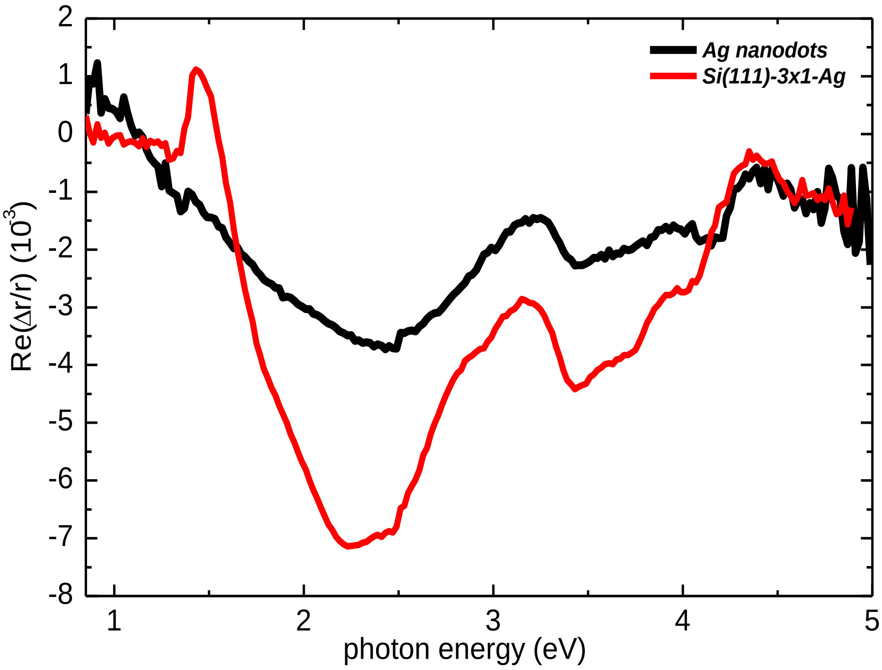

Figure 6.5 RAS of 0.5 ML (nanodots) of Ag on Si(111)-3×1-Ag surface offcut by 1° towards $[\bar{1}\bar{1}2]$,where $\Delta r = r_{11} - r_{\perp}$. RAS of (3×1)-Ag is shown for comparison.

and the IR RAS response only showed a very small positive anisotropy, increasing slightly towards lower energies.

The (3×1) surface is known to be semiconducting [24, 25], and the optical response is consistent with the absence of metallic character (see section 5.3.2). The lack of such a response from the nanodots is interesting. While it is possible that the nanodots, although aligned in chains (figure 6.6) and separated by only ~1.5 nm, produce a negligible anisotropic response because their shape is isotropic, it is more likely that the Ag nanodots are, in fact, non-metallic. In order to resolve this question, STS measurements were conducted on Si(111)-3×1-Ag and nanodots. All STS spectra were averaged over several individual spectra taken along relevant structures to improve the signal-to-noise ratio. The tip was also scanned between the dots parallel and perpendicular to the linear arrays to see if there was any difference in the tunnelling spectra. Tunnelling spectra from the (3×1)-Ag surface and the nanodots, are shown in figure 6.7(a). STS on the (3×1) surface showed a bandgap of ~1.1 eV, clearly indicating the semiconducting state of this surface. STS on the nanodot surface, however, also reveals a small bandgap of ~0.6 eV, indicating non-metallic character, consistent with the absence of a Drude tail in the optical spectra. STS measurements between two nanodots in the same line, and between two nanodots in

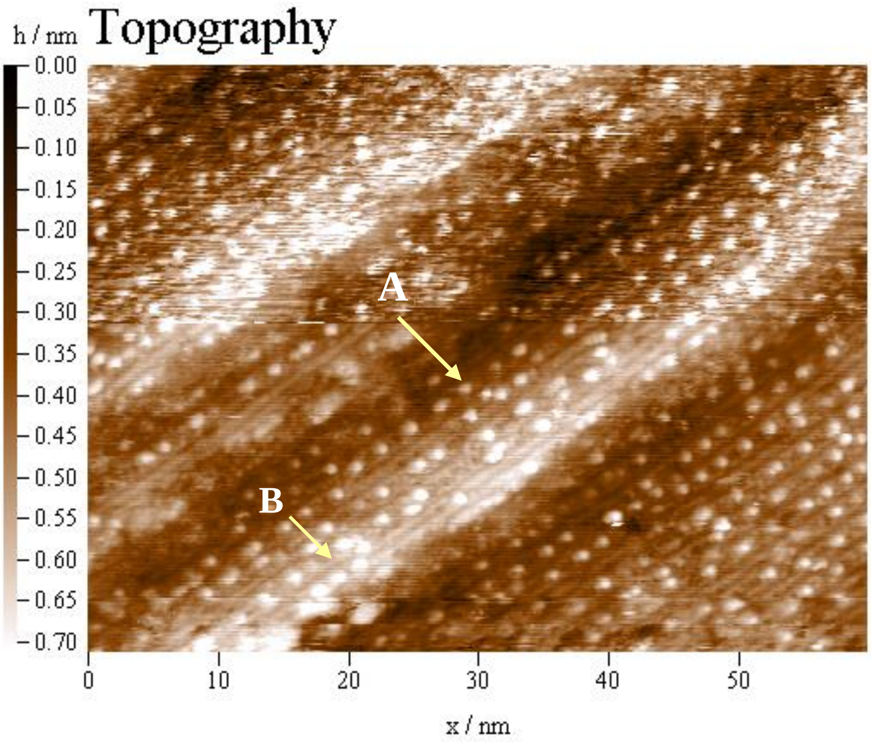

Figure 6.6 STM image of nanodots, 0.2 nm in height, grown on the Si(111)–3×1-Ag surface. An example of a nanodot is shown at A. An area of reconstructed (3×1) surface is shown at B. STS scans of these areas are shown in figure 6.7.

adjacent lines, showed a small anisotropy, with the inter-dot bandgap of the former being smaller by about 0.2 eV (figure 6.7(b)).

The electronic properties of metallic nanoclusters grown on substrates depend on the metal, the size and shape of the cluster, and the substrate. When the size of a cluster is less than a few nanometres, the average spacing of successive quantum levels, δ, (the Kubo gap [26], is given by $\delta = 4E_f/3n$, where E_f is the Fermi energy of the bulk metal and n is the number of valence electrons in the cluster [27]. Thus, for the Ag nanodots containing about 19 atoms [23], with $E_f = 5.49$ eV and $n = 19$, the value of δ would be 0.4 eV. This size-induced metal–insulator transition (figure 6.8 [28]) in nanoclusters has been observed, using STS, for several metals, such as Au, Pd, Ni and Ag, on a variety of substrates [27, 29]. Clusters of less than 2 nm diameter tend to be 2D and non-metallic, and there is evidence that metallicity develops in larger nanoclusters as the particles become 3D in character [29]. Where the nanoclusters are not isolated, however, there is evidence that lateral interactions between clusters can induce metallic behaviour. Strong quantum interactions can be observed when the interparticle separations in ordered monolayers become less than ~1 nm [30]. In an STS study of Ag nanoclusters on Si(100), it was found that the lateral conduction between neighbouring Ag clusters contributed significantly to the I–V characteristics via coupling through the substrate [31]. A study of coupling interactions as a function of inter-particle separation, using a monolayer of organically functionalized Ag nanoclusters, found that a metal-insulator transition occurred when $D/2r < 1.2$, where D is the distance between the centres of adjacent dots and $2r$ is the diameter of the dot [32]. The nanodots (figure 6.6) self-assemble such that, on average, $D/2r \sim 2.2$–3.2 [23] and thus the nanodots are not sufficiently close for lateral conduction to render them metallic. This is consistent with the absence of metallic character in RAS signal. There is another, albeit remote, possibility that should be considered. STM does not reveal atomic character directly, and STS is extremely surface sensitive. It is possible that the nanodots are Si adatoms, displaced by Ag atoms that embed in the surface beneath the dots, and that the embedded Ag cluster is metallic but not probed by STS. The displacement of Si atoms by Au to produce Si adatoms has been observed previously on Si(111) surfaces [33], but the displacement mainly produces isolated adatoms. Other LD systems grown on Si have not shown this behaviour [33], making the displacement of Si in

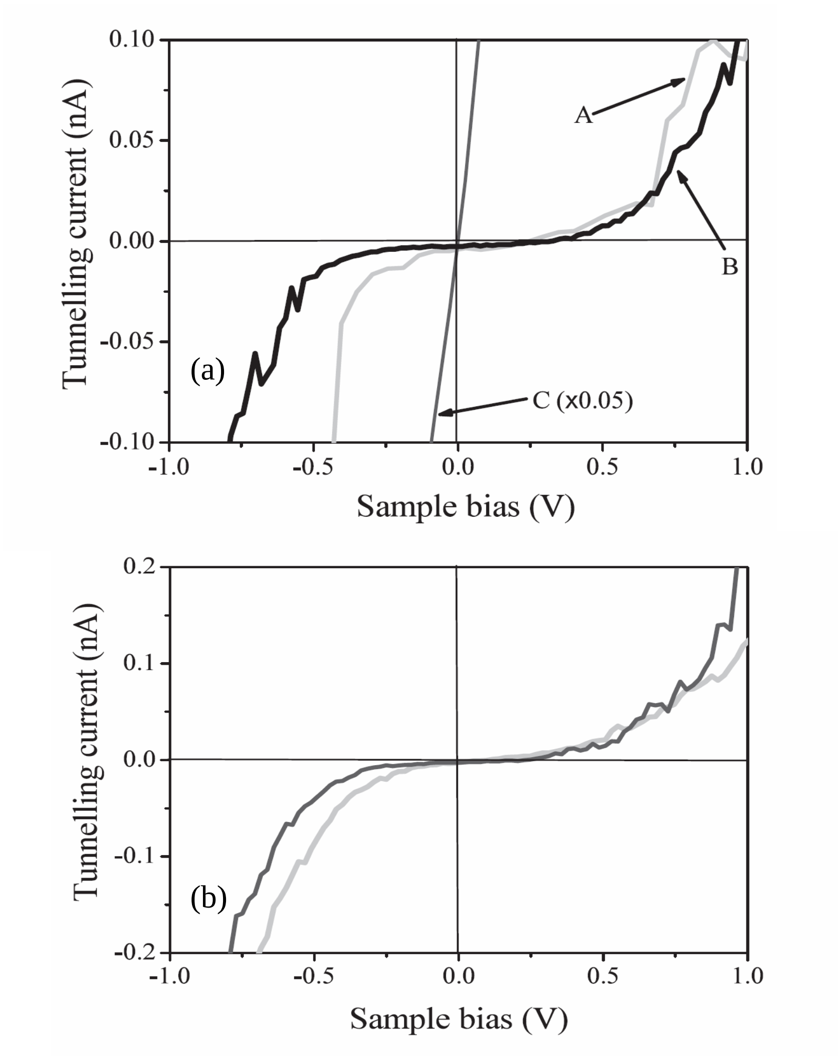

Figure 6.7 (a) STS spectra of the nanodots (A), the (3 ×1)-Ag surface (B) (b) STS spectra taken between two nanodots in the same line (thick grey line) and between two nanodots in adjacent lines (thick black line).

19 atom patches highly unlikely. It is important to note that the larger sampling depth of the RAS technique would detect the Drude signature of such embedded, aligned metallic Ag clusters, assuming the optical response was anisotropic. Care is required in interpretation, however, as an optically isotropic Drude tail of a buried metallic cluster would not be detected by RAS.

Finally, it has been suggested that the remarkably uniform 2D clusters form because a hexagonal Ag(111) packing arrangement with 19 Ag atoms just fit between neighbouring Ag channels of the HCC structure of the Si(111)–3×1-Ag surface [23]. It is not clear, however, why the nanodots do not elongate along the channels by adding further Ag atoms. For unsupported clusters of around this size, the formation of super-atom spherical

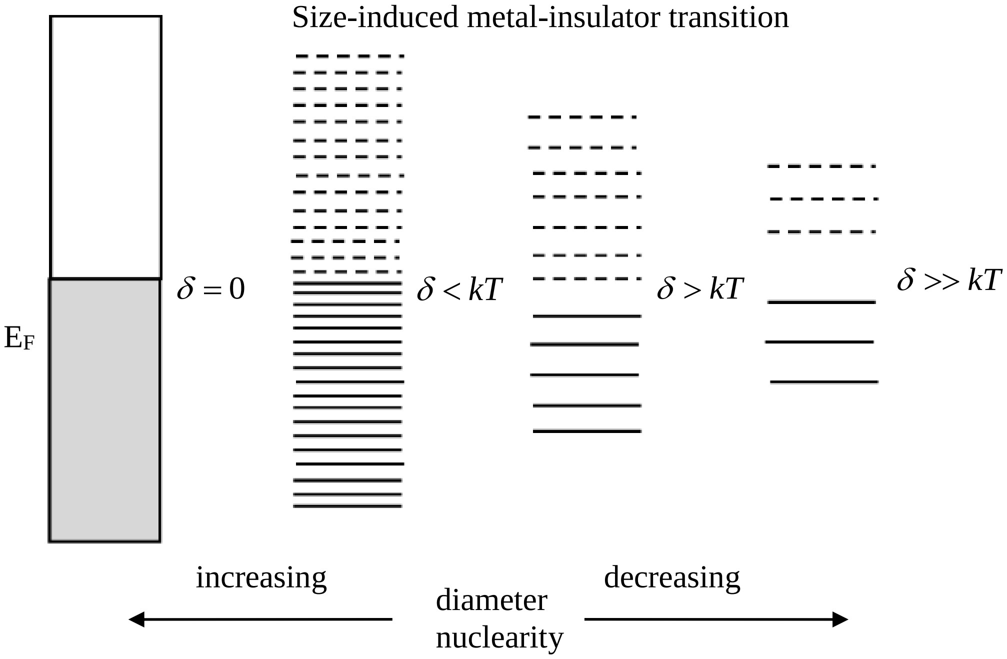

Figure 6.8 Evolution of band gap and the density of states as the number of atoms in a system increases (from right to left). δ is the so-called Kubo gap [28]

clusters of 8, 20 and 40 atoms is favoured for monovalent atoms, because of the additional stability associated with closed quantum shells arising from surface quantization, and such super-atom clusters have been observed experimentally [34]. Interaction with the underlying (3×1)-Ag surface clearly modifies this behaviour, because only 2D nanodots form at this coverage. It thus appears unlikely that super-atom considerations influence the cluster size, although this may be possible if the surface interactions are particularly finely balanced in this system.

6.5.2 RAS and STM results from Ag islands on Si(111)-3×1-Ag

Larger Ag islands were formed by further deposition of ~2 ML or more of Ag at RT, in order to determine the RAS response in the coverage regime where larger Ag islands are formed. Figure 6.9 shows the RAS spectra of islands on the 1^o offcut sample, for various Ag coverages. Figure 6.10 shows the STM image of ~2 ML Ag deposit on a 1^o offcut sample. STM measurements show that isolated, elongated Ag islands, of height ~1.5 nm, have been formed, with their long axes aligned in the direction of the step edges. This is consistent with the previous work, which showed that 2D dots changed their shape to three-dimensional, when their size exceeded the width between Ag channels [23]. In contrast to nanodots, the Ag islands the STS showed an unambiguous metallic behaviour, with a straight line through the zero point (figure 6.11, C).

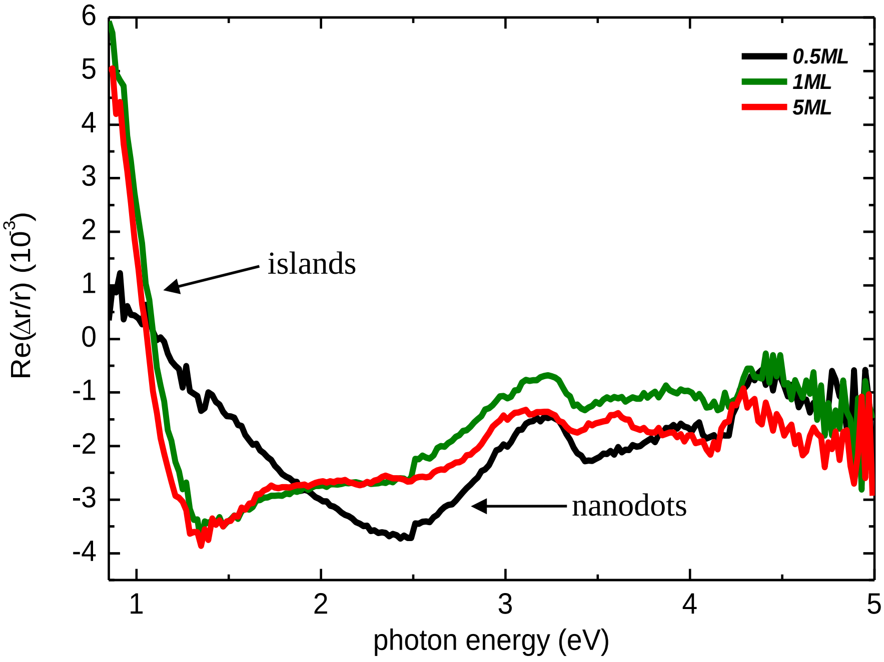

Figure 6.9 RAS spectra of Ag deposited on the single domain Si(111)-3×1-Ag surface offcut by 1° towards [$\bar{1}\,\bar{1}\,2$], where $\Delta r = r_{11} - r_{\perp}$.

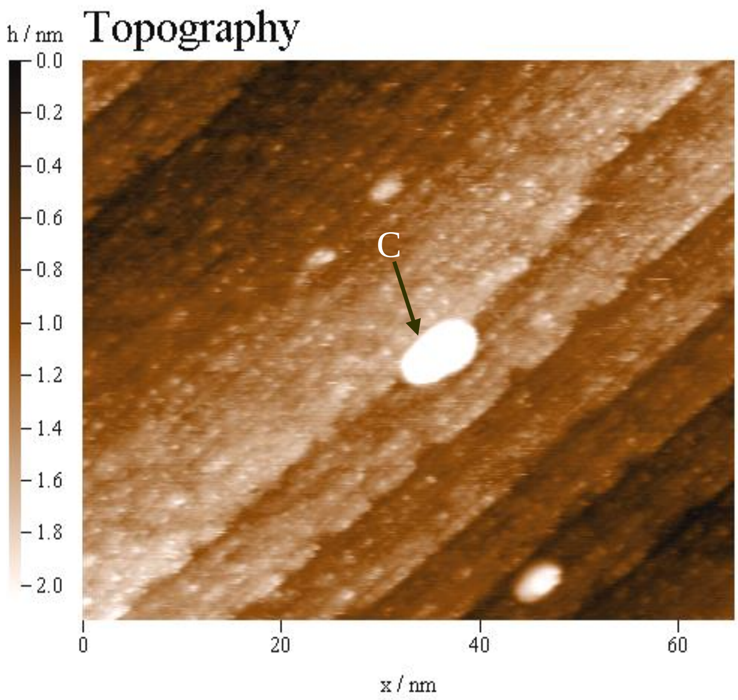

Figure 6.10 STM image of an elongated 3D Ag island (C), 1.5 nm in height, with its long axis aligned along the steps. The sample bias voltage was 1.1 V and the tunnelling current was 0.2 nA.

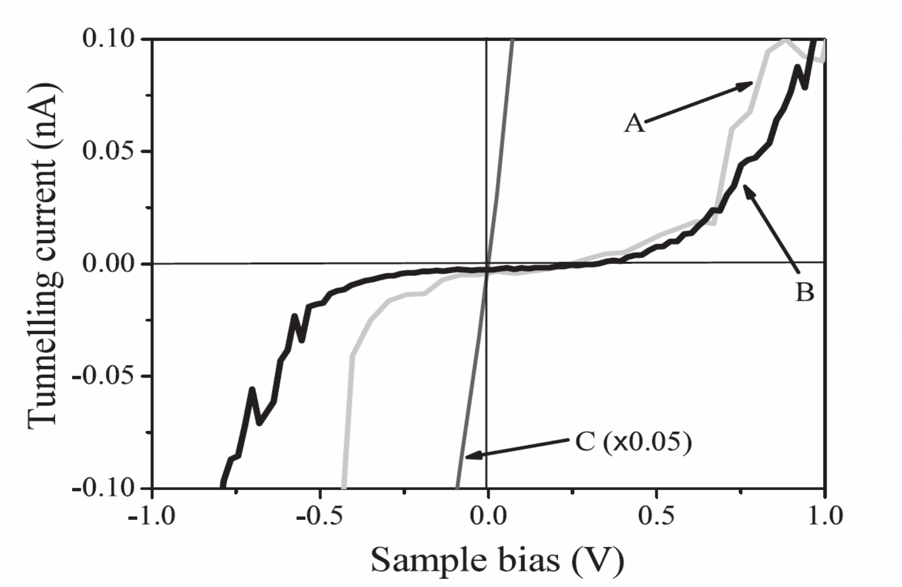

Figure 6.11 STS spectra of 3D Ag islands (C), with change of scale. STS of nanodots (A) and 3×1-Ag (B) surface are shown for comparison

There are a number of factors that may contribute to anisotropic island growth. Strain anisotropy can provide thermodynamic reasons for elongated islands to grow. This has been shown in the case of Si/Si(100)-2×1 [35]. Channeled low index substrates such as fcc(110) or bcc(211) surfaces [36], have anisotropic potential energy surfaces that provide kinetic reasons for anisotropic growth. There may also be a critical size, controlled by competition between isotropic surface energies and anisotropic strain energies, below which an island adopts an isotropic shape and above which it adopts an anisotropic shape [37]. The combination of electronic effects, due to QSE and strain anisotropy can also influence island morphology, as shown in the case of Pb on Si(111)-(4×1)-In [38].

Regarding the IR response in figure 6.9, large positive RA signals at lower energies have been observed in the case of other metal nanowires. This is due to the anisotropic quasi-free conduction electron response [14, 39, 40]. As the IR reflectance anisotropy of a 1D metallic system can be related to the Drude free-electron contribution [41], it can be shown that the RAS signal is proportional to the conductivity difference. The dielectric function is related to the optical conductivity, σ [42],

$$\varepsilon = 1 - i\sigma / \varepsilon_0 \omega \tag{6.1}$$

The RAS signal can be described in terms of conductivity anisotropy, $\Delta\sigma = \sigma_{xx} - \sigma_{yy}$, by using this relation and the three layer model of the RAS signal from equation (3.5)

$$\frac{\Delta r}{r} = \frac{2d}{\varepsilon_0 c} \frac{\Delta\sigma}{\varepsilon_b - 1} \qquad (6.2)$$

Hence the RAS signal is directly proportional to this conductivity difference. Analogously to the SDA (section 3.3.1), the RAS spectrum allows $d\Delta\sigma$, to the anisotropy in the sheet conductance, to be determined [14].

For bulk Ag, where there are no significant bulk interband optical transitions below ~3 eV, the Drude contribution becomes significant below about 1 eV ([43], and references therein). The large positive IR response at higher coverages, with the dominant polarizability along $[1\bar{1}0]$, parallel to the step edges and in the direction of the long axes of the islands, is in the spectral region where anisotropic Drude-like intraband transitions begin to make a significant contribution to the optical spectrum. The simplest explanation for the optical response being sensitive to the shape of the islands is that the inelastic scattering mean free path (mfp) of conduction electrons in bulk Ag at RT is ~60 nm [32], resulting in the mfp of the optically excited conduction electrons being determined by much smaller island dimensions. A simple anisotropic Drude model with scattering lengths determined by the dimension of these nanoscale islands is sufficient to produce the positive anisotropy in the response that is observed [14].

6.5.3 Offcut dependence

The RAS spectra at 0.5 ML coverage (figure 6.12) (nanodots) are essentially the same for all offcuts, and show no metallic signature. Very similar amplitudes of these spectra show the very good reproducibility of the surface preparation techniques that result in the single domain structure. It is also clear that the step contribution is limited to the region around bulk critical points (section 5.4.3). Figure 6.13(a) shows the RAS spectra of 0.5–6 ML Ag coverage on the Si(111)-3×1-Ag surface for 1^{o}, 2^{o} and 3^{o} offcut samples, and figure 6.13(b) shows the RAS transient of the additional Ag deposit on a 3^{o} offcut sample. The RAS transient shows a clear change around the region of transition from nanodots to the onset of islands. At 1 ML coverage (islands), there is only a small increase in the RAS signal with offcut angle. Interestingly, deposition of up to 6 ML of Ag on the 1° offcut surface does not change the measured anisotropy significantly. For the higher offcuts, however, figure 6.13(a) shows a dramatic change, with a strong IR response saturating around 4 ML and 6 ML Ag coverage for the 2° and 3° samples, respectively. All spectra are dominated by a minimum around 1.1-1.4 eV, with higher Ag coverages producing an

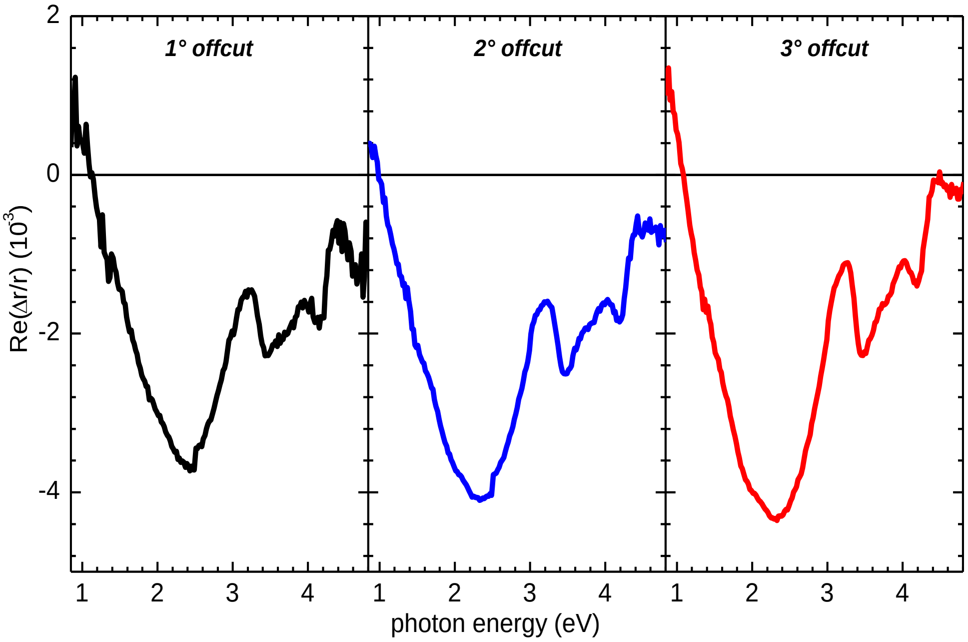

Figure 6.12 RAS of 0.5 ML of Ag on Si(111)-3×1-Ag surface (a) 1^{o} (b) 2^{o} and (c)3^{o} offcut towards [$\bar{1}\,\bar{1}\,2$], where $\Delta r = r_{11} - r_{\perp}$.

apparent red shift and increase in amplitude of the minimum. Further increase in Ag coverage does not lead to a significant increase in the optical anisotropy.

The spectra are consistent with the model based on diffusion-limited island formation discussed in detail in section 2.3.3. Arriving adatoms make random walks on the terraces and, when meeting each other, form islands. All islands larger than critical nucleus will grow by further addition of adatoms from the 2D lattice gas. Nucleation and growth are competing processes, because an arriving adatom can either form a new island with another free adatom (nucleation) or walk into an existing island (growth). The diffusion coefficient of the adatoms determine how large an area, i.e how many distinct sites, an adatom interrogates in unit time. Therefore, the diffusion coefficient determines the outcome of the competition between nucleation and growth, and hence determines the number density of stable islands after deposition to a certain dose at a given deposition rate [44]. A large diffusion coefficient means a high probability for an arriving adatom to find an existing island before another adatom is deposited in its vicinity to provide a chance for nucleation, yielding a lower number density of islands after deposition. With island growth

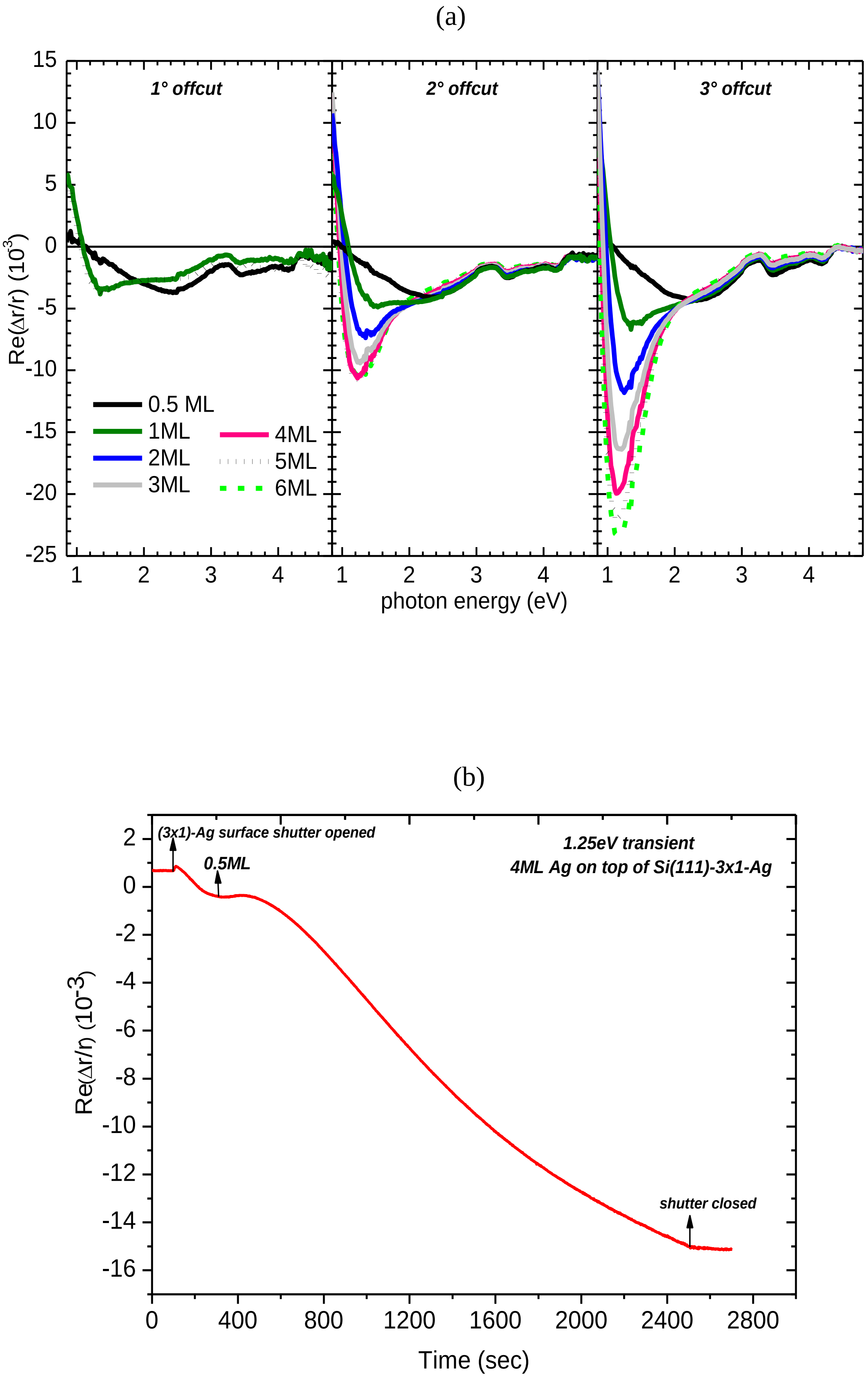

Figure 6.13 (a) RAS spectra of Ag deposit on the single domain Si(111)-3×1-Ag surface. (b) Transient of additional Ag deposition (up to 4 ML) on the 3° Si(111)-3×1-Ag surface, where $\Delta r = r_{11} - r_{\perp}$

on the terraces of a vicinal surface, terrace width, *L* appears also as a length scale. If *L* is much larger than nucleation length, l_n, growth proceeds as on a singular surface. On a terrace with smaller *L* most adatoms attach to the step edge and only few islands appear.

For the 1° offcut, the RAS results are consistent with the assumption that the average terrace width (18 nm, for single height steps) is significantly larger than the diffusion length of Ag at RT, leading to nucleation of Ag islands on the terrace as well as at the steps. The slightly elongated islands (figure 6.10) indicate only a small anisotropy in the diffusion coefficients or the strain. The similarity of the RAS spectra for coverages up to 6 ML shows that the morphology of these islands does not change significantly with coverage for the 1^o offcut. The 2^o offcut behaves quite differently (figure 6.13(a)). If the Ag diffusion length is greater than 9 nm (the average terrace width for the 2° offcut sample), step-nucleated islands are likely to be dominant. More elongated islands might be expected to form preferentially along the step edges, leading to the larger IR RAS signal. The 3° offcut has 50% more step length than the 2° offcut sample, giving a larger RAS response that should saturate at 50% higher coverage as, indeed, is observed in figure 6.13(a). STM measurements are planned on the 2° and 3° samples to probe the morphology of islands, particularly in the region of steps.

Previous work has shown that anisotropic islands can be grown on stepped surfaces. Uniform long arrays of CaF_2 and of Au-(5×2), islands adsorbed along steps have been prepared on stepped Si(111)-7×7 [45]. The very different RAS spectra for the 2° and 3° samples suggest that such anisotropic islands are now being formed, similar to those found in the Pb/Si(335) system, where an even larger optical anisotropy has been observed in the IR [7, 39] by direct subtraction of reflectance parallel and perpendicular to the long axes of the islands. The large optical anisotropy [39] has been attributed to the morphological anisotropy, which arises from the presence of the perfectly aligned nanowires. It has been suggested that, when the electric field vector is aligned parallel to the steps, the IR radiation induces AC currents along the nanowire which act like antennae.

Modelling of the RAS spectrum of the 2 ML Ag sample has been attempted by calculating the normal incidence reflectance for two non-interacting multilayer stacks, differing only in the dielectric function for the anisotropic layer (section 2.4.1). The discrepancy above 3 eV, in the region of the bulk critical points of Si, is probably caused by strain in the near-surface region [46]. The model assumes that the nanostructure signature originates from an effective anisotropy in the free electron response, with a significant deviation from an ideal Drude-like response being included by the addition of an anharmonic oscillator. This deviation might originate from electronic interactions with the substrate or percolation effects which are not included in the modelling. The software used was Lay_Tex 2.0, written by Dr. J.-Th. Zettler and database values for the isotropic bulk dielectric function for Si were used [47]. It was found possible to reproduce the response below 3 eV by adjusting 4 parameters, by a combined Drude like dielectric function in the *x* direction and an oscillator in the *y* direction, as set out in table 6.1. The measured RAS line shape (figure 6.14(a)) can be easily reproduced, when the (3×1)-Ag contribution (figure 6.14(b)) is included. This simple model of non-interacting layers may work here because only a relatively small proportion of the (3×1)-Ag surface is covered by Ag islands. No significance should be attached to the particular parameter values of table 6.1, however. The main use of the model is to explore the changes observed on capping, discussed in the next section.

Table 6.1 Numerical values for least square fits of figures 6.14 and 6.16

	Oscillator Parameters			Drude parameters	Comment
	$A_y\,(\mathrm{eV})^2$	ω_{0y} (eV)	Γ_y (eV)	Γ_x (eV)	
(3×1) contribution	13	2.44	1.9	-	d = 1 nm (fixed)
Ag islands (2 ML)	34 ± 1	1.2 ± 0.03	1.13 ± 0.05	1 ± 0.2	ω_p (7.3eV) fixed

6.5.4 RAS results of Si capped Ag nanostructures

Model nanostructures have been formed by deposition of Ag onto the Si(111)-3×1-Ag, as described in section 6.5.2. The Ag structures were then capped with Si using a high purity sublimation source, as described in section 4.2.3. The thickness of the a-Si was 6 nm, measured *ex situ* using variable angle spectroscopic ellipsometery. Samples were kept near RT during this step to avoid annealing the Ag nanostructures. The Si layers are expected to be amorphous under these conditions [48, 49], and LEED showed only a diffuse background. AES scan of the capped surface showed no detectable surface segregation of Ag. The RAS spectra of the samples were measured after depositing the cap, first in situ and then after exposure to ambient conditions. In Figure 6.15, RAS spectra are shown

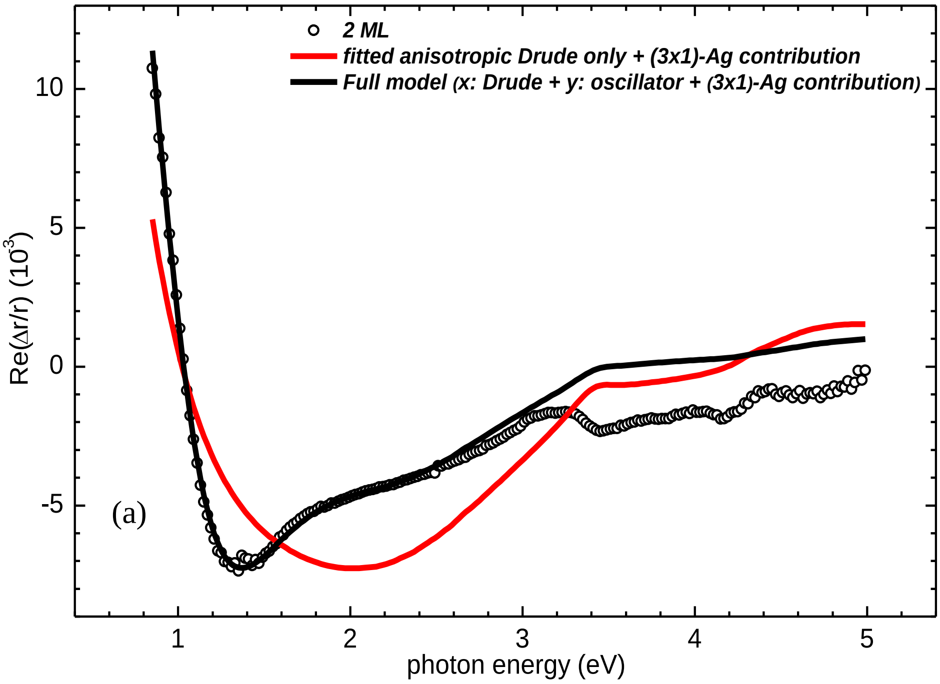

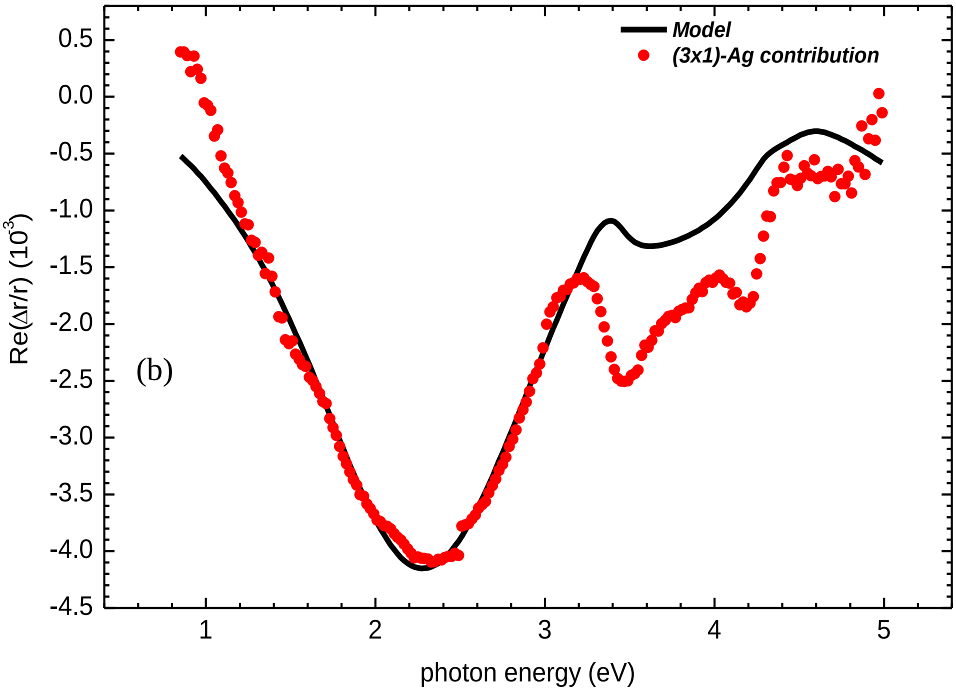

Figure 6.14 (a) Modelled RAS spectra for an additional 2 ML Ag. The RAS spectra include a contribution derived from the 0.5 ML spectrum (b) and a combination of a free - electron response in the *x* – direction and an oscillator in the *y*- direction. (b) Modelled 0.5 ML spectrum ((3×1)-Ag contribution)

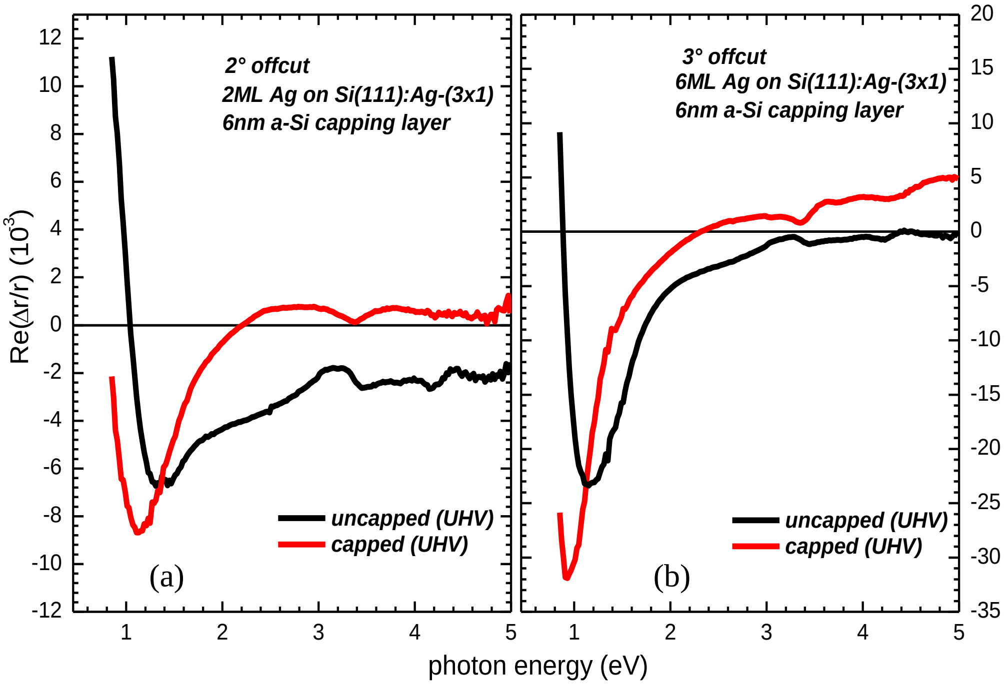

Figure 6.15 RAS spectra of 2 ML (6ML) Ag on the Si(111)-3×1-Ag surface with (a) 2° (b) 3° offcut, before (black lines) and after (red lines) capping with ~6nm a-Si.

before and after capping. It can be seen that capping does not destroy the RAS spectrum, in contrast to the Si(111)/In system. The major effect observed are a red shift and narrowing of the main peak, and a reduction in structure in the 2-3 eV region where any (3×1)-Ag contribution would occur. Details of the modelling of the RAS spectra of Ag islands are given in the previous section. Database values for the isotropic dielectric function for Si and a-Si were used [47], Figure 6.16 compares the model results with the RAS data for the uncapped and capped 2° offcut sample with 2 ML additional Ag. The figures show that agreement is significantly improved if the contribution of the (3×1) areas is removed. The simple modelling used here supports the conclusion that the metallic nanostructures survive the capping, while the (3×1) areas are modified by Si deposition. However, it can be seen that the modelling does not account for the red shift in the main peak observed upon capping. It is clear that the simple non-interacting multilayer model cannot explain this red shift. Red shift has been observed in surface plasmon resonances in larger scale Ag films, where a dielectric coating has been introduced that varies the inter-island dielectric function [12, 13]. In another study, it was concluded that the main origin of the plasmon shift (~1.5 eV) is the high refractive index of the a-Si matrix, in addition to the shift introduced by shape anisotropy (~0.3 eV) and coupling effects (~1 eV) [12]. Surface

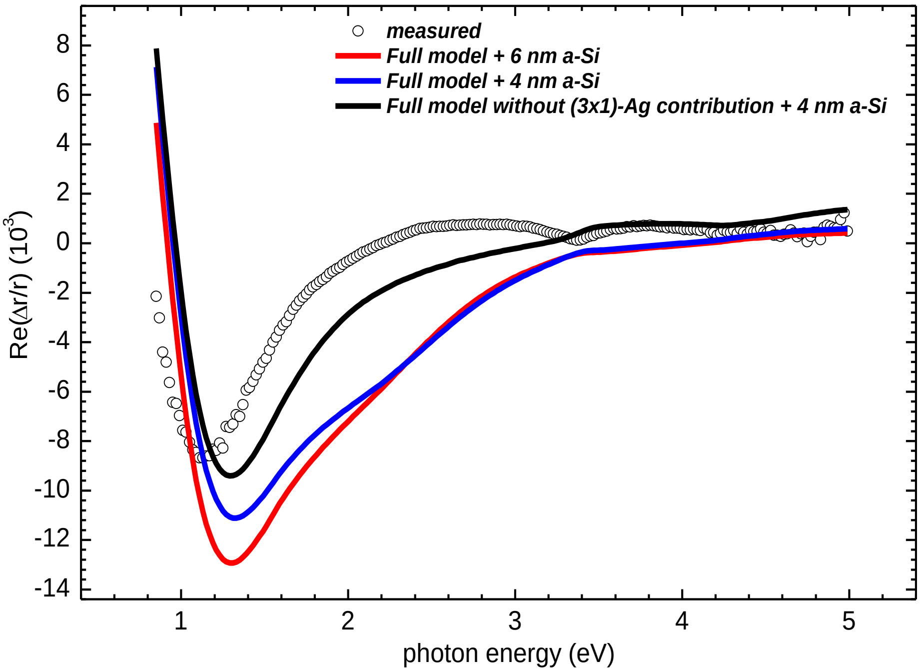

Figure 6.16 Modelled RAS spectra for an additional 2 ML Ag, after capping. The line shape of the capped structures cannot be explained by adding the capping layer alone (blue thick line), but reasonable agreement is reached if the contribution from the (3×1) area is excluded, indicating that the nanostructures survive the capping, while the (3×1) area is modified.

plasmon resonance in the near-infrared (0.9 eV), with tails extending below 0.5 eV, has been reported for two- dimensional arrays of silver nanoparticles embedded in amorphous silicon, fabricated by sequential Si/Ag/Si electron-beam evaporation [11] . The Ag nanoparticles were positioned in the center of a 14 nm-thick *a*-Si layer. Samples with Ag exhibited absorptance, mainly at energies below 2.5 eV, which is attributed to the surface plasmon absorption by the Ag nanoparticles. The absorptance was found to increase in magnitude and shifted towards lower energies with increasing Ag content. It was concluded that the large redshift was mainly due to the high refractive index of the matrix, with shape anisotropy and interparticle coupling [11]. Due to the lack of information about the size distribution and inter-island distance, this type of model could not be applied here. However, it appears likely that the origin of the large red shift may be due to the introduction of high refractive index a-Si. More advanced models are clearly needed in order fully model the capped nanostructures.

6.5.5 Long term stability of capped Ag nanostructures

The samples were re-measured *ex situ* after one, and then two, months to test the long term stability of the protected Ag layers, using an extended spectral range RA spectrometer at the Technische Universität Berlin. The RAS apparatus is unusual in having an energy range down to 0.5 eV The IR–vis RAS instrument utilizes MgF2 polarizers, a CaF2 photoelastic modulator, and a double-grating monochromator. Three detectors are used: a liquid nitrogen cooled InAs detector for measurements between 0.45 and 0.9 eV, an InGaAs photodiode for 0.75–1.5 eV, and a Si photodiode for measurements above 1.3 eV. Figure 6.17 shows the RAS of the capped samples after up to two months exposure to air.

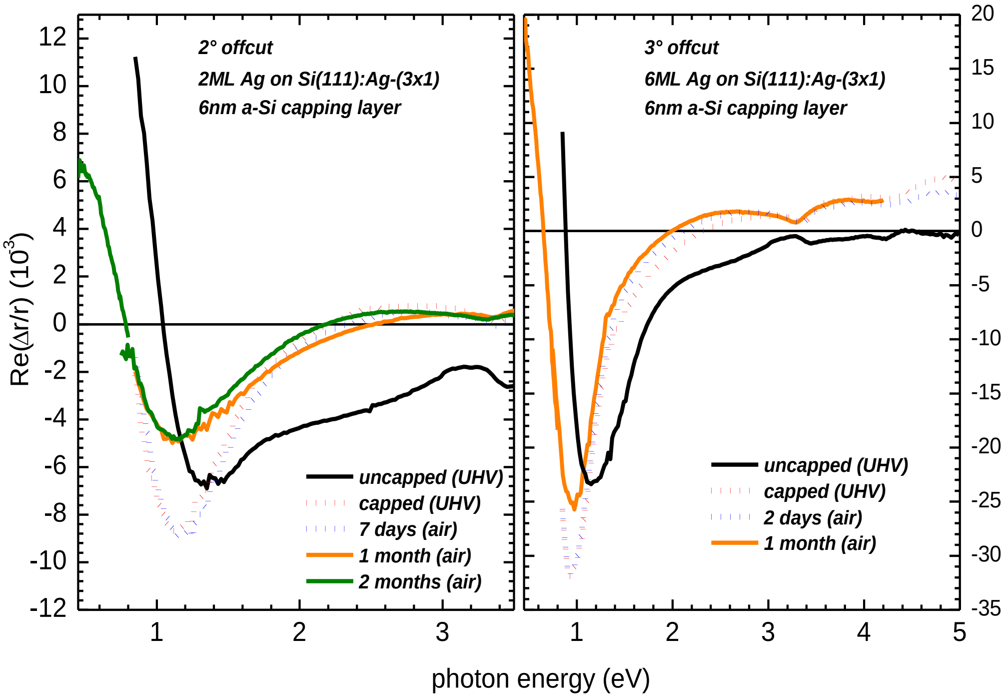

Figure 6.17 RAS spectra of 2 ML (6ML) Ag on the Si(111)-3×1-Ag surface with 2° (3°) offcut, before (black lines) and after (red dotted) capping with ~6 nm a-Si. The RAS of the capped structures remains stable for at least a week after exposure to ambient conditions (blue dotted), but degrades significantly within the first month (orange line)

A significant change has occurred, indicating that the 6 nm a-Si capping layer may not be providing complete long term protection. It is also possible that a slow relaxation process is occurring in the region of the nanostructures, but this is less likely. Finally, the results of this chapter show that extension of the IR response of the RAS spectrometer to below 0.5 eV would provide significant additional information on LD metallic nanostructures.

References

1. Narusawa T, Kinoshita K, Gibson WM, Hiraki A: **Structure study of Au-Si interface by MeV ion scattering.** *Journal of Vacuum Science and Technology* 1981, **18:**872-875.
2. Zhang Z, Niu Q, Shih C-K: **"Electronic Growth" of Metallic Overlayers on Semiconductor Substrates.** *Physical Review Letters* 1998, **80:**5381.

3. Yu H, Jiang CS, Shih CK, Ebert P: **Effect of the Si substrate structure on the growth of two-dimensional thin Ag films.** *Surface Science* 2002, **518:**63-71.
4. Roos KR, Roos KL, Horn-Von Hoegen M, Meyer Zu Heringdorf FJ: **High temperature self-assembly of Ag nanowires on vicinal Si(001).** *Journal of Physics Condensed Matter* 2005, **17:**1407-1414.
5. Tersoff J, Tromp RM: **Shape transition in growth of strained island. Spontaneous formation of quantum wires.** *Physical Review Letters* 1993, **70:**2782.
6. Jalochowski M, Bauer E: **Growth of metallic nanowires on anisotropic Si substrates: Pb on vicinal Si(0 0 1), Si(7 5 5), Si(5 3 3), and Si(1 1 0).** *Surface Science* 2001, **480:**109-117.
7. Jalochowski M, Bauer E: **Self-assembled parallel mesoscopic Pb-wires on Au-modified Si(5 3 3) substrates.** *Progress in Surface Science* 2001, **67:**79-97.
8. Ryjkov S, Lifshits VG, Hasegawa S: **Epitaxial growth of Ag on Si(111)-4*1-In surface studied by RHEED, STM, and electrical resistance measurements.** *e-Journal of Surface Science and Nanotechnology* 2003, **1**.
9. Nagamura N, Matsuda I, Miyata N, Hirahara T, Hasegawa S, Uchihashi T: **Quasi-one-dimensional quantized states in an epitaxial Ag film on a one-dimensional surface superstructure.** *Physical Review Letters* 2006, **96:**256801.
10. McGilp JF: **Optical response of low-dimensional In nanostructures grown by self-assembly on Si surfaces.** *Physica Status Solidi a-Applied Research* 2001, **188:**1361-1369.
11. Mertens H, Verhoeven J, Polman A, Tichelaar FD: **Infrared surface plasmons in two-dimensional silver nanoparticle arrays in silicon.** *Applied Physics Letters* 2004, **85:**1317-1319.
12. Jensen TR, Duval Malinsky M, Haynes CL, Van Duyne RP: **Nanosphere lithography: tunable localized surface plasmon resonance spectra of silver nanoparticles.** *Journal of Physical Chemistry B* 2000, **104:**10549-10556.
13. Xu G, Tazawa M, Jin P, Nakao S, Yoshimura K: **Wavelength tuning of surface plasmon resonance using dielectric layers on silver island films.** *Applied Physics Letters* 2003, **82:**3811-3813.
14. Fleischer K, Chandola S, Herrmann T, Esser N, Richter W, McGilp JF: **Free-electron response in reflectance anisotropy spectra.** *Physical Review B (Condensed Matter and Materials Physics)* 2006, **74:**195432-195410.
15. Nogami J, Park S, Quate CF: **Indium-induced reconstructions of the Si(111) surface studied by scanning tunneling microscopy.** *Physical Review B (Condensed Matter)* 1987, **36:**6221-6224.
16. Ofner H, Surnev SL, Shapira Y, Netzer FP: **In overlayers on Si(111)7*7: growth and evolution of the electronic structure.** *Physical Review B-Condensed Matter* 1993, **48:**10940-10949.
17. Bekhtereva OV, Churusov BK, Lifshits VG: **Thin gold and indium films on Si(111) surface.** *Surface Science* 1992, **273:**449-452.
18. Zotov AV, Wittmann F, Lechner J, Eisele I, Ryzhkov SV, Lifshits VG: **Electrical properties of surface phases on silicon capped by amorphous Si layers.** *Applied Physics Letters* 1995, **67:**611.
19. Headrick RL, Feldman LC, Robinson IK: **Stability of boron- and gallium-induced surface structures on Si(111) during deposition and epitaxial growth of silicon.** *Applied Physics Letters* 1989, **55:**442-444.
20. Zhang ZH, Hasegawa S, Ino S: **RHEED intensity oscillation during epitaxial growth of Ag on Si(111) surfaces at low temperature.** *Physical Review B: Condensed Matter* 1997, **55:**9983.

21. Matsuda I, Han Woong Y, Tanikawa T, Tono K, Nagao T, Hasegawa S, Ohta T: **Growth and electron quantization of metastable silver films on Si(001).** *Physical Review B (Condensed Matter and Materials Physics)* 2001, **63:**125325-125321.
22. Kuntze J, Mugarza A, Ortega JE: **Ag-induced zero- and one-dimensional nanostructures on vicinal Si(111).** *Applied Physics Letters* 2002, **81:**2463-2465.
23. Hirayama H, Horie R, Takayanagi K: **Nucleation of Ag nanodots at the Si(111)3*1-Ag surfaces.** *Surface Science* 2001, **482-485:**1277-1282.
24. Gurnett M, Gustafsson JB, Magnusson KO, Widstrand SM, Johansson LSO: **Angle-resolved photoemission study of the single-domain Si(111)(3*1)/(6*1)-Ag surface.** *Physical Review B-Condensed Matter* 2002, **66:**161101-161101-161104.
25. Sakamoto K, Ashima H, Zhang HM, Uhrberg RIG: **Identification of the basic structure of the Ag/Si(111)-(6 *1) surface: Observation of a low-temperature c(12*2) phase.** *Physical Review B* 2001, **65:**045305.
26. Kubo R: **Electronic Properties of Metallic Fine Particles. I.** *Journal of the Physical Society of Japan* 1962, **17:**975-986.
27. Vinod CP, Kulkarni GU, Rao CNR: **Size-dependent changes in the electronic structure of metal clusters as investigated by scanning tunneling spectroscopy.** *Chemical Physics Letters* 1998, **289:**329-333.
28. Edwards PP, Johnston RL, Rao CNR: *Metal Clusters in Chemistry.* P. Braunstein, G. Oro, P.R. Raithby (eds.), Wiley-VCH, Weinheim; 1999.
29. Lai X, St. Clair TP, Valden M, Goodman DW: **Scanning tunneling microscopy studies of metal clusters supported on TiO2(110): morphology and electronic structure.** *Progress in Surface Science* 1998, **59:**25-52.
30. Collier CP, Saykally RJ, Shiang JJ, Henrichs SE, Heath JR: **Reversible tuning of silver quantum dot monolayers through the metal-insulator transition.** *Science* 1997, **277:**1978-1981.
31. Kang-Ho P, Mincheol S, Jeong Sook H, Wan Soo Y, Young-Jo K: **Fabrication of lateral single-electron tunneling structures by field-induced manipulation of Ag nanoclusters on a silicon surface.** *Applied Physics Letters* 1999, **75:**139-141.
32. Shiang JJ, Heath JR, Collier CP, Saykally RJ: **Cooperative phenomena in artificial solids made from silver quantum dots: the importance of classical coupling.** *Journal of Physical Chemistry B* 1998, **102:**3425-3430.
33. Kirakosian A, Crain JN, Lin J-L, McChesney JL, Petrovykh DY, Himpsel FJ, Bennewitz R: **Silicon adatoms on the Si(1 1 1)5*2-Au surface.** *Surface Science* 2003, **532-535:**928-933.
34. Ekardt W: **The super-atom model: link between the metal atom and the infinite metal.** *Zeitschrift fÃ¼r Physik B Condensed Matter* 1997, **103:**305-312.
35. Mo YW, Kleiner J, Webb MB, Lagally MG: **Activation energy for surface diffusion of Si on Si(001): A scanning-tunneling-microscopy study.** *Physical Review Letters* 1991, **66:**1998-2001.
36. Roder H, Hahn E, Brune H, Bucher J-P, Kern K: **Building one- and two-dimensional nanostructures by diffusion-controlled aggregation at surfaces.** *Nature* 1993, **366:**141-143.
37. Pradhan A, Ma NY, Liu F: **Theory of equilibrium shape of an anisotropically strained island: Thermodynamic limits for growth of nanowires.** *Physical Review B (Condensed Matter and Materials Physics)* 2004, **70:**193405-193404.
38. Hupalo M, Tringides MC: **Self-organization and geometry control of Pb islands grown on anisotropic substrates.** *Physical Review B (Condensed Matter and Materials Physics)* 2006, **73:**041405-041404.

39. Jalochowski M, Strozak M, Zdyb R: **Reflectance anisotropy during growth of Pb nanowires on well ordered Si(3 3 5) surface.** *Applied Surface Science* 2003, **211:**209-215.
40. Fleischer K: **Optical anisotropy and vibrational properties of Sn, In and Cs nanowires.** PhD thesis, Technischen Universitat 2005.
41. Bennett HE, Bennett JM: *Optical properties and electronic structure of metals and alloys.* ed F Abeles (Amsterdam:North-Holland) P 181; 1966.
42. McIntyre JDE, Aspnes DE: **Differential reflection spectroscopy of very thin surface films.** *Surface Science* 1971, **24:**417-434.
43. Fuster G, Tyler JM, Brener NE, Callaway J, Bagayoko D: **Electronic structure and related properties of silver.** *Physical Review B (Condensed Matter)* 1990, **42:**7322-7329.
44. Venables JA: **Rate equation approaches to thin film nucleation kinetics.** *Philosophical Magazine* 1973, **27:**697-738.
45. Himpsel FJ, Kirakosian A, Crain JN, Lin JL, Petrovykh DY: **Self-assembly of one-dimensional nanostructures at silicon surfaces.** *Solid State Communications* 2001, **117:**149-157.
46. Mantese L, Rossow U, Aspnes DE: **Surface-induced optical anisotropy of oxidized, clean, and hydrogenated vicinal Si(001) surfaces.** *Applied Surface Science* 1996, **107:**35-41.
47. Palik ED: *Handbook of Optical Constants of Solids.* New York: Academic Press; 1985.
48. Zotov AV, Kulakov MA, Bullemer B, Eisele I: **Scanning tunneling microscopy study of Si growth on a Si(111)sqrt[3]*sqrt[3]-B surface.** *Physical Review B* 1996, **53:**12902.
49. Jona F: **Study of early stages of epitaxy of silicon on silicon.** *Applied Physics Letters* 1966, **9:**235-237.

7

SHG of Ag induced reconstructions and nanostructures

7.1 Overview

SHG studies of Si(111)-3×1-Ag, Si(111)-$\sqrt{3}\times\sqrt{3}$-Ag, Ag nanodots and Ag islands under 800 nm laser excitation are presented and discussed in this chapter. The results are analyzed in terms of the structural models proposed for the various reconstructions.

7.2 SHG of Si(111)-In, -Au and -Ag systems – previous studies

The sensitivity of SHG to the surface symmetry has been useful in studying the symmetry of various metal induced reconstructions on Si(111). There have been number of SHG studies on (5×2)-Au and (4×1)-In on vicinal Si(111) surfaces [1-5]. It was shown that the single mirror plane character of the vicinal Si(111)-7×7 surface remains even after the formation of (5×2)-Au and (4×1)-In. The SH response of Si(111)-4×1-In was also compared with the RAS studies [1]. The s-polarized SH response from single domain Si(111)-4×1-In showed a large, anisotropic change on formation of the In structure. The SH intensity at 1064 nm, increased by about a factor of six over that of Si(111)-7×7, when the nonlinear susceptibility in the surface plane along the In chains and step edges was probed, while the nonlinear susceptibility in the surface plane perpendicular to the step edges remained almost unchanged. In the case of Si(111)-5×2-Au, both SHG [6] and RAS [7] studies found dominant polarizabilities in the surface plane perpendicular to the Au chains and step edges. Previous SHG studies of 3×1-Ag on a singular Si(111) surface reported that the surface does not possess a mirror plane [8]. There also have been a number of SHG studies of Ag structures on Si(111), mostly concerned with investigating the origin of oscillations of the SH intensity with film thickness above 1 ML coverage [9-14]. Random nucleation of three-dimensional islands in thin film growth can cause an increase in SHG through enhancement of the light field by local plasmon resonance. An oscillation of the SHG intensity was reported during growth of Ag and Au thin films on Si(111)-7×7 surfaces [9, 15]. Peaks in the SHG oscillation appeared when one- or two excitation photon energy resonated to energy differences of the quantized states in the Ag films [11]. However, SHG intensity decreased monotonically with Ag deposition on the Si(111)-$\sqrt{3}\times\sqrt{3}$-Ag surface at room temperature. This difference is suggested to be due to the difference in the Ag film growth modes on the Si(111)-7×7 and Si(111)-$\sqrt{3}\times\sqrt{3}$-Ag surfaces.

7.3 SHG results

Vicinal n-type Si(111) samples, cut 1^{o} towards $[\bar{1}\,\bar{1}\,2]$ produced a regular array of ordered single height steps after in situ cleaning by resistive heating using a procedure described in section 4.2. Sharp Si(111)-7×7 LEED patterns were formed after cooling. The preparation of the 3×1 surface is described in detail in section 5.3.1. The predominantly single domain 3×1 surface was confirmed by using RAS and LEED. The $\sqrt{3}\times\sqrt{3}$ surface was obtained by depositing approximately 1.2 ML of Ag on the Si(111)-7×7 surface and annealing to 500^{o}C. The excitation wavelength was 800 nm, the beam diameter was ~190 μm at the sample, and an incident angle of 67.5^{o} was used. The experimental arrangement is outlined in section 4.4. For excitation at frequency ω in the xz or yz plane of incidence (where z is normal to the surface), the variation of *s*- and *p*-polarized SH intensity, with input polarization angle, α is of the form

$$I_{2\omega}^{p}(\alpha) = C\left|\left\{A\cos^2\alpha + B\sin^2\alpha + C\sin 2\alpha\right\}I_{\omega}\right|^2$$
$$I_{2\omega}^{s}(\alpha) = C\left|\left\{F\cos^2\alpha + G\sin^2\alpha + H\sin 2\alpha\right\}I_{\omega}\right|^2 \qquad (7.1)$$

where α is measured from the plane of incidence, and C is a collection of constants [16]. The tensor components probed are of the general form χ_{ijk} (where *ijk* refers to the *i*-coordinate SH field for *j, k* excitation), Tables 7.1, 7.2 and 7.3 show the various tensor components of 1 and 1m surfaces probed for the *s*- and *p*-polarized SH output, for excitation in the xz ($\alpha - sx$, $\alpha - px$, $[\bar{1}\bar{1}2]$ azimuth) and yz ($\alpha - sy$, $\alpha - py$, $[1\bar{1}0]$ azimuth) planes of incidence.

7.3.1 SHG results of Si(111)-7×7

Figure 7.1 (top panel) shows the $\alpha{-}sx$ and $\alpha - px$ SH rotation plots for the clean, vicinal Si(111)-7×7 surface in the xz ($\bar{1}\,\bar{1}2$ azimuth) plane of incidence. The vicinal Si(111)-7×7 surface has a macroscopic 1m symmetry, with the xz mirror plane orthogonal to the step edge [17]. When the plane of incidence is aligned with xz mirror plane, the s-polarized SH response depends only on the *yxy* and *yzy* tensor components, the other components being zero by symmetry (Table 7.1). Any s-polarized SH response under these conditions must vary as $\sin^2 2\alpha$, via *H* in equation (7.1). Figure 7.1 (top panel - left) shows this behaviour, which is used for sample alignment as discussed in section 4.4.2. Figure 7.3 (bottom panel) shows the $\alpha{-}sy$ and $\alpha - py$ SH rotation plots in the yz ($[1\bar{1}0]$ azimuth) plane of incidence. The unequal lobes for $\alpha{-}sy$ shows the absence of a mirror plane in this direction and confirms the 1m symmetry of vicinal Si(111)-7×7-surface.

7.3.2 SHG results of Si(111)-3×1-Ag and Si(111)-$\sqrt{3}\times\sqrt{3}$-Ag

Initial measurements on 3×1-Ag surface revealed that the ratio of *p*- to *s*-polarization intensities was very large, raising concerns that small experimental misalignments could have a significant effect on the critical *s*-output measurements. Hence precise alignment procedures were carried out before taking the actual measurements, as described in section 4.4.2. These procedures produced the $\alpha{-}sx$ (*s*-polarized output; *x* azimuth) plot of the top left panel of figure 7.1, where the four peaks of equal intensity confirmed the precise alignment necessary to avoid leakage of the *p*-polarized response into the $\alpha - s$ signals. As a second check, a misalignment of the output polarizer by 5° from the $\alpha{-}sx$ configuration, for the Si(111)-3×1-Ag structure, produced figure 7.2, where the solid line is a least squares fit using the parameters determined from the $\alpha{-}sx$ and $\alpha - px$ plots of figure 7.3, added coherently in a proportion determined by the polarizer offset. The only adjustable parameters were the relative phase of the *s*- and *p*-polarizations, and the overall intensity, which required a 6% adjustment. This is within the estimated error

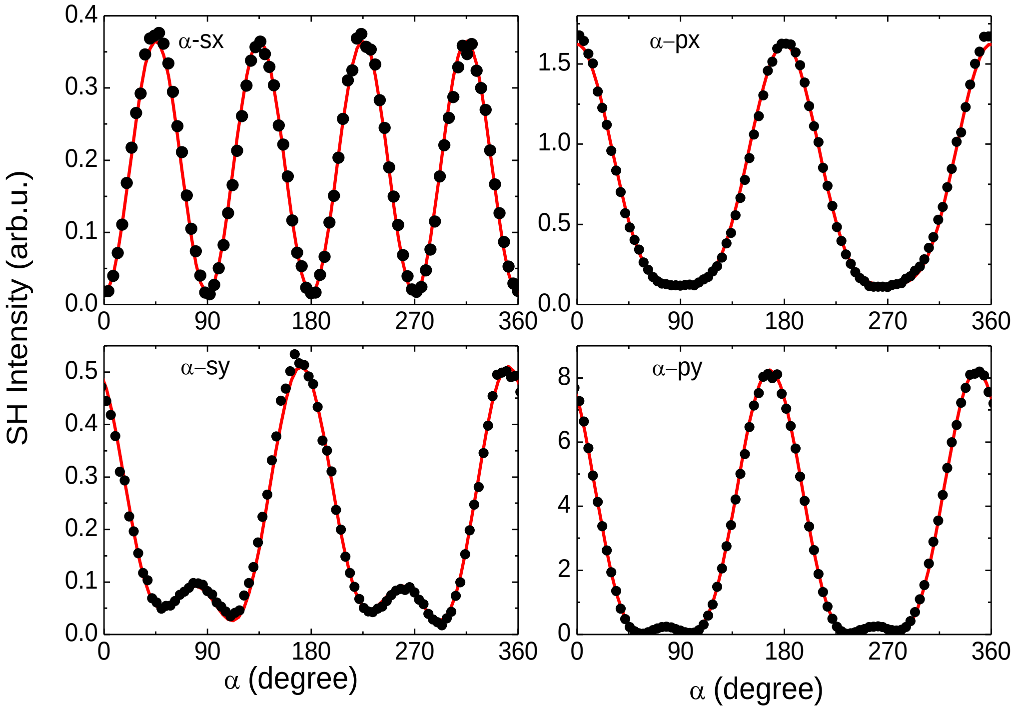

Figure 7.1 SHG rotation plots for Si(111)-7×7 where $\alpha - sx$ and $\alpha - px$ *xz* plane of incidence ([$\bar{1}\bar{1}2$] azimuth), and α–*sy* and α–*py* (*yz* plane of incidence ([$1\bar{1}0$] azimuth). The solid lines are fits to equation (7.1).

resulting from combining the results of three independent intensity measurements. Comparison of figures 7.2 and 7.3 shows the dramatic change associated with a polarizer misalignment of only $5°$, underlining the care required when the *s*- and *p*-polarization intensities differ by orders of magnitude.

Figure 7.3 shows the variation of *s*- and *p*-polarized SH intensity of the Si(111)-3×1-Ag surface, for excitation in the *xz* and *yz* planes of incidence. The *s*-output response of figure 7.3 departs significantly from $\sin^2 2\alpha$ behaviour (see 7.3.1), providing conclusive proof of the absence of an *xz* mirror plane in the (3×1)-Ag structure. The exclusion of a mirror plane in the *y*-azimuth, however cannot be proved in the present case, due to the absence of mirror plane for the vicinal Si(111)-7×7 surface in this direction. These results are consistent with the non-zero s-in/s-out results of Deng *et al.* [8] and also with the HCC structural model proposed for the (3×1)-Ag surface discussed in section 5.3 [18, 19]. The Ag atoms bond to a single atom in the silicon chain on one side of the trench and can bond to one of two atoms in the partial double layer on the other side, breaking the mirror symmetry along [$\bar{1}\bar{1}2$] [18, 19]. As discussed above, a slight misalignment would be

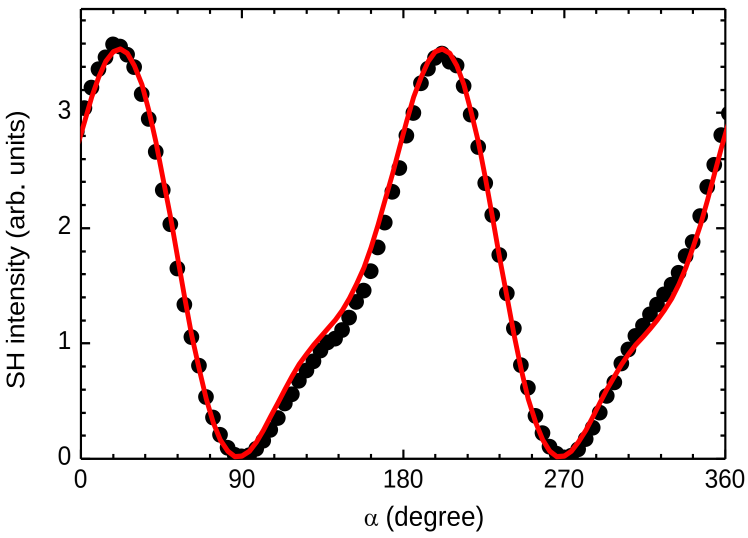

Figure 7.2 SHG rotation plots for *α –sx* Si(111)-3×1-Ag , with the output polarizer misaligned by 5°.The solid line is the least square fir described in the text.

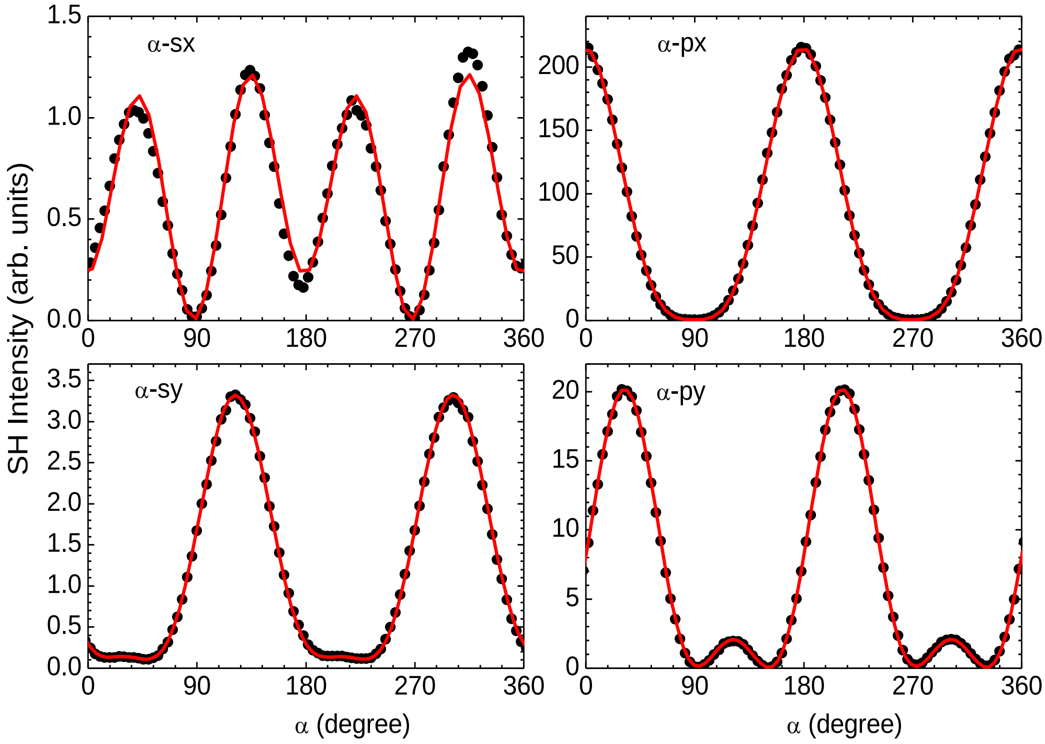

Figure 7.3 SHG rotation plots for Si(111)-3×1-Ag, for the *xz* and *yz* planes of incidence. The solid lines are fit to equation (7.1).

sufficient to produce, the s-in/s-out results of Deng *et al.* [8]: the $\alpha - sx$ plots of figures 7.1 and 7.3 are a much more reliable test of the absence of the *xz* mirror plane.

Figure 7.4 shows the variation of *s*- and *p*-polarized SH intensity of the Si(111)-$\sqrt{3}\times\sqrt{3}$-Ag surface, for excitation in the *xz* and *yz* planes of incidence. The $\alpha - sx$ response is consistent with the presence of mirror plane, but care in interpretation is required because missing tensor components may not be forbidden, but may be simply too small for detection. Two structural models have been proposed for the $\sqrt{3}\times\sqrt{3}$ reconstruction based on its empty-state STM images at RT [20, 21] and at LT (62K) [22-24].

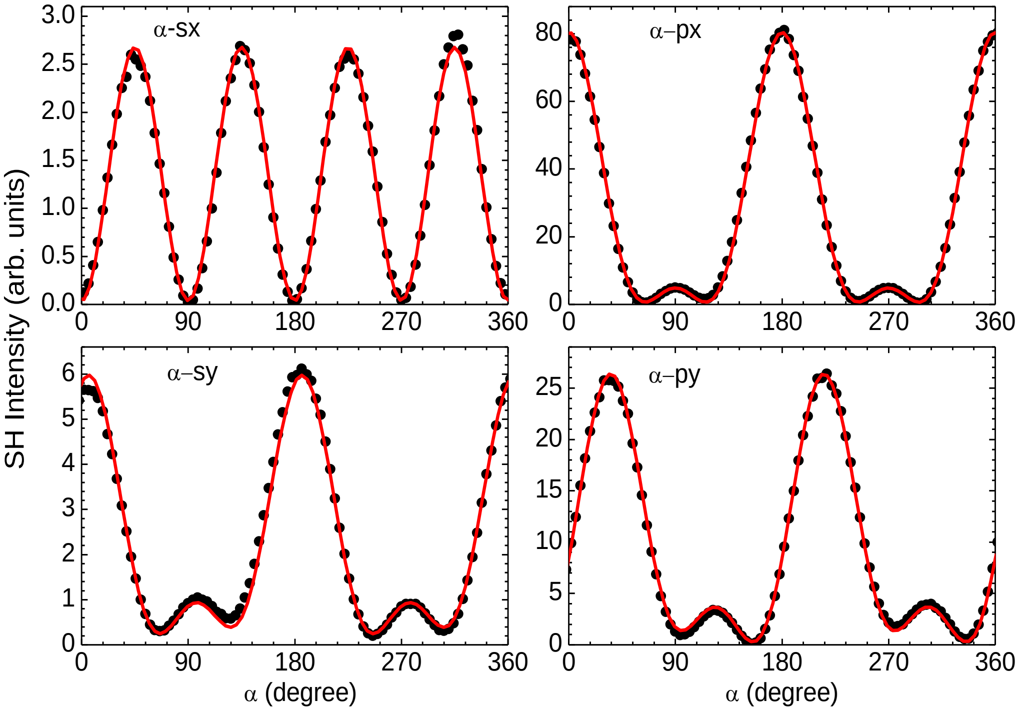

Figure 7.4 SHG rotation plots (including Fresnel factors) for Si(111)-$\sqrt{3}\times\sqrt{3}$-Ag, for the *xz* and *yz* planes of incidence. The solid lines are fits to equation (7.1).

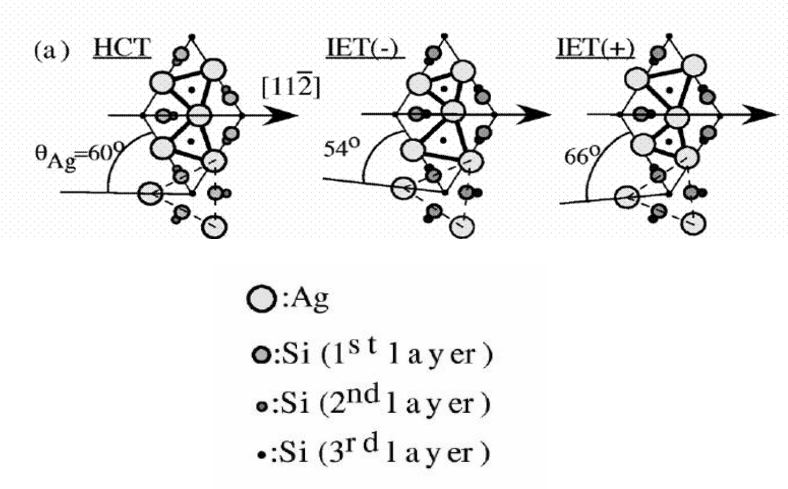

Figure 7.5 Schematic illustrations of the HCT and IET models for the Si(111)-$\sqrt{3}\times\sqrt{3}$-Ag surface. Thin solid lines indicate the unit cell and thick ones represent Ag trimers The triangles with thin broken lines and angles show differences between HCT, IET(-), and IET(+) [24].

The atomic arrangement of RT phase is known to be honeycomb-chained triangle (HCT), in which each atom makes an ionic covalent bond with a substrate Si atom, leaving no dangling bonds. The structural model proposed for the LT phase is an inequivalent triangle (IET). In this model, the positions of three Ag atoms in each unit cell are slightly rotated in the same direction around the cell corner from those of the HCT structure. As a consequence two inequivalent Ag triangles of different sizes are formed in a unit cell, and a mirror plane along $[\bar{1}\,\bar{1}2]$ crystal axis in the HCT model disappears in the IET model (figure 7.5). Previous SHG studies on $\sqrt{3}\times\sqrt{3}$ reported an increase in s-in/s-out response as the temperature is lowered, which is interpreted as a transition from HCT to IET [25]. The symmetry observed in figure 7.4 could be due to equal populations of the IET structures at RT.

Table 7.1 shows the various fitting parameters for excitation in the *x*- and *y*- azimuths for *s* and *p*- polarized SH output for vicinal Si(111)-7×7. The interpretation of the overall SH response is complicated by contributions from the many different tensor components of the 1m surface. This is particularly so for the $\alpha - p$ configuration.

Table 7.1 Tensor components (including Fresnel factors) contributing to the polarization rotation plots of figure 7.1, and the fitted parameter values using equation (7.1), normalised to the *x*-azimuth value of H of Si(111)- 7×7.

		Vicinal Si(111)-7×7-Ag (1m symmetry)			
		x-azimuth		*y*-azimuth	
α-*p*	*A*	*zxx zxz* *zzz xxx* *xzx xzz*	2.145	*zyy zzz* *yzy*	4.592
	B	*zyy xyy*	$0.556e^{i69}$	*zxx*	$0.595e^{-i148}$
	C			*zxz yxy*	$1.233e^{i162}$
α-*s*	*F*			*xyy xzz*	1.155
	G			*xxx*	$0.421e^{i136}$
	H	*yxy yzy*	1	*xzx*	$0.20e^{i151}$

Table 7.2 Tensor components contributing to the polarization rotation plots of figures 7.3 and the fitted parameter values using equation (7.1), normalised to the *x*-azimuth value of H of Si(111)-7×7.

		Vicinal Si(111)-3×1-Ag (1 symmetry)			
		x-azimuth		*y*-azimuth	
α-*p*	*A*	*zxx zxz* *zzz xxx* *xzx xzz*	24.8	*zyy zyz* *zzz yyy* *yzy yzz*	4.81
	B	*zyy xyy*	$1.20e^{i29}$	*zxx yxx*	$0.73e^{-i52}$
	C	*zxy zyz* *xyx xyz*	$0.44e^{i148}$	*zyx zxz* *yxy yxz*	$4.47e^{i3}$
α-*s*	*F*	*yxx yxz* *yzz*	0.80	*xyy xyz* *xzz*	0.91
	G	*yyy*	$0.16e^{i94}$	*xxx*	$2.19e^{-i30}$
	H	*yxy yzy*	$1.76e^{-i85}$	*xyx xzx*	$1.45e^{i137}$

Table 7.3 Tensor components contributing to the polarization rotation plots of figures 7.4 and the fitted parameter values using equation (7.1), normalised to the *x*-azimuth value of H of Si(111)-7×7.

	Vicinal Si(111)-$\sqrt{3}\times\sqrt{3}$-Ag (1m symmetry)				
	x-azimuth			*y*-azimuth	
α-p	*A*	*zxx zxz* *zzz xxx* *xzx xzz*	15.1	*zyy zzz* *yzy*	4.89
	B	*zyy xyy*	$3.71e^{i153}$	*zxx*	$2.19e^{-i56}$
	C			*zxz yxy*	$5.38e^{i7}$
α-s	*F*			*xyy xzz*	4.06
	G			*xxx*	$1.52e^{i132}$
	H	*yxy yzy*	2.74	*xzx*	$0.59e^{-i25}$

Tables 7.2 and 7.3 show equivalent results for vicinal Si(111)-3×1-Ag and Si(111)-$\sqrt{3}\times\sqrt{3}$-Ag. The dominance of χ_{xxx} in the *s*-output response, for excitation in the *y*-azimuth, of the (3×1)-Ag surface is consistent with dominant polarizability perpendicular to the step edges (see section 5.3.2) seen by RAS at the excitation wavelength of 800 nm (1.55 eV). In contrast with the (4×1)-In system [1], there is no evidence, at these energies, of a large response from *y*-dependent components, which would have indicated a dominant polarizability in the step direction. Figures 7.3 and 7.4, and tables 7.2 and 7.3 show that there are substantial changes in the SH response between the (3×1)-Ag and the ($\sqrt{3}\times\sqrt{3}$)-Ag structures. Further interpretation is difficult, however, because of the large number of tensor components that contribute to the SH response from these low symmetry structures. Even spectroscopic studies are unlikely to be readily interpreted without the benefit of microscopic calculations, very few of which have been attempted for SHG. The main strength of SHG that has been exploited in this section is its sensitivity and interface symmetry.

7.3.3 SHG results of Ag nanodots and Ag islands

The preparation details of Ag nanodots and Ag islands on si(111)-3×1-Ag are given in section 6.5. The excitation wavelength was 800 nm, the beam diameter was ~190 μm at the sample and an incident angle of 67.5° was used. The experimental arrangement is outlined in section 4.4. Results obtained by depositing 0.5 ML (nanodots) and 2 ML (islands) onto the Si(111)-3×1-Ag surface are presented in figure 7.6. It can be seen that SHG observed from the island surfaces is significantly smaller than that from the Si(111)-3×1-Ag surface (figure 7.3).

In attempting simple modelling of the SHG response, the STM images (figures 6.6 and 6.10) have shown that the nanodots and islands only cover a proportion of the surface, the remainder being (3×1)-Ag. The simplest assumption is that the effective nonlinear susceptibility, $\chi^{(2)}$, can be written as

$$\chi^{(2)} = a\chi^{(2)}_{3\times1} + (1-a)\chi^{(2)}_{nanodots(islands)} \tag{7.2}$$

where $\chi^{(2)}_{3x1}$ and $\chi^{(2)}_{nanodots(islands)}$ are the contributions to $\chi^{(2)}$ from the (3×1)-Ag surface and the nanodots (islands) response respectively, and *a* represents the fraction of (3×1)-Ag surface remaining. The STM studies discussed in section 6.5, revealed the nanodots to be circular with a constant diameter of 1 nm and that the 19 ± 1 atoms and consistent with Ag(111) packing. It also has been observed that the registry of Ag atoms on Si substrates was primarily driven by geometrical matching, and that the 3D Ag islands showed, <111> preferred growth orientation on an Si(111) substrate [26, 27]. Hence, it is reasonable to assume that both the nanodots and islands have 3m symmetry.

In developing the model, the (3×1)-Ag contribution is known (Table 7.2), and the 3m symmetry of the nanodots and islands reduces the number of new tensor components:

xxx = -*xyy* = -*yxy*
xzx = *yxy*
zxx = *zyy*

leaving only four independent components, zxx, zzz, xxx and xzx. However, the Fresnel factors for the tensor components have to be determined in order to exploit these symmetry relations. Using the dielectric function of bulk Si at the energies involved, and the expressions of Lüpke *et al.* [28], the Fresnel factors of Table 7.4 were calculated for an incident angle of 67.5°, where the very small mixing of tensor components associated with the 1° offcut has been neglected

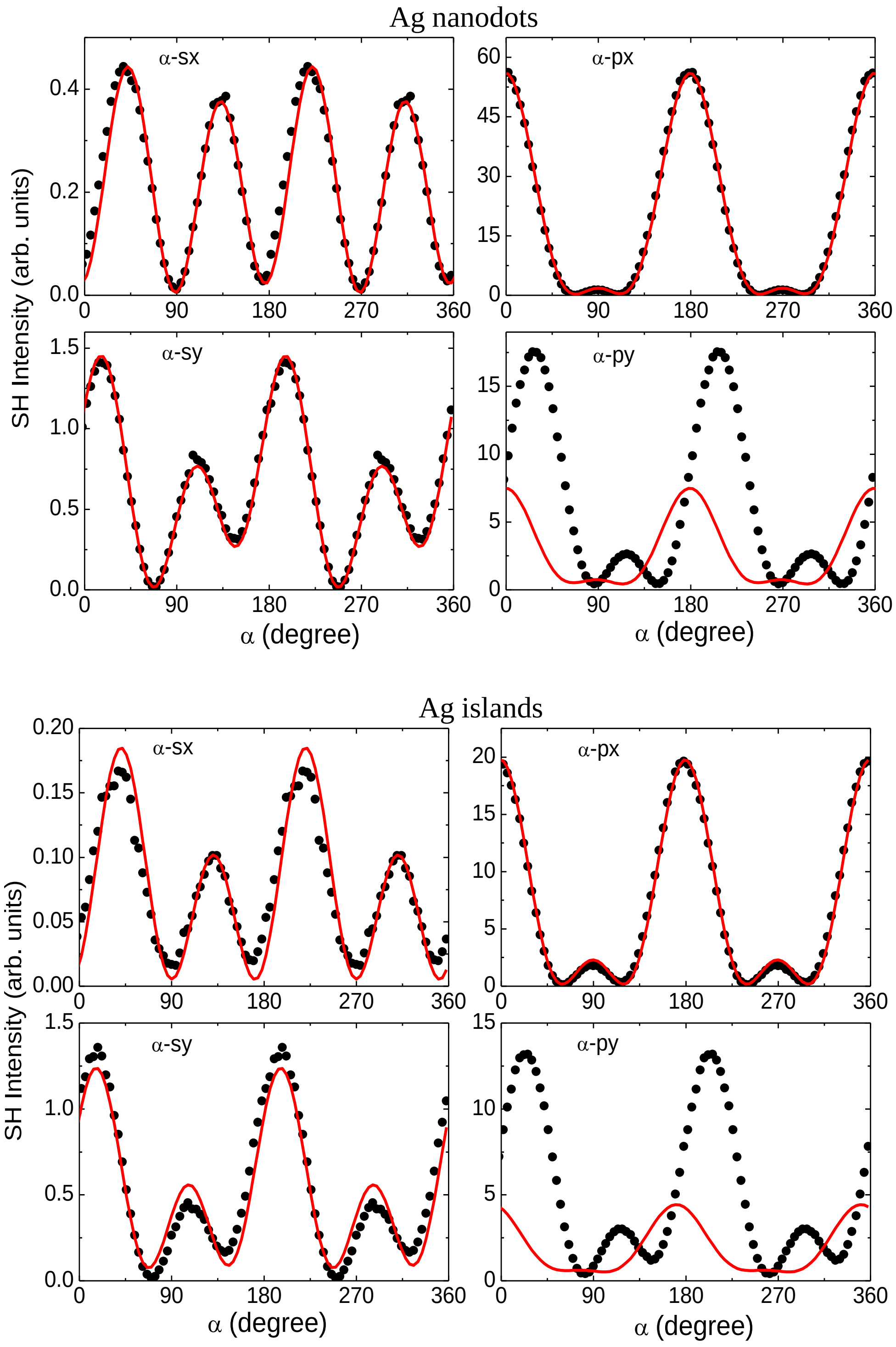

Figure 7.6 SHG rotation plots for Ag nanodots (0.5 ML) and Ag islands (2ML) on the 1° offcut Si(111)-3×1-Ag surface, for the *xz* and *yz* planes of incidence. The solid line is the least squares fit described in the text

Table 7.4 Fresnel factors for Si(111) surfaces with 3m symmetry, incidence angle 67.5^{o}, fundamental wavelength 800 nm (3m symmetry).

	χ □(3m)	Fresnel factors (*xxx* = -*xyy* = -*yxy*, *xzx* = *yzy*, *zxx* = *zyy*) $px\ \ (\psi = 0^\circ)$
A	*zxx zzz* *xxx xzx*	$4.835e^{i4}\chi_{zxx} + 0.323e^{i4}\chi_{zzz} + 0.925e^{i180} + 0.478e^{i180}\chi_{xzx}$
B	*zyy xyy*	$5.158e^{i4}\chi_{zyy} + 0.986e^{i180}\chi_{xyy}$
C	-	

	χ □(3m)	$py\ \ (\psi = 90^\circ)$
A	*zyy zzz yzy*	$4.835e^{i4}\chi_{zyy} + 0.323e^{i4}\chi_{zzz} + 0.478e^{i180}\chi_{yzy}$
B	*zxx*	$5.158e^{i4}\chi_{zxx}$
C	*yxy*	$0.955e^{i0}\chi_{yxy}$

	χ □(3m)	$sx\ (\psi = 0^{o})$
F	-	
G	-	
H	*yxy yzy*	$0.968e^{i0}\chi_{yxy} + 0.250e^{i0}\chi_{yzy}$

	χ □(3m)	$sy\ (\psi = 90^{o})$
F	*xyy*	$0.937e^{i180}\chi_{xyy}$
G	*xxx*	$1.000e^{i180}\chi_{xxx}$
H	*xzx*	$0.2501e^{i180}\chi_{xzx}$

.

Table 7.5 Tensor components contributing to the polarization rotation plots of figure 7.6, and the fitted parameter values using equation (7.2), assuming 3m symmetry for the nanodots and islands.

	Ag - nanodots	Ag - islands
a	0.33	0.24
zxx	$0.231e^{-i122}$	$0.20e^{-i172}$
zzz	$4.73e^{i0}$	$4.44e^{-i129}$
xxx	$1.41e^{-i173}$	$1.19e^{i161}$
xzx	$4.09e^{-i154}$	$0.231e^{i131}$

Figure 7.6 shows the result least-squares fits (solid lines) using equation (7.2) the parameters of the (3×1)-Ag surface (Table 7.2) values, but without normalisation and Fresnel factors (table 7.4). Table 7.5 shows the corresponding tensor components. It can be seen that the fit is poor, and is certainly not unique. This implies a significant interaction between the nanodots and islands, and the underlying (3×1)-Ag chains, as discussed in section 6.5. Further interpretation is not justified for the reasons discussed above.

References

1. Chandola S, McGilp JF: **Optical second harmonic generation at Si(111)-In interfaces: Evidence of quasi-one-dimensional metallicity.** *physica status solidi (a)* 2001, **184:**111-116.
2. Chandola S, McGilp JF: **Optical second harmonic generation studies of indium deposited on vicinal Si(111).** *Physica Status Solidi a-Applied Research* 1999, **175:**189-193.
3. O'Mahony JD, McGilp JF, Verbruggen MHW, Flipse CFJ: **Au Structures on Si(111) Studied by Spectroscopic Ellipsometry and Optical 2nd-Harmonic Generation.** *Surface Science* 1993, **287:**713-717.
4. O'Mahony JD, Kelly PV, McGilp JF: **Optical 2nd Harmonic-Generation from Ordered Si(111)-Au Interfaces.** *Applied Surface Science* 1992, **56-8:**449-452.
5. Chandola S, Carroll L, McGilp JF: **Anisotropic second harmonic generation from Si(111)-4x1-In.** *physica status solidi (c)* 2003, **0:**3050-3054.
6. O'Mahony JD, Kelly PV, McGilp JF: **Optical second harmonic generation from ordered Si(111)-Au interfaces.** In *Applied Surface Science, vol.56-58, no.1-4, pt.A, March 1992, pp.449-52. Netherlands.*;
7. Power JR, Weightman P, O'Mahony JD: **Strong optical anisotropy of the single-domain 5*2-Au reconstruction on vicinal Si(111).** *Physical Review B-Condensed Matter* 1997, **56:**3587-3590.
8. Deng D, Suzuki T: **Si(111)-3*1-Ag reconstruction studied in situ at elevated temperatures by second-harmonic generation.** *Japanese Journal of Applied Physics, Part 2 (Letters)* 2004, **43:**510-512.

9. Pedersen TG, Pedersen K, Kristensen TB: **Optical second-harmonic generation from Ag quantum wells on Si(111)7*7: Experiment and theory.** *Physical Review B-Condensed Matter* 1999, **60:**R13997-14000.
10. Hirayama H, Komizo T, Kawata T, Takayanagi K: **Changes of phase and intensity of optical SHG with Ag deposition on Si(111)-7*7 surfaces.** *Applied Surface Science* 2002, **190:**108-112.
11. Hirayama H, Kawata T, Takayanagi K: **Oscillation of the optical second-harmonic generation intensity during Ag thin film growth on a Si(111)7*7 surface.** *Physical Review B-Condensed Matter* 2001, **64:**195415/195411-195415.
12. Pedersen K, Kristensen TB, Pedersen TG, Morgen P, Li Z, Hoffmann SV: **Optical second-harmonic generation and photoemission from quantum well states in thin Ag films on Si(1 1 1).** *Surface Science* 2001, **482-485:**735-739.
13. Hirayama H, Yamasaki A, Kawata T: **Change of optical second harmonic generation intensity during Ag deposition on Si(111)7*7 and Si(111)sqrt[3]*sqrt[3]-Ag surfaces.** *Surface Science* 2003, **532-535:**922-927.
14. Hirayama H, Watai M: **Two-photon resonance in optical second harmonic generation from quantum well states in ultra-thin Ag films grown on Si(1 1 1) surfaces.** *Surface Science* 2006, **600:**3825-3829.
15. Pedersen TG, Pedersen K, Kristensen TB: **Theory of second-harmonic generation from quantum well states in ultrathin metal films on semiconductors.** *Physical Review B-Condensed Matter* 2000, **61:**10255-10266.
16. Power JR, O'Mahony JD, Chandola S, McGilp JF: **Resonant Optical 2nd-Harmonic Generation at the Steps of Vicinal Si(001).** *Physical Review Letters* 1995, **75:**1138-1141.
17. McGilp JF: **Using steps at the Si -SiO2 interface to test simple bond models of the optical second-harmonic response.** *Journal of Physics: Condensed Matter* 2007, **19:**016006.
18. Collazo-Davila C, Grozea D, Marks LD: **Determination and refinement of the Ag/Si(111)-(3*1) surface structure.** *Physical Review Letters* 1998, **80:**1678-1681.
19. Erwin SC, Weitering HH: **Theory of the "honeycomb chain-channel" reconstruction of M/Si(111)-(3*1).** *Physical Review Letters* 1998, **81:**2296-2299.
20. Wan KJ, Lin XF, Nogami J: **Reexamination of the Ag/Si(111)-sqrt[3]*sqrt[3] surface by scanning tunneling microscopy.** *Physical Review B (Condensed Matter)* 1992, **45:**9509-9512.
21. Ding YG, Chan CT, Ho KM: **Structure of the sqrt[3]*sqrt[3] R30 Ag/Si(111) surface from first-principles calculations.** *Physical Review Letters* 1991, **67:**1454-1457.
22. Aizawa H, Tsukada M, Sato N, Hasegawa S: **Asymmetric structure of the Si(111)-sqrt[3]*sqrt[3]-Ag surface.** *Surface Science* 1999, **429:**509-514.
23. Sato N, Nagao T, Hasegawa S: **Si(111)-(sqrt[3]*sqrt[3])-Ag surface at low temperatures: symmetry breaking and surface twin boundaries.** *Surface Science* 1999, **442:**65-73.
24. Matsuda I, Morikawa H, Liu C, Ohuchi S, Hasegawa S, Okuda T, Kinoshita T, Ottaviani C, Cricenti A, D'angelo M, et al: **Electronic evidence of asymmetry in the Si(111) square root 3 * square root 3 -Ag structure.** *Physical Review B (Condensed Matter and Materials Physics)* 2003, **68:**85407-85401.
25. Venkataraghavan R, Aono M, Suzuki T: **Studies on the nucleation, dynamics and structure of the Si(111)-sqrt[3]*sqrt[3]-Ag surface using surface second-harmonic generation.** *Surface Science* 2002, **517:**65-74.
26. Aburano RD, Hawoong H, Roesler JM, Chung K, Lin DS, Zschack P, Chen H, Chiang TC: **Boundary-structure determination of Ag/Si(111) interfaces by X-ray diffraction.** *Physical Review B (Condensed Matter)* 1995, **52:**1839-1847.

27. Goswami DK, Bhattacharjee K, Satpati B, Roy S, Satyam PV, Dev BN: **Preferential heights in the growth of Ag islands on Si(1 1 1)-(7*7) surfaces.** *Surface Science* 2007, **601:**603-608.
28. Lüpke G, Bottomley DJ, van Driel HM: **Second- and third-harmonic generation from cubic centrosymmetric crystals with vicinal faces: phenomenological theory and experiment.** *Journal of the Optical Society of America B-Optical Physics* 1994, **11:**33-44.

8

Conclusions and outlook

8.1 General review

The main objective of this thesis was to explore the characteristics of LD structures, in-situ and non-destructively, by the linear and non linear optical techniques: RAS and SHG. Secondly, the growth of capping layers on the LD structures to protect them from ambient conditions during study or use outside the growth chamber, was investigated. These state-of-the art epioptic [1] techniques exploit the difference in symmetry between the surface or interface and the centrosymmetric structure of substrates such as Si and also capping layers, in order to eliminate the normally dominant bulk response. These techniques are very well suited to probe the properties of buried nanostructures, as their penetration depth is much larger than that of conventional surface probes, and the lower symmetry of aligned nanostructures helps to discriminate the nanostructure response from the residual interface, bulk and capping layer response.

RAS results have been presented for Si(111)-3×1–Ag, Si(111)-5×2-Au, Si(557)-5×1-Au and Si(111)-4×1-In with the spectral range extended to IR wavelengths. In the region below 3eV, large minima are observed, which show, systematically, a higher polarizability perpendicular to the adsorbate chains for all these structures. The detail, however, varies with the adsorbate and the reconstruction. By monitoring the RAS signal at the minima, single-domain Si(111)-m×n–X (where X = Ag, Au and In) could be grown quite easily. The RAS response of (3×1)–Ag surface below 1eV is almost zero, consistent with the structure being semiconducting. RAS studies of Si(111)-5×2-Au structures, grown on substrates with different offcuts and step densities, show significant differences in the spectral region below 2.5 eV. These changes have been attributed to a variation in the relative population of single and double Au chains. Previous work has provided good evidence that only single Au chains form in the region of $[11\overline{2}]$ offcut steps [2], and the RAS results from Si(557)-5×1-Au are consistent with this interpretation. Zig-zag chains of adsorbate are found on all of the above surfaces. If the electronic states involved are located at the metal-Si backbond, as previously suggested for the Si(111)-4×1-In [3], the broad minimum in Si(111)-5×2-Au is consistent with a double chain and two different Au positions in the surface unit cell, leading to similar, but energetically shifted, electronic states.

Below about 1.2eV, the RAS signal is positive, indicating a dominant polarizability along the chain direction, but with a large difference between the single and double chain response. These results show, for the first time, an intriguing difference in the general anisotropic optical response of the single- and double-chain structures. Theoretical models of these chain structures can now be tested against the RAS data, if electronic structure calculations are extended to excited states, and the linear optical response calculated.

Two-dimensional Ag nanodots of 1 nm diameter were grown by self-assembly on the Si(111)–3 × 1-Ag surface, in rows running parallel to the steps of the vicinal surface. STS has shown that the clusters are non-metallic, with a bandgap of ~0.6 eV, consistent with the opening of a Kubo gap due to confinement of the electron wavefunction. This is expected for such small clusters, provided that their separation is at least comparable to their dimension, thus reducing lateral interactions. The nanodots showed a very small optical response in the IR region, which is consistent with their non-metallic character. Larger, anisotropic 3D Ag islands, formed by further deposition of Ag, also align along the rows, but STS has shown these to have well-developed metallic character, in agreement with their larger size. RAS measurements extended into the IR region have been shown to be consistent with the electronic properties of the nanostructures measured by STS. The large positive IR anisotropy for the 3D Ag islands is in the region where anisotropic Drude-like intraband transitions begin to become significant, the larger polarizability being aligned along the length of the islands, where the inelastic scattering electron mean free path is expected to be longer. The anisotropy is also found to be influenced by the offcut angle of the substrate, and hence the terrace width, and a simple analysis based on diffusion of Ag atoms across the terraces has been presented. The agreement between the electronic properties, as measured by STS and the IR measurements indicates that IR RAS should be a useful technique for the non-contact probing of the metallicity of aligned anisotropic nanostructures.

The Ag nanostructures were capped with Si to form a near-IR transparent protecting layer. The samples were stable to exposure to ambient conditions for significant periods. The RAS spectra were compared to model calculations, which included the known dielectric functions of the substrate and capping material and an anisotropic, Drude-like, dielectric function for the metallic nanostructures. This simple model supported the conclusion that the metallic nanostructures survive the capping, while the (3×1) areas not covered by the nanostructures are modified by the deposition of Si. However, the quasi-1D structure of Si(111)-4×1-In did not survive the capping by amorphous Si, as the (4×1)-In related RAS signature was destroyed.

Optical second harmonic generation (SHG) was used to study the structural symmetry of (3×1)-Ag, ($\sqrt{3}\times\sqrt{3}$)-Ag, Ag nanodots and Ag islands. SHG studies of predominantly single domain Si(111)-3×1-Ag provide conclusive proof that the structure does not possess a mirror plane, in agreement with previous polarization-selected SHG studies on the singular surface [4]. It is shown that, as the ratio of p- to s- polarized SH intensity is large, precise alignment procedures are required to eliminate any leakage of p-output polarization into the s-output measurements. SHG studies of the ($\sqrt{3}\times\sqrt{3}$)-Ag surface are consistent with the presence of a mirror plane but, while SHG can prove the absence of a mirror plane, only a consistency with higher symmetries can be shown, as a number of other factors could account for the apparent symmetry. SHG studies of Ag nanodots and Ag islands revealed deviation from 3m symmetry, implying interaction between the Ag nanostructures and the underlying (3×1)-Ag chain.

It has been shown that RAS and SHG provide complementary information about LD structures. RAS is experimentally simpler, and also more amenable to theory, while SHG provides additional symmetry information that the linear optical technique cannot supply.

8.2 Outlook

The observed difference in the RAS signal of Si(557)-5×1-Au and Si(111)-5×2-Au, 4^o offcut $[11\bar{2}]$ sample is attributed to the difference in Au chain populations. RAS measurement of Si(775)-5×2-Au, which is structurally similar to the Si(111)-5×2-Au, 4^o offcut towards $[11\bar{2}]$, should be helpful in comparing these structures and the related RAS signal, because ARUPS and electronic structure calculations are available for the (775) offcut [2].

STM measurements are required to identify the morphology of the islands grown on the Si(111)-3×1-Ag, for comparison with the model predictions of section 6.5.3. This will also be helpful in the full multilayer modelling the optical anisotropy of the capped and uncapped nanostructures. Surface plasmon-polariton behaviour may account for the large red shift in the RAS signal of the metallic islands on the introduction of the capping layer, and hence needs to be included in a general optical model. Capping of quasi-1D structures needs to be explored further. One approach is to try to grow epitaxial silicon, without destroying the LD characteristics. The problem here is to find a temperature window for epitaxial growth that does not destroy the nanostructure.

RT SHG studies of Si(111)-$\sqrt{3}\times\sqrt{3}$-Ag did not reveal the symmetry breaking nature of the surface, but a low temperature study would provide important additional information. SHG studies of the anisotropic islands need to be done at longer wavelengths for the comparison with linear optical studies, but this will require investment in an optical parametric oscillator.

References

1. McGilp JF: **Optical second-harmonic generation for studying surfaces and interfaces.** *Journal of Physics Condensed Matter* 1989, **1:**85-92.
2. Crain JN, McChesney JL, Fan Z, Gallagher MC, Snijders PC, Bissen M, Gundelach C, Erwin SC, Himpsel FJ: **Chains of gold atoms with tailored electronic states.** *Physical Review B (Condensed Matter)* 2004, **69:**125401-125401.
3. Pedreschi F, Omahony JD, Weightman P, Power JR: **Evidence of electron confinement in the single-domain (4*1)-In superstructure on vicinal Si(111).** *Applied Physics Letters* 1998, **73:**2152-2154.

4. Deng D, Suzuki T: **Si(111)-3*1-Ag reconstruction studied in situ at elevated temperatures by second-harmonic generation.** *Japanese Journal of Applied Physics, Part 2 (Letters)* 2004, **43:**510-512.

Appendix A
Description of RAS components

High pressure Xenon lamp

In any optical technique, adequate light intensity is of crucial importance, and RAS is no exception. As the reflectance difference is very small compared to the absolute reflectance, this is an additional problem, as fluctuations in the light source may be contribute significant noise to the RAS signal. The required light source must be of sufficient intensity that the signal is not buried in background noise, and sufficiently stable that it does not contribute to the noise itself. It is also advantageous if the lamp has a small spot size, to enable examination of small samples and optimize the use of small area detectors. The light source used in the current set-up was a high pressure Xenon discharge lamp. A continuous mode super quiet Xenon lamp from Hamamatsu (model L2194-02) was combined with a C6979 dropper type power supply. In general, the lamp requires a thirty minute warm-up period before it achieves adequate stability

Polariser

These are required to linearly polarise the probe light and specify the axes with regard to which the RA response is being measured, and to analyse the time varying signal produced by the PEM. The axis of polarisation is chosen to be at 45° to the axes of interest on the crystal. To allow adequate UV transmission, appropriate materials must be used for the polariser crystal and any cement used in the polariser construction. Both polarisers require rotation during setup and therefore rotational mounts are required. The input polariser, especially, requires precise positioning due to its role as an axis selector. Equation (4.1) shows that inaccuracies in the polariser azimuth can introduce an offset into the real part of the RAS signal. In practice, it is found that rotational accuracy of 30’’ or less is required to reduce this offset to negligible levels [1]. Calcite Glan Taylor polarisers from Ekspla Optics with 10 mm apertures were selected for this application. Wider apertures may be used if greater intensity is required. If two polarisers of different quality are used, the better one should be used for the input polariser, due to the effects of polariser imperfections on imaginary-part spectra. To first order, the analyser is less important in this regard. Rotational accuracy is also not as important, as analyser offset tends to affect the DC level, rather than the AC, and autophasing the lock-in may assist here.

Low strain window

As RAS measures sample induced changes to a polarised light beam, all other influences on the beam's polarisation state must be reduced or eliminated. This applies to every optical component between the polariser and analyser, and it may be quite difficult to remove all birefringence effects. As the candidate quantum wire systems investigated here must be maintained in vacuum, the vacuum chamber viewport is an obvious candidate for a source of strain induced birefringence due to the pressure difference across its surface and possibly due to its attachment on a flange. Adequate spectral range is also a consideration. It is possible to obtain windows that are specially fabricated to reduce the possibility of strain effects. They usually employ a cylindrical geometry which distributes pressure-induced strain along the side of the cylinder, rather than along its face. Fused silica is often used for improved UV transmission. Although this geometry reduces window strain, it does not remove it entirely, and this strain will have its own RA spectra that will add to the sample spectrum. If the strain is assumed to be small and constant, however, sample spectra may be adjusted to compensate. The constancy of this strain is a very important factor. Any vibrations in the chamber will be transmitted to the window, and this will modulate the polarisation effects at the vibration frequency and couple those oscillations into the light beam. If they are near any of the PEMs harmonics, they may not be filtered by the lock-in and will result in an offset in the RA spectra. A low strain, fused silica bakeable window was purchased from Bomco U.S.A.

Photoelastic modulator (PEM)

By modulating the retardation along one of its optical axes relative to the other, the polarisation state of any light the PEM interacts with will be altered, as long as the light beam is not polarised along one of those axes. With an appropriate set-up, the PEM will vary the polarization between the axes specified by the polariser. In order to work as efficiently as possible, its aperture must be wide enough to completely accept the light to be analysed. During operation, the PEM crystal is compressed by a piezoelectric transducer, which is driven by a control voltage, which may be quite large. This driving voltage oscillates at a predetermined frequency, which sets the PEM's fundamental frequency. This drive voltage may or may not be a pure sinusoid, but regardless, this will not result in a purely sinusoidal vibration in the crystal. This will result in the presence of higher harmonics in the PEM's oscillating output. Although this is useful in distinguishing between the real and imaginary parts of the RA response, in other regards it can pose problems, especially if the lock-in is driven by a square wave reference. The PEM crystal may also have some residual birefringence as a result of its mounting inside the PEM, in a similar manner to the other optical components. This will add a certain constant value on to the PEM's retardation, which may be represented by $\delta_{PEM} = \delta_{PEM}\sin(\omega t) + \delta_0$, where δ_0 is the constant strain. A Hinds PEM-90 with an FS-50 optical head was used.

Monochromator

A monochromator is required for scanning over a range of photon energies. The grating must have adequate spectral range and it should be computer controllable. Apart from these criteria and a general desire for compactness, there are no other special requirements here. As there are no fine structures in RAS, very high resolution is not required. In this set-up a CM-110 monochromator from Digikröm was used, which is quite compact and features an onboard microcontroller and stepper motor and has an f number of 3.3.

Mirrors

Concave mirrors are used to focus the lamp arc onto the target sample, and to focus the reflected beam into the monochromator. The mirrors should have high quality reflective coatings, and the focal lengths must be appropriate for the RAS installation. It is advantageous if they are matched to the monochromators f number to maximise light collection. Two 25.4mm mirrors, with focal lengths of 150 and 200 mm were used to allow good set-up flexibility.

Detector

There are two main options here: a photomultiplier tube or a photodiode. Each detection method has its own advantages. The detector sees a small AC signal, proportional to the optical anisotropy at the modulator frequency, and a large DC signal. The origin of this was described in chapter 4. The AC signal may be between three to five orders of magnitude smaller than the DC, so low noise signal recovery is an absolute priority and is the prime factor in detector selection. Traditionally, low noise detection has been the domain of the photomultiplier, as its gain occurs at the dynodes and it has no need for noisy electronic amplification. The tube chosen was a Hamamatsu 957-08 hybrid assembly, which consists of a R928 photomultiplier tube and a built-in DC converter, which allows operation from a 15V power supply and a 0 to 4V control voltage for gain. This proved very convenient to use and was relatively compact. However, advances in photodiode design and low noise IC amplifiers have now made the photodiode a viable choice. Later, a dual detector assembly was used, comprising a silicon PIN photodiode for

RAS measurements for the energy range 1.3 to 5.0 eV, and an InGaAs photodiode for the energy range 0.85 eV to 1.3 eV. The InGaAs detector has been used successfully down to 0.75 eV [2], but was limited here due to the decline in the grating efficiency. The dual detector was built by Elektronik-Manufaktur Mahlsdorf (EMM), Germany.

Lock-in Amplifier

This is used to extract the RA signal from the detector output. It compares a reference frequency, selected by the operator, to a broadband input and returns the amplitude of any component of the input that is at the reference frequency. Due to the nature of the lock-in process, the output is the RMS amplitude of the selected frequency component. To maximise the lock-in's output, the input wave must be in phase with the reference wave. Many lock-ins are provided with an autophasing system, which performs this task when required. This generally works by antiphasing the two signals, as it is easier to zero the outputs than it is to maximise them, and then adjusting the reference phase by 180^o. In general, some fine tuning will be required by the operator. EG&G model 7225 lock-in was used here. As well as providing excellent lock-in detection, the instrument provides four digital-to-analogue and two analogue-to-digital converters.

1. Rumberg J: **Thesis, Dip. in Physics.** T.U Berlin, 1996.
2. Fleischer K, Chandola S, Esser N, Richter W, McGilp JF: **Reflectance anisotropy spectroscopy of Si(111)-(4*1)-In.** *physica status solidi (a)* 2001, **188:**1411-1416.